Random lasing action from biocompatible materials

Carlos Caixeiro, Soraya

Awarding institution:
King's College London

Random Lasing action from Biocompatible Materials

Soraya Carlos Caixeiro

Lead supervisor:

Dr. Riccardo Sapienza

Second supervisor:

Prof. Klaus Suhling

Thesis submitted in partial fulfilment of the requirements of the degree of Doctor of Philosophy in Physics

King's College London

School of Natural and Mathematical Sciences

Department of Physics

2018

Thesis defended in London on 21^{st} of March 2018

Examiners:

Prof. Giuseppe Battaglia

Prof. Frank Vollmer

Acknowledgments

Firstly, I would like to thank my supervisor Riccardo Sapienza for introducing me to research and scientific thinking and for having infinite patience and time over the years. You have been a source of inspiration, an ever-reliable source of ideas, a great mentor and friend.

In chronological order, Michele Gaio, Marta Castro-Lopez, Matilda Peruzzo, Sandro Mignuzzi, Sergii Mozorov, Duong Van Ta, Dhruv Saxena and Tahiyat Huq, thank you for all the fruitful discussions, coffee break conversations and group spirit. It was a pleasure to meet you all and a privilege to be able to call you my friends.

To my collaborators, thank you for making this work possible. A special thank you to Francisco Fernandes, for your patience, teachings and friendship. My time at King's was truly a time of nurture and growth, throughout the 7 years I was supported by many members of staff specially, Paul le Long, Julia Kilpatrick and towards the end Bonnie Parker, you all really made my life easier allowing me to focus on my studies and research, thank you. To my fellow PhD students: Alix le Marois, Diane Roth, Pooya Azarhoosh, Daniel Allen, Amy Beedle and Krzysiek Bozek.

Thank you for adding to my experience. A special thank you to my family for the great education and support you have given me not just during my PhD but throughout my life. Agradeço especialmente aos meus pais por tudo, pelo ânimo em alturas difíceis por me apoiarem nesta longa caminhada e aos meus avós que me enchem de amor e que ajudaram a chegar onde cheguei. Obrigado também a minha irmã e aos meus tios e primos pelo imenso carinho.

Lastly to my good friends here and abroad, I am incredibly thankful for all the sanity checks, support and good times. You were my rock, kept me sane, loved and motivated.

List of publications

The work described in this thesis has been published in the following:

- *Disordered Cellulose-Based Nanostructures for Enhanced Light Scattering.* S. Caixeiro, M. Peruzzo, O. D. Onelli, S. Vignolini, R. Sapienza, ACS Applied Materials & Interfaces 9 (9), 7885-7890 (2017).
- *Microsphere Solid-State Biolasers.* V. D. Ta, S. Caixeiro, F. M. Fernandes, R. Sapienza, Advanced Optical Materials 5 (8), 1601022 (2017).
- *Gain-Based Mechanism for pH Sensing Based on Random Lasing.* M. Gaio, S. Caixeiro, B. Marelli, F. G. Omenetto, R Sapienza. Physical Review Applied 7 (3), 034005 (2017).
- *Silk-Based Biocompatible Random Lasing.* S. Caixeiro, M. Gaio, B. Marelli, F. G. Omenetto, R Sapienza, Advanced Optical Materials 4 (7), 998-1003 (2016) .
- *Random laser detector.* R Sapienza, G Michele, S Carlos Caixeiro. US Patent App. 15/319,300 (2015).

Abstract

A new class of lasers has recently emerged: biolasers. Biolasers are sources of stimulated emission suitable for tissue integration. They have begun to captivate the scientific community due to their potential to harness the amplifying power of stimulated emission for biosensing, cell tracking and tagging. The main goal of this thesis is to fabricate a biocompatible random laser, study its properties and demonstrate a proof of sensing.

Random lasers rely on multiple scattering to provide optical trapping necessary for lasing. Nanostructuring promotes light confinement while the gain provides light amplification. The lasing action is independent of the overall shape and instead relies on the device's internal porosity; it can therefore easily adapt to biological media with the ability to withstand stretching, wetness and heat. Firstly we address how engineering light-matter interaction with a single biocompatible material can lead to increased light scattering and increased opaqueness. We demonstrate simple fabrication techniques which allow the nanostructuring of biomaterials. The gain is studied by doping biomaterials such as proteins, polysaccharides and silica and fabricating doped solid state whispering gallery mode laser. The threshold is evaluated as well as the biocompatibility. The different fabrication techniques are complementary and yield the first silk biocompatible random laser, where the technique is not limited to this material. The lasing output is studied in detail for different gain molecules. Miniature spherical random lasers are made and studied in terms of the threshold size dependence. In simultaneous we take on a different approach and develop macroporous lasers using freeze-drying. As proof of principle we explore lasing as a mechanism for enhanced sensing, demonstrating that bio-random lasing acts as a nonlinear sensor that switches off lasing

at high pH values, with a sensitivity ∼100 times larger than its fluorescent counterpart. Additionally we build a theoretical framework which clarifies the sensing mechanism.

The combination of a natural biopolymer and random lasing offers the opportunity for integration of a laser sensor within living tissue, opening a new path at the interface between nanophotonics and medicine.

"If I have seen further it is by standing on the shoulders of Giants."

Isaac Newton. Letter from Sir Isaac Newton to Robert Hooke 1675.

Contents

1 Light interaction with matter

When light interacts with matter it can be scattered and absobed by the materials. In the absence of absorption the scattering event alters the k of light without changing the energy, this is called elastic scattering. According to the relative ratio of the scatterer size and the wavelength of light λ there are two scattering regimes we can discuss when considering elastic scattering. Rayleigh scattering occurs for small particles whose size is much smaller than the wavelength of light ($\lambda \gg a$). The light is isotopically and elastically scattered and its intensity is inversely proportional to λ^4, this is the well known reason for the sky being blue. Sunlight is scattered from molecules in the atmosphere and given the dependence on λ shorter wavelengths are scattered significantly more, giving the observer the impression that the sky is blue. Instead, Mie scattering occurs for particles whose size is comparable to the wavelength of incident light ($\lambda \sim a$), such as the scattering which occurs in clouds and brings about their white and non-transparent traits.

1.1 Single light scattering

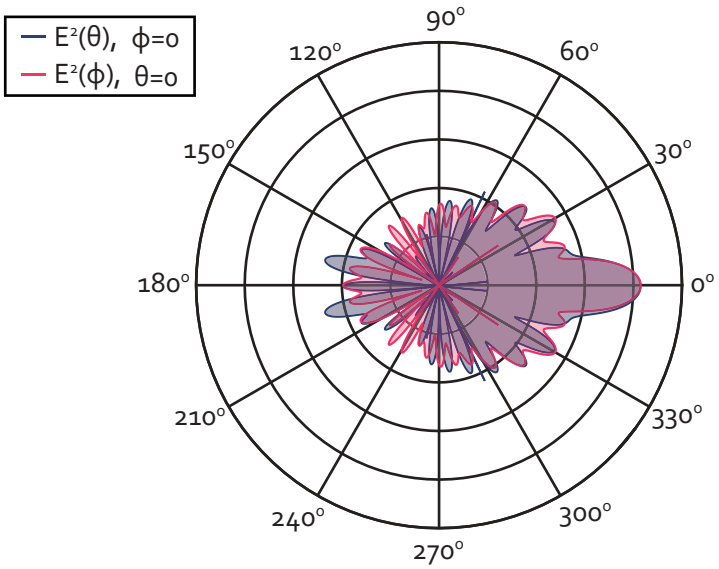

Figure 1.1: **Differential cross-section of a Mie sphere.** Logarithmic plot of the scattering cross-section of a Mie sphere in air of $d = 1.28\mu m$ and refractive index $n_{sphere} = 1.5$ in direction $\phi = 0^o$ (blue map) and $\theta = 0^o$ (pink map)

The regime in which light interacts only once with a scatterer is called single scattering. We will focus on single scattering of light from dielectric spheres where exact solutions have been obtained. To do so we will base calculations on Mie theory, developed by Gustav Mie in 1908 [1, 2], derived from Maxwell's electromagnetic theory.

We calculate the scattering cross section by using Mie theory in the approximation of independent scatterers. Mie theory as well as the independent scattering approximation has been used extensively and is described in the following references [2, 3] and developed for the work of Dr. Michele Gaio [4]. The following scattering map for a spherical particle of $d = 1.28\,\mu m$, $n_{sphere} = 1.5$ and incident wavelength $\lambda_0 = 532\,nm$ was obtained and is plotted in Figure 1.1 for $\phi = 0^o$ (blue map) and $\theta = 0^o$ (pink map) in logarithmic scale. Here θ is defined as the angle between x and y axis, while ϕ is the angle between z and y axis. Due to their size, Mie scattering objects can sustain optical resonances as evidenced in Figure 1.1. In Mie scattering the polarisability depends on the k -vectors and has a very complex function, as a result the scattering is more pronounced in the forward direction, as the forward scattering (0^o) is larger than in other directions, this feature increases with the particles size [2].

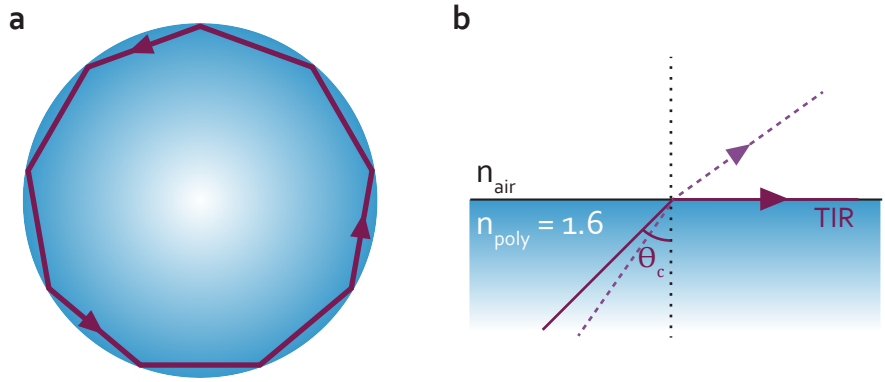

Figure 1.2: **Total internal reflection at an interface**. a) WGMs supported by a polymer sphere, reliant upon total internal reflection (TIR) at the interface between the sphere and the surrounding media. b) Schematic of TIR, which occurs when the angle with the normal is $\theta > \theta_c$

For large particles the optical modes are confined close to the sphere-air interface and are referred to as whispering gallery modes (WGMs). The ray-optics depicture of WGMs in a sphere is illustrated in Figure 1.2a, where the sphere's cross section is shown. WGMs arise due to total internal reflection of light, the schematic is showed in Figure 1.2b. Total internal reflection occurs when light strikes a boundary of lower refractive index at an angle θ larger than the critical angle θ_c with respect to the normal to the surface, which is given by:

$$\theta_c = \sin^{-1}\left(\frac{n_s(\omega)}{n_1(\omega)}\right) \tag{1.1}$$

Where the sphere's refractive index is n_1 and the refractive index of the surrounding media is n_s. In this condition light cannot be transmitted beyond the boundary and is entirely reflected with a given phase. This phenomena is the operating principal of many technological components, stemming from optical fibres and waveguides to total internal reflection fluorescence microscopy and sensing with WGM resonators [5, 6, 7, 8].

1.2 Multiple light scattering in disordered systems

In the previous section we focused on the single scattering regime where the scatterer is a single sphere. Here we will use the properties discussed previously to present multiple scattering where many scattering elements and events are considered.

When light propagates in a non-homogeneous medium with a randomly spatially vary-

ing dielectric function, also called a disordered media, light is scattered multiple times. Straight or ballistic propagation cannot on their own accurately describe the multiple scattering of light, depicted in Figure 1.3. Instead light propagation is analogous to the Brownian motion of particles in a liquid [9]. Light undergoes a random walk [10, 11] and can be accurately described as a diffusion process. For example paper is composed of randomly oriented fibres made of cellulose, these fibres are not completely compact. Due to the refractive index variation the light impinged on the surface is scattered numerous times and emerges from the material conserving the colour of the incident light, therefore a diffusive medium such as paper appears white in the absence of selective absorption. Recently white beetles were uncovered to have naturally occurring strongly scattering disordered structures in their scales to obtain an exceptionally bright whiteness [12, 13]. In fact most opaque materials owe their colour to multiple light scattering. Unlike structural colour found in most beetles as seen in reference [14], there is no evidence of periodicity.

Below we will briefly review the standard diffusion model used to quantitatively describe light transport in an isotropic random dielectric medium.

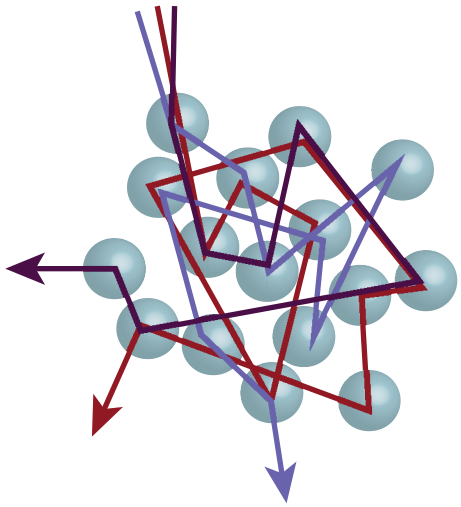

Figure 1.3: **Multiple scattering ray picture**. The grey spheroid represent the scattering centres, the different coloured beams represent different paths light could travel: multiple scattering of light.

1.2.1 The diffusion approximation

The solution to the Maxwell's equation for multiple scattering of light is very complex due to the shear number of scatterers. The simplest approach to model light transport, where

multiple scattering occurs, is the diffusion approximation [9, 11, 15]. This is achieved by imposing light continuity $I(\boldsymbol{r}, t)$ and, as an approximation, disregarding interference effects. In general, diffusive models are very appropriate for light propagation in clouds, foams, bones, paint, and the structures discussed here. One of the key parameters is the scattering mean free path ℓ_s, which is defined as the average distance between two scattering events and is given by:

$$\ell_s = \frac{1}{n_p \sigma_{sc}} \tag{1.2}$$

This quantity is related to the probability of a single scattering event, the scattering cross section: σ_{sc}, given by the integral of the differential scattering cross section:

$$\sigma_{sc} = \int_{4\pi} \frac{d\sigma(\theta, \phi)}{d\Omega} d\Omega \tag{1.3}$$

The total probability is given by the product of σ_{sc} and n_p; the density of scatterers.

The differential cross section in equation 1.3 is given by:

$$\frac{d\sigma}{d\Omega}(\overrightarrow{k_0}, \overrightarrow{\epsilon_0}; \overrightarrow{k}, \overrightarrow{\epsilon}) = \frac{a^2 I_s(\overrightarrow{k}, \overrightarrow{\epsilon})}{I_0(\overrightarrow{k_0}, \overrightarrow{\epsilon_0})} \tag{1.4}$$

Where $\overrightarrow{\epsilon_0}$, $\overrightarrow{\epsilon}$ and $\overrightarrow{k_0}$, $\overrightarrow{k}$, are the polarisation vectors and the wave vectors of the incident and scattered radiation respectively. Mie solution can be calculated explicitly from equation 1.4 and reduces to the Rayleigh scattering by using the Born approximation in the limit $\lambda \gg a$ [2]. The equation 1.4 becomes:

$$\frac{d\sigma}{d\Omega}(\theta) = \frac{k^4 a^6}{2} \mid \frac{\epsilon_r - 1}{\epsilon_r + 2} \mid^2 (1 + \cos^2 \theta) \tag{1.5}$$

Another characteristic length relevant in the multiple scattering regime is the transport mean free path ℓ_t which describes non-isotropic scattering such as the one illustrated in Figure 1.1. ℓ_t defines the average distance after which the propagation of the photon is completely randomised, or defined alternatively as when the intensity distribution becomes isotropic. ℓ_t is related to ℓ_s by the following expression:

$$\ell_t = \frac{\ell_s}{1 - g} \tag{1.6}$$

where $g = \langle \cos\theta \rangle$ is the average cosine of the scattering angle. For isotropic scattering the correction term is $g = 0$ and $\ell_t = \ell_s$. For non-isotropic scattering $g > 0$ and for a spherical particle g can be extracted from Mie theory.

The propagation of light in a disordered media is given by the diffusion equation:

$$S(\boldsymbol{r}, t) + \frac{\partial I(\boldsymbol{r}, t)}{\partial t} = D\nabla^2 I(\boldsymbol{r}, t) - \alpha v_E I(\boldsymbol{r}, t) \tag{1.7}$$

where $I(\boldsymbol{r}, t)$ is the radiation's intensity, D is the diffusion constant and is equal to: $D = \frac{\ell_s v_E}{3}$, $S(\boldsymbol{r}, t)$ describes the light source $\alpha = 1/\ell_a$ is the reciprocal of the absorption length. ℓ_a refers to the diffusive path length over which the intensity is attenuated by a factor of e and v_E is the energy velocity within the medium [15]. v_E is a quantity that describes the light transport in a diffusive media, in presence of strong resonances the energy velocity can be drastically altered [15, 16].

The majority of the absorbing materials attenuate light exponentially and satisfy the Lambert-Beer Law:

$$I(\lambda) = I_0(\lambda) e^{-\sigma_{abs}(\lambda) C L} \tag{1.8}$$

where σ_{abs} is the absorption cross section and can be expressed as in equation (1.2) but now in function of the number of absorbers and ℓ_a, C is the concentration of the absorbers, L is the sample thickness, I_0 is the incident light intensity and I is the intensity of transmitted light both at a given wavelength λ. ℓ_a is defined as [17]:

$$\ell_a = \sqrt{\frac{\ell_t \ell_i}{3}} \tag{1.9}$$

where ℓ_i is the average distance light propagates ballistically in a homogeneous medium before it is attenuated by a factor of e.

The diffusion approximation is valid if $L \gg \ell_t$, where the sample thickness should be large enough that many scattering events occur before the light exits the sample and memory of previous scattering events is lost. ℓ_t is also taken to be larger than λ, i.e. $k \times \ell_s \gg 1$ where k is the light wave vector [16].

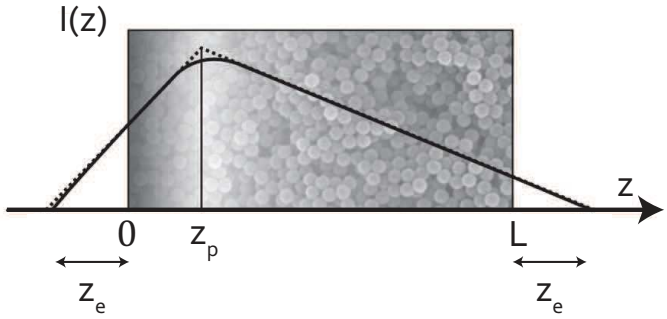

Figure 1.4: **Schematic plot of the light intensity vs. distance in a diffusive slab of photonic glass**. Adapted from [16]: The extrapolation length z_e and the penetration length z_p are shown.

Many of the samples treated in this work have a slab like geometry, which imposes certain boundary conditions on the diffusion approximation, illustrated in Figure 1.4. The system is considered infinite in the x and y direction and finite between $z = 0$ and $z = L$. A collimated beam is incident on the diffusive medium from the left, initially the light is ballistic and is dictated by the Lambert beer equation (1.8) after which the propagation is diffusive. A common assumption is to place $z = 0$ at the extrapolation length z_e. This is effectively represented by putting an exponential source or a delta function located at z_p, the penetration depth. The extrapolation length z_e, can be understood as the point where the light intensity is zero for a source inside the system.

The full solution of the stationary diffusion equation is obtained with boundary conditions considered in Figure 1.4. Additionally the light source is approximated by a delta function light source at z_p. The solution is expressed as the total transmission of light, defined as the total flux at $z = L$ and normalised by the source, as follows:

$$T(L,\lambda) \simeq \frac{1}{\alpha z_e} \frac{\sinh\left[\alpha\left(z_p + z_e\right)\right]\sinh\left(\alpha z_e\right)}{\sinh\left[\alpha\left(L + 2z_e\right)\right]} \tag{1.10}$$

with:

$$z_e = \frac{1}{2\alpha} \ln\left(\frac{1+\alpha z_0}{1-\alpha z_0}\right) \tag{1.11}$$

and:

$$z_0 = \frac{2}{3}\ell_t(\lambda)\left(\frac{1+R}{1-R}\right) \tag{1.12}$$

where R is the diffuse reflectivity of the sample. For a diffusive slab with filling fraction 0.55 and made with a typical biopolymer ($n \sim 1.55$) [18], $R \simeq 0.39$ when $m = {}^{n_{polymer}}/_{n_{air}} = 1.29$ [11, 19]. Figure 1.5 depicts the variation of the diffusive reflectivity as a function of the refractive index mismatch. In the shaded region we have depicted the range which include the polymers we will use throughout this thesis. From the lowest Bovine Serum Albuim (BSA) n = 1.43 to silk fibroin n∼1.55.

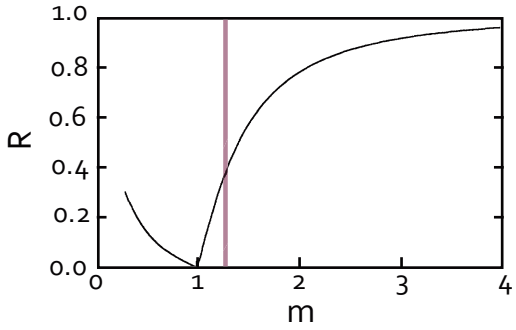

Figure 1.5: Reflectivity R as a function of refractive index mismatch, $m = {}^{n_{polymer}}/_{n_{medium}}$ where $n_{polymer}$ is the refractive index of the matrix and n_{medium} is the refractive index of the surrounding medium. The shaded region represents the polymers ranging from refractive indices: 1.45 - 1.6 and filling fraction 0.55. Figure adapted from [19].

Furthermore, for a slab like geometry, the parameters z_e and z_p are usually set to be identical. In absence of absorption the solution can be simplified to:

$$T(L, \lambda) \simeq \frac{2z_0}{L + 2z_0} \tag{1.13}$$

In electronic transport, doubling the thickness of the conductor halves the transmission, which is the Ohm's law. Here according to the optical Ohm's law [10, 20], the light transmission though a diffusive slab is directly proportional to the transport mean free path ℓ_t, and inversely proportional to the slab thickness:

$$T(\lambda) \sim \frac{\ell_t}{L} \tag{1.14}$$

With static experimental measurements of the total light transmission through a given slab with known thickness it is possible to obtain the absolute value of the transport mean free path, within the limits where the diffusion approximation is valid [11, 16].

1.2.2 The radiative transfer equation

For the scope of this thesis it is particularly useful to describe the transport of light in the dilute scattering regime, where the diffusion approximation is no longer valid, $L \sim \ell_t$ [21]. The radiative transfer equation (RTE) applied to light transport is valid spanning over a wide range of transport regimes, from the ballistic regime to the diffusive regime, while ignoring the phase of light and interference [22, 23].

The radiative transfer equation (RTE) is a mathematical description of the propagation of electromagnetic radiation through a medium in terms of the absorption, emission and scattering [21]. It has been used in many fields including astrophysics [24, 25], nuclear physics and bioimaging [26].

The basic quantity of RTE is the specific intensity L(**r**,**u**,t), from which the photon density irradiated at point **r**, propagating along **u** direction at time t, and describes the evolution in time and space of the averaged radiance, the energy flowing towards a given direction and at a given position and time.

In a system which exhibits absorption and scattering the the radiance is given by:

$$\frac{1}{c}\frac{\partial L}{\partial t}(\mathbf{r},\mathbf{u},\mathrm{t}) + \mathbf{u}\cdot\nabla \mathrm{L}(\mathbf{r},\mathbf{u},\mathrm{t}) = -\left(\alpha + \frac{\mathbf{1}}{\ell_{\mathrm{sc}}}\right)\mathrm{L}(\mathbf{r},\mathbf{u},\mathrm{t}) + \frac{1}{\ell_{sc}4\pi}\int_0^{4\pi} p(\mathbf{u},\mathbf{v})\,\mathrm{L}(\mathbf{r},\mathbf{u},\mathrm{t})d\Omega \quad (1.15)$$

where $p(\mathbf{u},\mathbf{v})$ describes the scattering angle. The solution of equation (1.15) describes the spatial field correlation transport in random media and can be derived from the Maxwell equations as well as from the Bethe-Salpter equation [27]. The solution converges to the diffusion approximation when $L \gg \ell_t$.

1.2.3 Measuring the transport mean free path

Static measurements of the transport mean free path (ℓ_t), defined in equation (1.6), are an important measure of the scattering strength of a disordered material and can be estimated experimentally in various ways. Photonic techniques such as coherent backscattering [28, 29] and total transmission of light [10, 30, 31] are commonly employed. In this thesis we use an integrating sphere to estimate the ℓ_t of our samples. An integrating sphere consists of a hollow cavity, where the interior is coated with a high diffusive material with

no absorption. A white light source (e.g. tungsten lamp) is collimated and directed at the sample surface at normal incidence. When shining light on a disordered medium, the spatial in-homogeneity of the refractive index prohibits a straight-line propagation, forcing the wave instead to scatter in all available directions. The light exiting the sample from the bottom surface is collected by the integrating sphere.

The radiation introduced into the integrating sphere hits the reflective walls and is multiply scattered. After a number of reflections the radiation is dispersed uniformly. In this manner the flux which exits the sample is collected by the detector and the integrated intensity is proportional to the initial radiation exiting the sample.

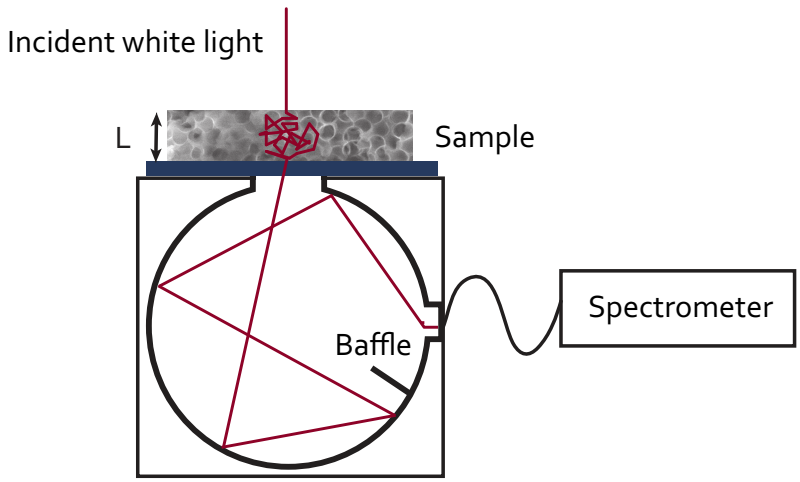

Figure 1.6: **Schematic of an integrating sphere.** White light is incident on a sample, diffuses within the sample and the light which exits the back of the sample is collected by the integrating sphere. The interior of the integrating sphere allows light to be scattered with minimal losses until it is directed to the spectrometer and acquired.

The light is then sent to a fibre which is coupled to a spectrometer. The baffle, illustrated in Figure 1.6, is coated with the same material as the rest of the sphere and blocks the direct incident light, preventing it from reaching the detector. The final intensity is normalised by the intensity in absence of the disordered media and the transmission is extracted for a given sample thickness and wavelength. The photonic Ohm's law [10, 20] which is described by the change in total transmission (T) as a function of the sample thickness (L), is obtained via the stationary solution of the diffusion equation, equations 1.10 and 1.13 for transmission with and without absorption respectively [10, 16]. By measuring samples

of different thickness spectrally and fitting the data points to equation 1.10 we can obtain ℓ_t. The sample is optically thick, therefore it is assumed that only diffusive light enters the integrating sphere.

1.3 Polymer sphere assemblies as strongly scattering materials

A dielectric sphere with a size comparable to the wavelength of light is a good building block to create highly scattering systems. This simple polymer beads can self-assemble into two opposing systems, an ordered arrangement called photonic crystal and a completely random arrangement called a photonic glass.

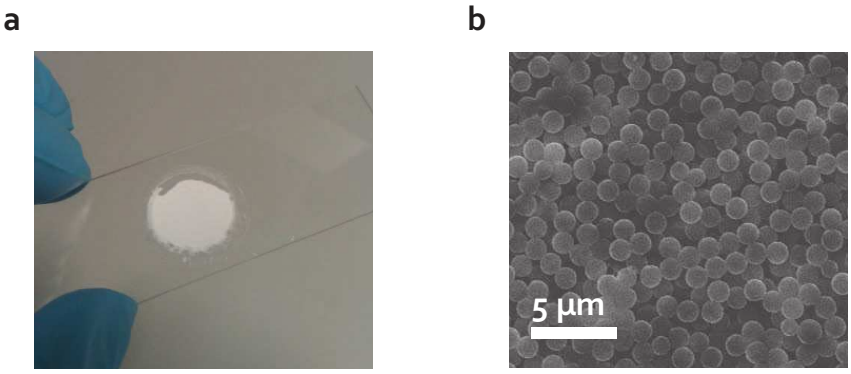

Figure 1.7: **Photonic glass** a) A photo of a fabricated photonic glass made with polystyrene spheres. b) the respective SEM of the surface of the photonic glass.

Photonic crystals have a periodically varying dielectric functions $\epsilon(\mathbf{r})$ which carry many interesting properties for photonics, such as a photonic band gap where light of certain wavelength are forbidden to propagate [32, 33], which are particularly useful for anti reflection coatings and waveguiding [34].

Photonic crystals made from monodisperse polymer microspheres can be understood theoretically as the packing of hard spheres. The packing efficiency can be defined by the ratio of particle volume with respect to the total volume; this is called the packing fraction or filling fraction. For photonic crystals the densest regular packing of monodisperse hard spheres is achieved for a face centred arrangement with a theoretical packing limit of 0.74 and void fraction of 0.26 [35, 36].

Photonic glasses, on the other hand, have randomly varying $\epsilon(\mathbf{r})$. Applications of this technology range from coherent light backscattering,[28, 37] random lasing [9], strong light localisation [38] and long-range intensity correlations [39]. The maximum packing fraction for random hard spheres is theoretically predicted to be 0.64 [40, 41], lower than that of photonic crystal for equal building blocks. An example of a photonic glass made with monodisperse microsphere is illustrated in the picture in Figure 1.7a and the corresponding scanning electron microscope (SEM) image is shown in Figure 1.7b [42].

Both arrangements can be accomplished by self-assembly of a colloidal suspension of polymer spheres [43]. A colloid is defined as a two phase or more system where one is composed of small particles, which can be between 1 nm and several microns in size and are dispersed in a second substance. Their properties differ from bulk materials due to their large surface to volume ratio. Here we are focusing on the self assembly of monodisperse polystyrene (PS) beads between $200\,nm$ and $2\,\mu m$, obtained via the Goodwin method [44], giving rise to a negative surface charge of the particles.

1.3.1 Direct photonic glasses

Colloidal stability or lack thereof are the key to obtaining photonic crystals and photonic glasses respectively. Specifically, vertical deposition method has been widely used to fabricate 3D photonic crystals [45], although other methods yield similar results [46]. In this technique a clean hydrophilisised microscope slide is placed in a container with the colloidal suspension. A meniscus is formed between the solution and the substrate, such that the spheres are allowed to self assemble. In order to construct photonic glasses the ordered assembly should be prevented; it is then necessary to force the flocculation of the spheres. Flocculation is the process where colloids break their colloidal equilibrium and form clusters of particles. For PS particles, once the cluster is large enough to fight the buoyancy forces the cluster sediments, settling to the bottom of the container. As mentioned previously, the spheres are negatively charged and therefore repel each other. Adding positive electrolytes ensures the instability of the colloid by charge screening, in our case this is achieved by adding an acid, hydrochloric acid (HCl), which dissociates in solution giving rise to the charges necessary. The suppression of the repulsion potential leads to attractive van de Waals forces between spheres [16], this step ensures a random packing of the spheres and avoids the formation of an opal structure [43]. The typical filling fraction obtained for a

photonic glass is 0.45-0.55 smaller than the theoretical limit of 0.64 [42]. Given the disordered nature of the photonic glass it appears white as seen in the picture in Figure 1.7. The fabrication procedure for a photonic glass made with monodisperse polymer beads is well documented [42, 43].

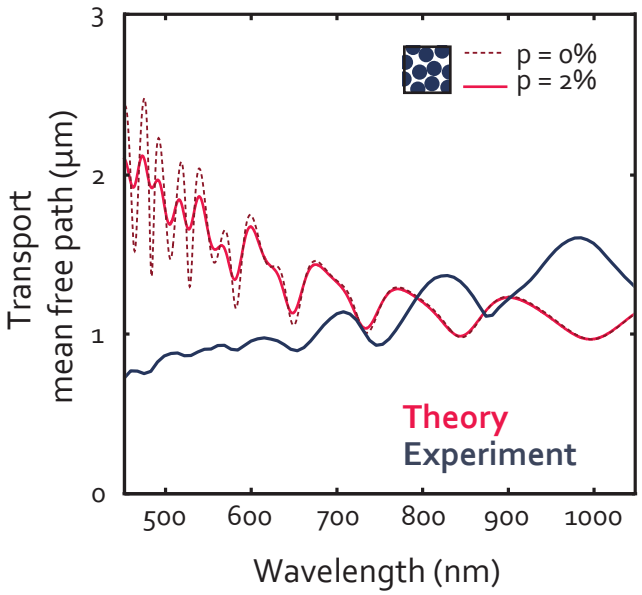

Figure 1.8: **Transport mean free path of photonic glasses.** The photonic glasses are made with Polystyrene beads of diameter d= 1270 *nm*. Experimental results obtain from 5 photonic glasses of different thickness, full blue line. Theoretical calculation of the transport mean free path is depicted by the full pink line, for spheres of d= 1270 *nm* and refractive index $n_{ps} = 1.6$ using the single particle approximation assuming a filling fraction of $f = 0.55$ assuming a 2% polydispersity of the polymer spheres used. In dashed pink is assuming the spheres are monodisperse.

The transport mean free path of photonic glasses can be determined experimentally, using the integrating sphere and theoretically via the Mie theory in the independent particle approximation. The results are plotted in Figure 1.8 where the blue line is the experimentally obtained transport mean free path. The pink lines are the theoretical results, assuming no polydispersity of the sphere (dashed curve) and assuming a polydispersity of 2% for d= 1.27 μm (full curve), which is a realistic polydispersity of the colloidal spheres used throughout this thesis. Since the building blocks are of spherical nature, Mie resonances at certain wavelengths are observed illustrated in Figure 1.8. The minima in ℓ_t correspond to the λ of light which are more confined in the photonic glasses. The polydispersity of microspheres leads to a change and a smearing of the resonances. The mismatch between

the theoretical and the experimental resonances, is accredited to the independent scattering approximation. The approximation describes a single sphere in an effective refractive index, in contrast to the packed photonic glass while also neglecting interference of light. Additionally, the small underestimation of the transport mean free path is due to an overestimation of the thickness as PS spheres left a thin lining on the container after dying. Similar results can be see in the following reference: [16].

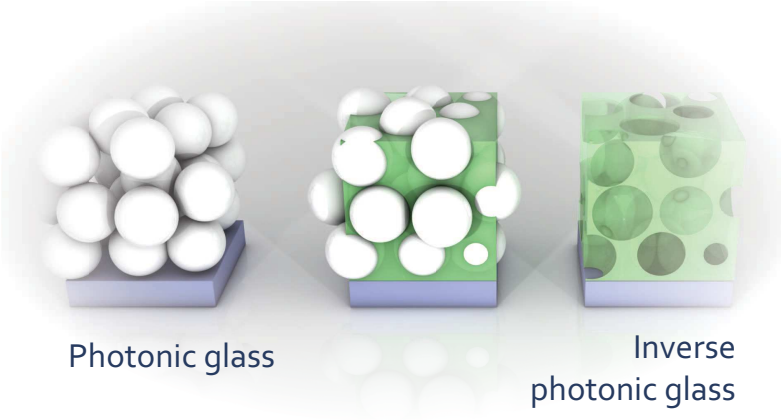

Figure 1.9: **Fabrication steps of an inverse photonic glass.** The different fabrication steps, from a conventional photonic glass containing PS beads to the inverse photonic glass made solely out of polymer.

1.3.2 Inverse photonic glass

Photonic glasses discussed previously rely on simple self-assembly of monodisperse polymer spheres to yield highly scattering bodies with $\ell_t > 3\ \mu m$. The method is very simple and cheap, but cannot easily be made with many types of biomaterials. To overcome this bottleneck we use the photonic glasses made with polymer beads as a template to nanostructure natural polymers. When successful, this leads a nanostructured biopolymer with disordered air voids as illustrated in Figure 1.9. This assembly has been dubed inverse photonic glass as what is left is the negative imprint of the photonic glass sphere assembly, analogous to opals and inverse opals [47, 48]. Here the photonic crystals are infiltrated with a polymer of choice followed by the selective etching of the monodisperse ordered spheres. Fabrication of an inverse photonic glasses will be exploited in the next chapter.

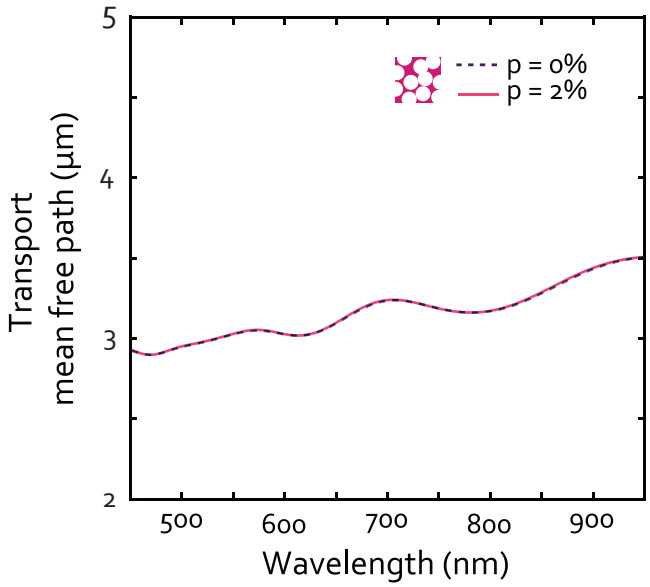

Figure 1.10: **Theoretical transport mean free path calculated for air spheres in a polymer matrix** $n_{polymer} = 1.6$ at a filling fraction of $f = 0.55$ as a function of wavelength (full red line) assuming polydispersity of 2% (dashed black line).

An inverse photonic glass containing spherical air voids of lower refractive index than their surroundings is expected to provide less scattering and therefore a higher ℓ_t than its direct counterpart. Employing the same calculation tools used to calculate the ℓ_t of a photonic glass, we calculate the ℓ_t for an inverse photonic glass of an arbitrary polymer with $n_{polymer} = 1.55$, without absorption, assuming a filling fraction of $f = 0.55$ and taking into account a polydispersity of 2%. From these parameters we obtain an average ℓ_t over visible wavelengths of $\sim 4\mu m$, plotted in Figure 1.10. In an inverse photonic glass assembly where the interconnected holes have low refractive index and the surrounding refractive index is higher, Mie resonances are weak and scattering is reduced. Consequently, the resonant modulation of ℓ_t is washed out and the average ℓ_t is larger as seen in Figure 1.10, when compared to the highly resonant ℓ_t transport for a photonic glass, Figure 1.8. For equal filling fraction and refractive index contrast the ℓ_t increases approximately 2 fold. Another important parameter which can affect the ℓ_t is the packing of the spheres, well packed spheres ($f = 0.55$) yields a lower ℓ_t as illustrated in Figure 1.11. As mentioned before, from the literature on photonic glasses we can expect a filling fraction $f = 0.45-0.55$ [42], in this window the variation of the ℓ_t for both the direct photonic glass and its inverse is small. This results from the definition of scattering in equation 1.2 where the density of

scatterers is inversely proportional to the scattering mean free path.

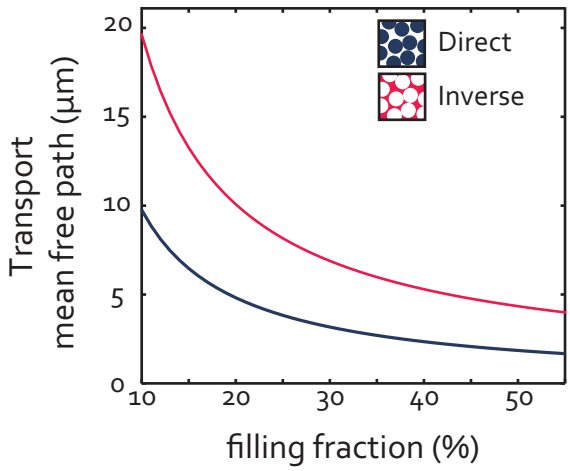

Figure 1.11: **Filling fraction and transport properties of direct and inverse photonic glasses.** The relation of the filling fraction and the transport mean free path for direct photonic glass (Blue line) and the inverse photonic glass (Pink line) for $n_{media} = 1.55$, $\lambda = 600$ nm and size of spheres and voids $d = 1.27\mu m$.

1.4 Lasing action

Lasers are devices which generate and amplify light radiation by stimulated emission. Light originating from a laser has remarkable properties. Generally the beam is directional, has large spectral purity and high brightness. The first laser cavity was developed in 1960 [49], since then many other types of lasers have emerged, and its technology is still in development today: nanowire lasers [50, 51], quantum cascade lasers [52], spasers [53, 54, 55] and Biolasers [56] continues to spark interest in the scientific community.

For the scope of this thesis, biolasers are of specific interest. We can define a biolaser as a laser made from biological materials. They have the potential to produce new coherent light sources, flexible and compatible with living tissue integration. Biocompatible lasers are attracting attention for their potential to harness the amplifying power of stimulated emission for biosensing and cell tagging and tracking [8]. Despite the different geometries and sizes, to operate effectively any lasers requires three essential elements, i) a laser medium also known as the gain medium, which range from semiconducting crystals to gas molecules, ii) a pump, a manner to excite the gain medium and iii) method of optical trapping that allows the radiation to pass through the laser medium several times.

1.4.1 Organic dyes as gain media

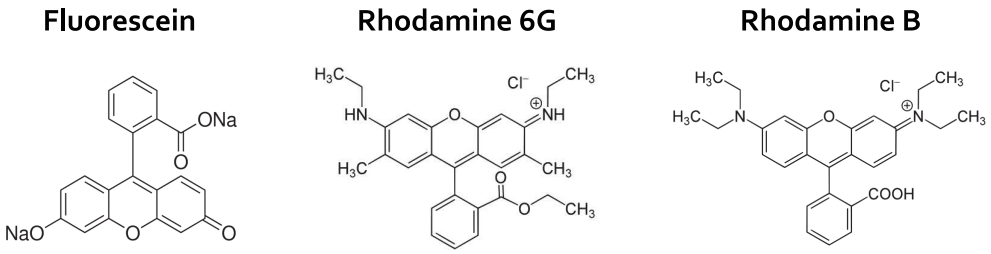

Figure 1.12: **Chemical structure of gain molecules.** From the left, fluorescein, rhodamine 6G and rhodamine B.

Optical gain can be obtained from a variety of sources such as atoms (e.g. HeNe laser), [57] molecules (e.g. CO_2 laser) [58], dielectric solids (e.g. the Nd:YAG laser) [59], semiconductor materials such as perovskites [60] and organic molecules [61] such as rhodamines. We focused on organic dyes as a source of gain, due to their compatibility with the biopolymers used and their relatively low-toxicity.

Organic dyes have been employed as the gain media of dye lasers since their discovery in the 1960s. Typically in liquid form, the laser dye was recirculated, reducing dye photobleaching when compared to its solid state laser counterpart. Additionally dye lasers often allowed a wavelength tuning range of 50 -100 nm [62]. Dye lasers have since then been largely replaced by solid-state lasers, which can be smaller and much easier to operate. However, recently organic dyes employed as gain have been used for several miniaturised organic lasers and hold promise in biointegration, sensing, and lab-on-chip applications.

The gain molecules used throughout the scope of this thesis are depicted in Figure 1.12. Sodium fluorescein, represented in Figure 1.12a, is a biocompatible laser dye used for diagnostic purposes. For example fluorescein angiography is used to diagnose vascular disorders in the human eye [63], for neurosurgery to detect cerebrospinal fluid leaks and to identify ventricular septal defects in the heart [64]. Additionally in Figure 1.12 b is rhodamine 6G (Rh6G), and in Figure 1.12c, rhodamine B (RhB), both are conventional laser dyes [61]. RhB has been used to stain cells and used as a mitochondrial membrane potential probe.

Spontaneous emission is the process in which the system spontaneously decays from an excited state to a lower energy state by releasing energy in form of a photon [49].

Fluorescence is a subset of spontaneous emission which stems from the absorption of a photon to an excited quantum state and subsequent relaxation after a certain time and emission of a photon. The time-lag between the absorption and emission of a photon is called fluorescence lifetime (τ).

In fluorescence, the spontaneous emission from the ensemble is broad like in spectral emission and emerges randomly in all directions. Additionally, there is another downward relaxation mechanism called nonradiative relaxation, whereby the energy is emitted as phonons or heating rather than as electromagnetic radiation.

The quantum yield of fluorescence, ϕ, is defined as the ratio of the total number of emitted photons to the number of molecules promoted to the exited state and is given by:

$$\phi = \frac{\Gamma_r}{\Gamma_r + \Gamma_{nr}} \tag{1.16}$$

and fluorescence lifetime is given by:

$$\tau = (\Gamma_r + \Gamma_{nr})^{-1}. \tag{1.17}$$

where Γ_r is the radiative decay rate and Γ_{nr} is the non-radiative decay rate. The lifetime of a molecule can be estimated from the Strickler-Berg equation found in reference [65].

The lifetime of organic molecules is typically of the order of a few ns, but can be as short as 0.3 ns for Coumarine 6 and as long as 90 ns for Pyrene [66]. An example of a fluorescence lifetime decay for a single Rh6G molecule in a polymer film is depicted in Figure 1.13. This property is intrinsic to the chemical structure of the molecule as well as its environment and therefore is a important tool to measure properties such as: temperature, polarity, viscocity, voltage amongst many others [66].

Having introduced spontaneous decay we will now focus on stimulated transition, essential for the function of lasers. Stimulated emission is a process where an incoming photon interacts with an electron in the excited state, perturbing it and causing it to decay to a lower energy state through the emission of a photon as illustrated in Figure 1.14. The emitted photon is identical to the incident photon with respect to the polarisation, phase, wavelength and direction.

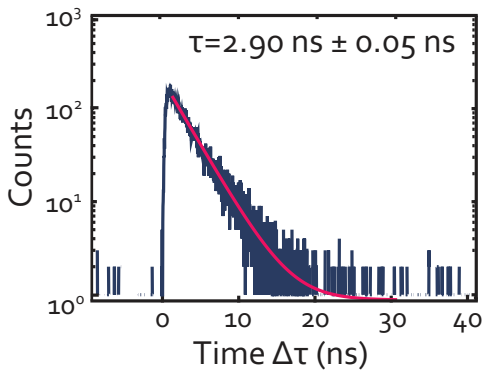

Figure 1.13: **Fluorescence lifetime.** Single molecule life-time of rhodamine 6G in a PVA film.

Spontaneous emission probability is proportional to the population in the excited state N_2, while the probability is not influenced by the population of the lower states (N_1 and N_0 depicted in Figure 1.14). Conversely, this does not hold for stimulated emission since the process which interacts with the excited state causing it to relax downwards can equally cause it to transition upwards from a lower energy state, called stimulated absorption. For a two-level system the probability of both transitions are identical. In order to have a net stimulated emission, there has to be a condition of population inversion, in which more fluorophores are in the excited state than in the ground state. A four-level lasing system represented in Figure 1.14 is a realistic description of many lasers.

In this model a certain photon density W_p excites the fluorophores into a vibrational levels of the excited state, where their population is represented by N_3 and can accumulate. They relax down to the lowest vibrational level of the singlet state via internal conversion. Radiative transitions occur from level 2 to level 1, by spontaneous or stimulated emission (W_e) into a upper vibrational state of the lower singlet state, which by internal conversion can relax to the lowest vibrational state. Stimulated emission provides the gain of a laser, in other words its ability to amplify light. A laser with molecular transitions can be described by a simplified 4 level model [49] as follows:

$$\frac{\partial N_1}{\partial t} = \sigma_a N_2 W_e v - \sigma_e N_1 W_p v + \frac{N_2}{\tau_r} \tag{1.18}$$

where N_1 and N_2 are the populations of energy levels 1 and 2 respectively, σ_a is the absorption cross section at the pump wavelength; σ_e is the stimulated emission cross section, v is the velocity of light inside the medium. The gain molecules chosen have a large stimulated

emission cross sections in the order of $10^{-22}\,m^{-2}$.

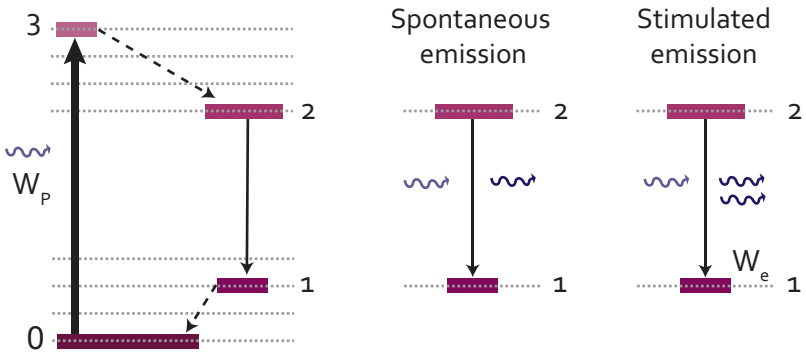

Figure 1.14: **Radiative and non-radiative transitions in a four level system**. Straight black arrows: radiative transitions. Dark blue arrows: incident radiation and output radiation. Purple bars: population level.

1.4.2 Conventional lasing geometries

The optical trapping and consequent recirculation of photons in the gain media ensures that enough amplification can take place to counter balance the losses incurred by the system. This is conventionally achieved by cavities such as Fabry-Perot cavity illustrated in Figure 1.15.

Fabry-Perot Laser

A Fabry-Perot cavity is a resonant cavity for light composed of two planar parallel highly reflecting mirrors where light bounces back a forth between the mirrors forming a standing wave. The clearing between the mirrors is the gain region. Here, upon excitation there is a non-zero probability that a small amount of spontaneous emission starts along the axis of the device, schematically illustrated in Figure 1.15a. The signal is amplified as the photons travel towards the mirror where they get reflected back and re-amplified as it passes back through the gain media towards the second mirror and then again reflected. When the gain outweighs the cavity losses it will eventually become a coherent oscillation; this is dubbed the laser threshold. The interplay between the gain spectrum, represented by the Gaussian profile in Figure 1.15b and the distance between the mirror dictates the laser output schematically represented in Figure 1.15b in pink, while the reflectivity of the mirrors impact the width of the peaks.

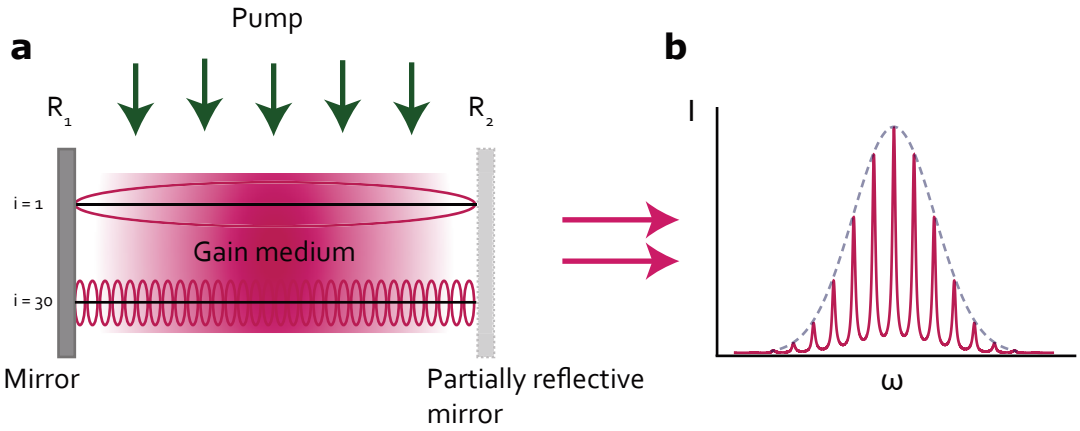

Figure 1.15: **Fabry-Perot laser**. a) is the schematic of the cavity, formed of two mirrors with reflectivity R_1 and R_2, a gain medium represented in pink between the two mirrors and a pump represented by the green arrows. b) Output of a typical Fabry-Perot cavity with gain, where the dashed plot represent the gain curve.

The requirement of constructive interference determine the resonant frequencies of the cavity. The phase condition is given by:

$$\phi(\omega) \equiv \frac{2\omega L n_1}{c} \tag{1.19}$$

where the resonant frequencies are given by:

$$\omega_m = m\frac{2\pi c}{2Ln_1} \tag{1.20}$$

and the mode spacing is:

$$\Delta\omega \equiv \omega_{m+1} - \omega_m = \frac{2\pi c}{2Ln_1} \tag{1.21}$$

where m is the mode number, L is the cavity length, c is the velocity of light in vacuum and n_1 the refractive index of the gain medium.

Only light in the resonant frequencies is amplified as it has a long dwell time in the cavity. The gain is generally represented as a medium with negative absorption. The threshold condition is given by:

$$R_1 R_2 e^{2Lg} = 1 \tag{1.22}$$

where R_1 and R_2 represent the mirror reflectivities, g is the gain coefficient with dimensions of inverse length.

One of the most important parameters to describe the performance of a resonator is the quality factor, commonly know at the Q-factor defined as:

$$Q = 2\pi \frac{Stored\ energy}{Power\ loss} \tag{1.23}$$

The Q-factor is a measure of the characteristic time for the decay of the energy stored in the resonator in units of 2π, full field oscillations. Another way of writing the Q-factor is by means of the ratio between the cavity resonant frequency ω and the full width at half maximum (FWHM) of the peaks $\delta\omega$.

$$Q = \frac{\omega}{\delta\omega} \tag{1.24}$$

Therefore, for larger Q-factor energy is stored inside the cavity for longer and the modes sustained are fed with more energy than for an equal pump power.

Whispering gallery mode Laser

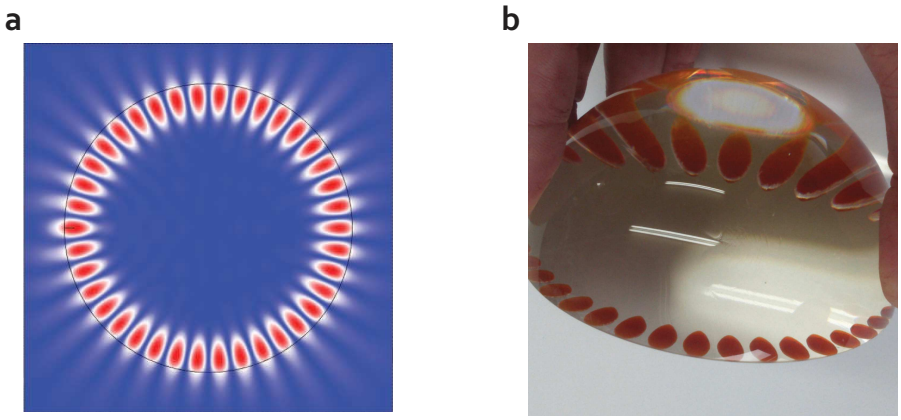

Figure 1.16: **Wave picture of light confinement in a microsphere resonator**. a) Microsphere cross section depicting WGM where high electric field intensity is depicted in red. b) Artistic construction of microsphere resonator illustrating WGMs in orange, courtesy of Shelly James.

Fabry Perot resonators are commonly utilised as laser cavities in commercial lasers. In the context of biolasers they have been used with cells to do lasing experiments with outlook for intracellular sensing [67, 68, 69]. They have great potential for in-vitro sensing and

on-chip sensing. However, for biolasing within the human body Fabry-perot cavities are far from ideal as they are bulky, require toxic materials or materials which cannot degrade naturally in tissues and are very susceptible to misalignment.

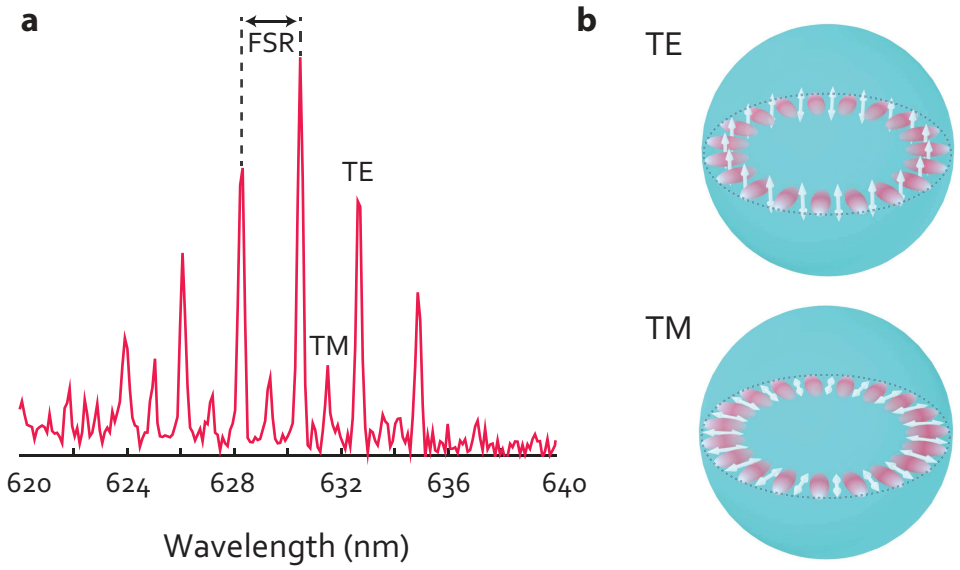

Figure 1.17: **Transverse electric (TE) and transverse magnetic (TM) polarised modes in a WGM laser.** a) TE and TM modes are identified for a typical laser WGM laser plot. The free spectral range is shown for TE modes. b) Schematic of the TE and TM mode in a WGM sphere.

Whispering gallery mode (WGM) lasers are micron-sized resonators with cylindrical symmetry and optical gain. In this thesis we will address a class of WGM laser, microcavities based on microspheres. Microsphere lasers benefit from small mode volumes, low losses, they can be made with less toxic materials while still sustaining lasing at low threshold and narrow linewidth with high Q-factors [70] without the need for mirrors. In order to achieve a high light intensity in a cavity, strong confinement is required. In this type of resonator the light is confined via total internal reflection as illustrated in Figure 1.16, along the equatorial plane of the microsphere. Light within the microsphere has an evanescent tail extending into the surrounding media enabling strong interaction between the light and the objects in the cavity mode volume. For example in the presence of a gold nanorod, microspheres have been shown to achieve single molecule sensitivity [6, 71]. Therefore, WGM resonators are very suitable as laser cavities for low threshold lasing. Details of different fabrication techniques, materials (solid and liquid) and different WGM geometries is extensively covered in the following reviews[72, 73, 74].

Gain can be introduced in WGM microspheres by adding active materials such as organic

molecules and Quantum dots in a host material. Polymers as host materials are an attractive option for biocompatible gain molecules as many can be dissolved in the polymer host or coated on the surface. Laser emission has been demonstrated in polymer microspheres [75, 76, 77]. Recently they were engulfed by various types of cells and shown to lase within a cell opening doors for cell tagging, tracking and inference of cellular internal stress [8, 78].

Similar to Fabry-Perot cavities, WGM lasers also have resonance conditions instead depending on the microsphere perimeter P and are as follows:

$$\phi(\omega) \equiv \frac{\omega P n_1}{c} \tag{1.25}$$

$$\omega_m = m\frac{2\pi c}{P n_1} \tag{1.26}$$

$$\Delta\omega = \frac{2\pi c}{P n_1} \tag{1.27}$$

A typical lasing spectra obtained from a polymer microsphere is illustrated in Figure 1.17 a. Two distinct polarisations can be supported in spherical resonator, transverse electric (TE) and transverse magnetic (TM) polarised modes depicted in Figure 1.17 b.

For a given resonator there are several modes accessible. A mode is characterised by its mode number which is approximately the number of wavelengths within the cavity. While, for large systems the number of modes is very large, such that counting modes is cumbersome, for microspheres of μm size instead a countable number of modes exists.

Another important parameter to characterise a microcavity is the Free spectral range (FSR). FSR is defined as the wavelength or frequency spacing between a mode m and its neighbouring mode $m+1$ [73], exemplified in Figure 1.17a between two TE modes. FSR is given by:

$$FSR = \frac{\lambda^2}{\pi n_1 D} \tag{1.28}$$

where λ is the resonant wavelength, n_1 is the refractive index of the microsphere and D is the spherical cavity diameter.

The positions of the microsphere's resonances (TE and TM modes) can be matched to

theoretical WGM values using the Lorenz-Mie calculations [79, 80], for a mode order p which accounts for the number of modes along the radial direction and mode number m to be:

$$\lambda^{-1} = \frac{1}{\pi n_1 D}\left[m + \frac{1}{2} + 2^{-1/3}\alpha(p)\left(m+\frac{1}{2}\right)^{1/3} - \frac{L}{\left(n_r^2-1\right)^{1/2}} + \right.$$

$$\left. + \frac{3}{10}2^{-2/3}\alpha^2(p)\left(m+\frac{1}{2}\right)^{-1/3} - 2^{-1/3}L\left(n_r^2 - \frac{2}{3}L^2\right)\frac{\alpha(p)\left(m+\frac{1}{2}\right)^{-2/3}}{\left(n_r^2-1\right)^{3/2}}\right] \tag{1.29}$$

where

$$L = \begin{cases} n_r & \text{for TE modes} \\ \\ 1/n_r & \text{for TM modes} \end{cases}$$

and $\alpha(p)$ are the roots of the Airy function and the refractive index mismatch is given by: $n_r = {}^{n_1}/_{n_S}$with n_s denoting the surrounding media of the cavity.

1.4.3 Unconventional lasing geometries: random laser

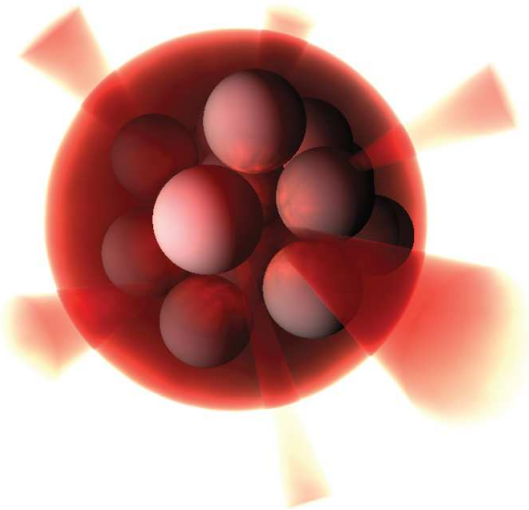

Figure 1.18: **Artist illustration of a random laser.** The light is multiple scattered between the spheres in the gain medium in red. The lasing emission is isotropic.

Laser emission is not limited to linear or circular resonators. When multiple scattering is combined with a gain medium it is possible to observe lasing action in a process called random lasing. Random lasers are cavity-less lasers, and instead use a disordered gain medium to trap light and create favourable conditions for lasing, as schematically illustrated in Figure 1.18. The resulting light emission is isotropic and can fall short of the monochromatic of high Q-factor lasers, but the threshold behaviour, the photon statistics and relaxation oscillations are very similar to those of standard lasers [9].

Random lasing was first proposed theoretically in the late 1960s by Letokhov [81] and then experimentally in 1994 by Lawandy and his colleagues from suspended nanoparticles in a solution of laser dye [82]. Letokov argued that for diffusion with amplification, the gain is proportional to the volume (αR^3) while the losses related to the escape of photons is proportional to its surface (αR^2). Therefore, there is a critical volume or a critical length (for a slab geometry) below which the losses exceeds the gain available and the system cannot lase. The relations are dependent on the scattering and the gain and given by:

$$V_{cr} \approx \left(\frac{\ell_t \ell_g}{3} \right)^{\frac{3}{2}} \tag{1.30}$$

$$L_{cr} = \pi \sqrt{\frac{\ell_t \ell_g}{3}} \tag{1.31}$$

where

$$\ell_g = \frac{1}{n_p \sigma_e} \tag{1.32}$$

While high-Q cavities favour lasing, their precise geometry limits the applications for dynamic systems like living tissues. Instead, random lasing is emerging as a simple, robust, and easy to integrate, source of stimulated radiation. Random lasing can be obtained in a variety of media [83], including organic materials such as cellulose [84, 85], and biological tissues [86, 87] and geometries such as: random fibre networks [88, 89, 90] and photonic glasses [91, 92] as well as many others [93, 94, 95]. Moreover, it is not influenced by the material's overall shape but instead relies on its internal heterogeneity, therefore it can easily adapt to biological media with the ability to withstand stretching, wetness, and heat. Its form is naturally biocompatible.

Given the diversity of random lasers studied it is important to clarify what constitutes

as a random laser. Firstly, light must be multiply scattered in the random laser as a result of the randomness of the material and amplified by stimulated emission. Secondly, the output of the laser is characterised by a threshold owing to the multiple scattering, above which the gain outweighs the losses [9].

As discussed before, the diffusion approximation is an accurate model for multiple scattering. This approximation holds for diffusion with gain [4, 96, 97]. The diffusion equations for typical experimental configurations are described in reference [4].

For a system of randomly varying refractive index, the gain is represented by a positive imaginary part. Deriving from the limitations of the diffusion approximation, the model described neglects the fact that for light rays in a random laser, when they undergo a random walk, are subject to interference effects.

The optical gain is described by the stimulated emission cross-section σ_e, the absorption cross-section σ_a and the excited lifetime τ. The pump, W_p brings the gain to the excited state labelled N_1, while the total density of gain molecules is N and the emitted light is given by W^i. The equations are coupled to a four-level system described in equation 1.18. The set of equations are the following:

$$\frac{\partial N_1}{\partial t} = \sigma_a W_p [N - N_1] v - \sum_i \sigma_e^i W^i N_1 v - \frac{N_1}{\tau_r} \tag{1.33}$$

$$\frac{\partial W_p}{\partial t} = D \frac{\partial^2 W_p}{\partial x^2} - \sigma_a W_p [N - N_1] v + \frac{I_p}{I_s} \tag{1.34}$$

$$\frac{\partial W^i}{\partial t} = D \frac{\partial^2 W_i}{\partial x^2} - \sigma_e^i W^i N_1 v + \frac{\beta^i}{\tau} N_1 \tag{1.35}$$

The emitted light is discritised spectrally by λ_i . The typical laser output can be seen in Figure 1.19a and 1.19b which plots the theoretical evolution of both the full width half maximum (FWHM) and the peak intensity as a function of increased pump power, as well as the spectral output below and above threshold. At low pump power fluorescence emission is observed where the spectra is broad ∼40 nm (blue open circles) and the peak intensity grows linearly with increase pump power (dark red circles). At threshold a change in the linearity of the peak intensity is observed. Above threshold stimulated emission is prevalent and a subsequent narrowing of the FWHM occurs. The threshold behaviour constitutes and

the narrowing of the linewidth are two important proofs of lasing operation and important indicators and terms of comparison of lasing efficiency.

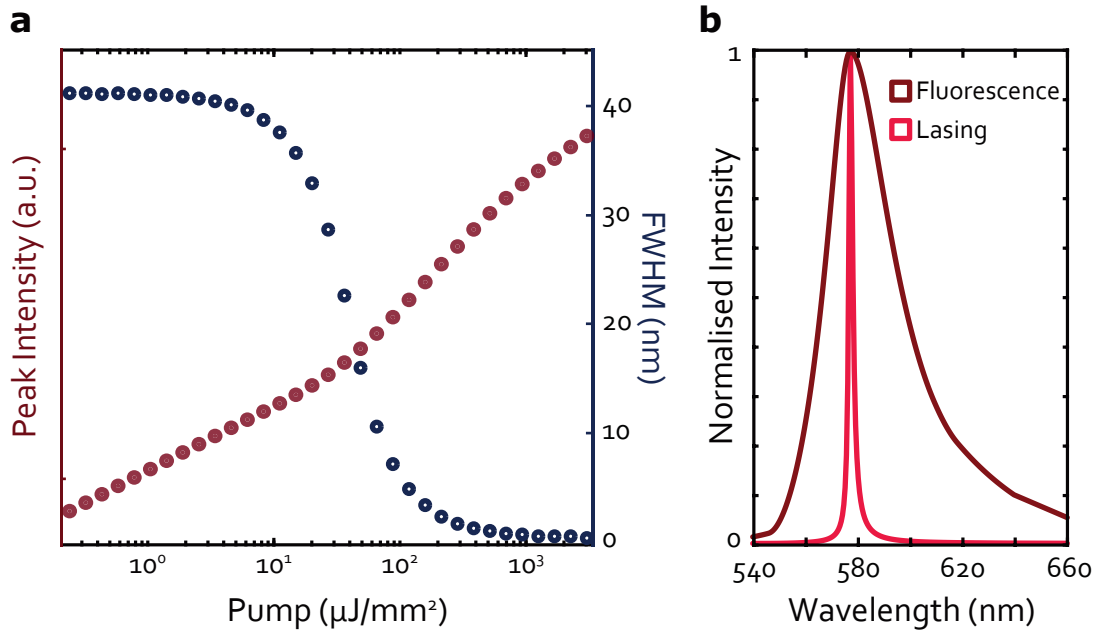

Figure 1.19: **Solution of the random laser model**. Assuming a solution of TiO_2 particles in ethanol with 1mM of RhB with $\ell_t = 1.5\,\mu m$ and a pump duration of $6\,ns$. a) The blue open circles represent the collapse of the FWHM from $\sim 40\,nm$ to $\sim 1\,nm$. The dark red full circles represent the evolution of the peak intensity with increasing pump power. b) The spectra in below threshold (dark) and above threshold (light) is depicted.

Given that the modes of a random laser are given by multiple scattering of light in a random media, a diffusive random laser is spectrally distinct from a resonant cavity spectra observed in Figure 1.15b.

Radiative transfer equation with gain

For the quasi ballistic regime, where $L \sim \ell_t$ the transport of light cannot be described by the diffusion equation, which diverges from the correct solution. Instead the transport of light described by RTE holds valid. The RTE for random lasers is described in the following reference [98]. We will use the solution for a 3D sphere one obtain the critical radius for the laser threshold to describe the limiting volume of a spherical random laser [22, 99, 100]. For parameters ℓ_{sc} and ℓ_g the critical radius of a sphere can be calculated by solving:

$$\tan(qR_{cr}) = \frac{2qR_{cr}}{2 - q^2 R_{cr} \ell_g} \tag{1.36}$$

with

$$q^2 = \frac{3}{\ell_g}\left(\frac{1}{\ell_{sc}} - \frac{1}{\ell_g}\right) \tag{1.37}$$

In Figure 1.20 shows the divergence of the diffusion solution from the RTE approximation, where l_g is plotted as a function of l_{sc} normalised by the critical radius for a spherical particle.

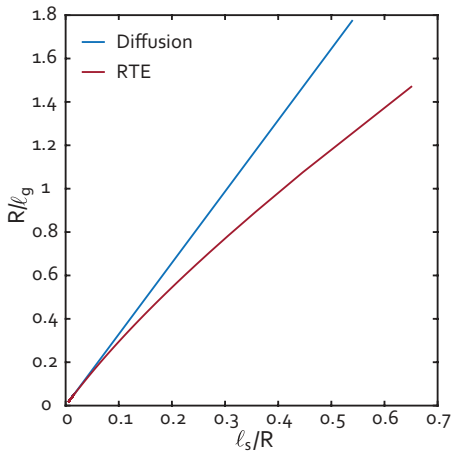

Figure 1.20: **Comparison of the thresholds computed from different models.** The blue line is the diffusive threshold computed from equation (1.31). The red line is the RTE threshold computed from equations (1.37)

1.4.4 Experimental characterisation of lasing action

Lasing experiments are performed with the setup described in Figure 1.21 unless stated otherwise. The main property of the setup is the excitation, which is a high energy density, reaching powers up to few $\mu J/mm^2$ per pulse (depending on the excitation area), required to achieve population inversion and subsequently lasing.

Individual samples, in most cases microspheres, are pumped by the second harmonic of a pulsed microchip Nd:YAG laser with excitation wavelength at 532 nm. The pulse time width reported is 500 ps with a measured average energy per pulse of $\sim$ 3.4 μJ. Due to the laser fluctuation coupled to fluctuations of the lasing process, particularly around threshold, measurements are typically single pulse. The excitation energy is controlled via an acousto-optic modulator (AOM) represented in Figure 1.21 in red. The AOM comprises of a crystal where sound waves travelling through the crystal effectively create a grating of refractive indices. The sound waves are voltage controlled (0 - 5V) and are generated by a

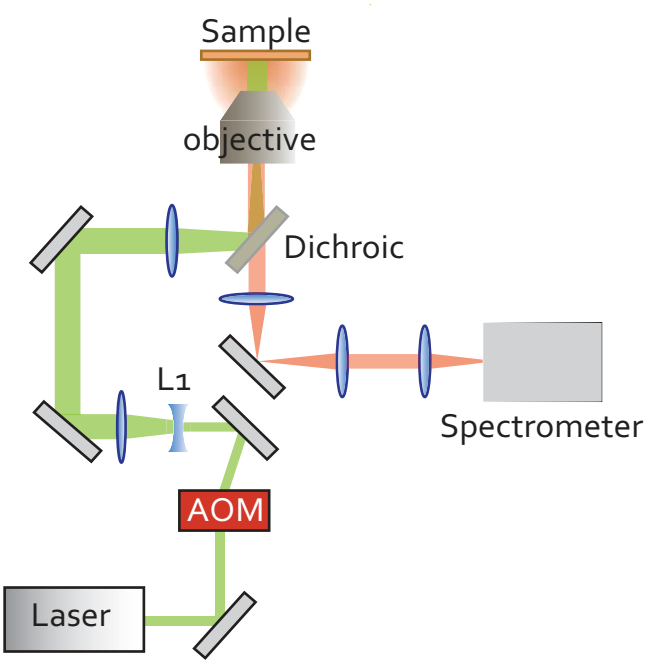

Figure 1.21: **Custom built optical setup**. Key elements of the setup are presented on the schematic. The negative lens L1 is mounted on a rail and XY stage, allowing the tuning of the spot size at the objective.

radio frequency given by the AOM driver. In practice this configurations allows us to achieve up to 3 orders of magnitude control in energy density, further improved by either changing the spot size to change the energy density, or decrease it by utilising neutral density filters. Unlike a conventional microscope configuration, where the light is focused on the sample, here the light exits the objective collimated with spot size ranging from $50\,\mu m - 170\,\mu m$ in diameter with the 40X air objective and 10X air objective respectively.

Collection takes place in reflection through the same objective used for excitation. Due to the Stokes shift of the emission with respect to the excitation, a dichroic beam splitter separates the pump from the emission. Furthermore, long-pass filters remove any residual excitation light. The emission is directed to a low noise, high resolution spectrometer. A Princeton Instruments Isoplane 320 spectrograph is employed, which supports 3 turrets containing a mirror, a high resolution grating (small wavelength span) and low-resolution grating (high wavelength span). The signal is collected on to a low noise CCD array. This system allows the distinction of narrow lasing peaks, broad emitters as well as real plane imaging and Fourier imaging. The maximum spectral resolution is 0.03 nm around 600 nm for a slit width of $10\,\mu m$.

1.5 Biocompatible optical materials

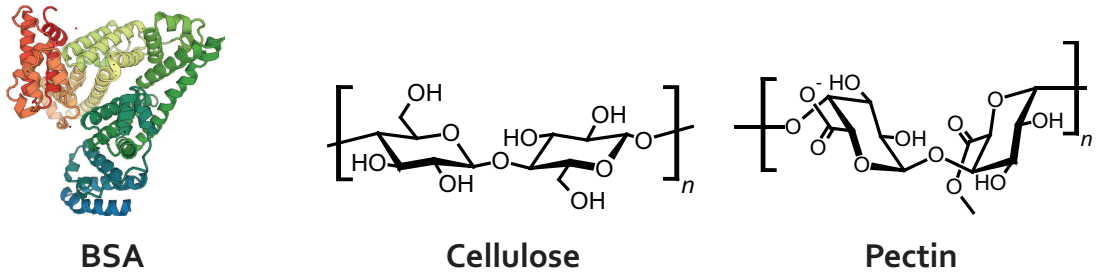

Figure 1.22: **Chemical structure of biomaterials**: BSA, Cellulose and Pectin.

Biopolymers are promising building blocks for new generation devices with a huge variety on offer. This class of polymers is produced by living organisms, from chitin in butterfly wings [101] and arthropods exoskeletons, [102] to the collagen in lens arrays or in dermal iridescences, to the keratin in bird claws, [103] among many others. Much effort is directed to re-engineering these green, readily available materials into technological platforms. [48, 104, 105, 106] Our reasoning is to exploit a few of each class with intent to identify which could pose as the best matrix for our gain molecules and the best structure overall. Our long term goal is to implant our optical devices in the human body. There are many candidates available which can potentially reside in the human body or in contact with tissue for the duration of the measurement and with low degrees of inflammatory response, we will consider there polymers to be biocompatible, however studies into the specific target areas of our optical devices have not been studied and true biocompatibility is not accessed in this thesis. We exploited two classes of biopolymers: i) proteins and ii) polysaccharides.

Proteins consist of a chain of amino acid residues, and they perform many biological functions. There are two types of proteins, globular and fibrous. Globular proteins are spherical in shape, and are mainly responsible for transport of vital nutrients. An example of such a protein in Bovine Serum albumin (BSA) which is responsible for the transport of biomolecular species such as lipids, hormones, metal cations and therapeutic drugs in the blood stream and for the osmotic pressure maintenance in blood plasma [107]. The structure is illustrated in Figure 1.22. A fibrous protein exploited was fibroin derived from silk. Silks are synthesised by a variety of organisms, silkworms, spiders, scorpions, flies and others, we use silk woven by the worm Bombyx Mori. Fibroin is a fully biocompatible

protein and has many medical applications such as silk sutures [108] and silk screws [109] for wound and bone healing [110, 111]. Silk is transparent at visible wavelengths and has exceptional mechanical properties, in fact has been used extensively in photonics: holographic gratings [18], waveguides [112] and DFB lasers [113] have been obtained. The advantage of using a protein such as silk, is that it can incorporate both organic and inorganic compounds while maintaining their functionalities ranging from enzymes, antibodies to quantum dots and dye molecules [114].

Polysaccharides instead consist of a repeating sugar units and most commonly they have structural and storage functions. We exploited three polysaccharides: cellulose, pectin and chitosan. Cellulose is one of the biomaterials we will exploit and is the most abundant biopolymer on earth. Moreover, cellulose is a biodegradable, biocompatible, and renewable natural polymer and hence it is considered an alternate to non-degradable fossil fuel-based polymers. Cellulose is most commonly found in lignocellulosic materials in forest, where wood pulp, illustrated in Figure 1.23a, is currently the most prevalent source [115]. However, a rich source of living organisms can synthesize cellulose, including Tunicates [116], certain bacteria such as *Komagataeibacter xylinus*, [117] and algae [118]. Naturally cellulose is synthesised in individual molecules, illustrated in Figure 1.23d, and individual cellulose molecules are assembled into elementary fibrils. Packed together the fibrils make up microfibrils, which in turn assemble in to cellulose fibres, such as the ones depicted in Figure 1.23b.

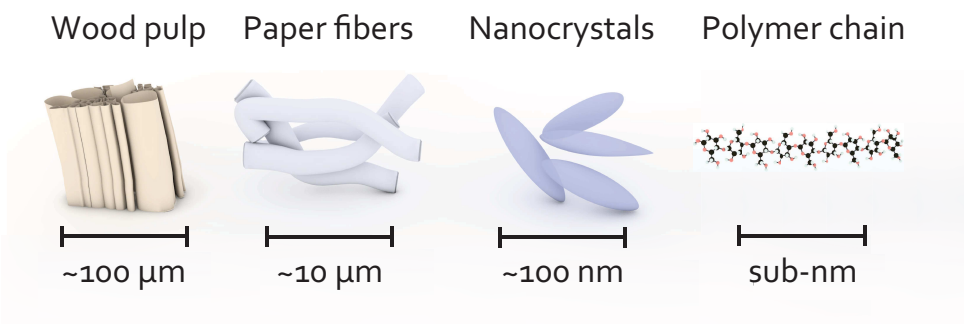

Figure 1.23: **Cellulose from wood pulp to polymer chains**. Size comparison between the different forms that cellulose can adopt, from the wood pulp to molecular cellulose.

Fibrils are composed of crystalline portions, where the atoms are in structural order,

and amorphous sections. The crystalline elements can be isolated via acid hydrolysis. They are called cellulose nanocrystals (CNCs) illustrated in Figure 1.23c, can be extracted and suspended in water [119]. Chitosan is the most abundant derivative of Chitin, obtained by the deacetylation of chitin in alkaline conditions. Chitin is the supporting material of crustaceans and insects, like cellulose it is a structural polysaccharide [120]. Chitosan has excellent properties such as biocompatibility, biodegradability and non-toxicity. [121] Chitosan has antibacterial properties [122] and has been developed commercially for the healing and treatment of wounds [123, 124, 125]. Pectin instead, is contained in the plant cell walls of plants and is a gelling agent used in jams. Pectin is an important cell wall polysaccharide that allows primary cell wall extension and plant growth.

All of the biomaterials mentioned are readily available and sourced naturally, they can be solution processed and yield solid and transparent films. Therefore, they are good candidates for optical devices and lasers.

1.6 Outline of the thesis

- Chapter 2 exploits a co-deposition technique to obtain nanostructured biocompatible materials, specifically cellulose nanocrystals. The light transport properties of structured materials are studied in this chapter and compared to that of conventional paper.
- Chapter 3 shows a technique to obtain solid state microsphere laser of various materials. In this chapter lasing emission from the micropsheres is obtained and characterised. Additionally the microspheres are studied in biological media and cultured with cells.
- In chapter 4 a biocompatible silk random laser is obtained. Lasing emission from silk is achieved and characterised. The fabrication method is applied to other materials and the random laser is made smaller. The size and threshold dependence of the random lasers is studied. Lastly foams with gain are studied and characterised.
- Finally in chapter 5 sensing with silk random laser is shown, the sensing mechanism is explained and the response is theoretically predicted.

2 Nanostructured Biomaterials for Scattering

Cellulose fibres, such as the one extracted from cotton or wood-pulp, have been used by humankind for hundreds of years to make textiles and paper. Cellulose is the most abundant biopolymer on Earth, an almost inexhaustible material and a source of a range of sustainable derivatives, such as cellulose nanocrystals.

Here we show how, by engineering light—matter interaction, we can optimise light scattering using exclusively cellulose nanocrystals. The produced material is sustainable, biocompatible, and when compared to ordinary microfibre-based paper, it shows enhanced scattering strength (×4), yielding a transport mean free path as low as 3.5 μm in the visible light range. The experimental transport studies are in a good agreement with the theoretical predictions obtained with a diffusive model for light propagation. Furthermore we predict theoretically the conditions for maximal scattering. I envisage an increase in contrast for paper based sensors as well as specialised functionalisation not possible for non-crystalline cellulose; opening doors for sensor improvement and development.

2.1 Introduction

Maximal scattering gives rise to a smaller transport mean free path (ℓ_t) and more opacity for a given L. In the context of random lasers this is equates to a smaller random laser for a fixed gain length (ℓ_g). Miniaturisation is essential for integration into cells and living tissue. In this chapter we explore the structuring of cellulose in the absence of gain into an inverse photonic glass paper and theoretically explore the optimum void size for increased scattering.

With the term "paper" we include a large variety of cellulose-based composite materials that find use in everyday life such as in packaging and printing. Recently, paper-based technologies have captivated increasing interest not only due to their applications in sensing [126, 127, 128] and lasing [84], but also in 3D-cell scaffolding [129]. Cellulose can be easily functionalised to produce materials with enhanced mechanical, optical, and chemical properties due to its intrinsic fibrillary morphology and consequent porosity. These new materials are particularly attractive from an industrial point of view thanks to their low production costs [130]. The main components of paper are cellulose fibres [131]. Natural cellulose can be extracted from different sources: ranging from plants (such as wood pulp or cotton) to bacteria, to invertebrates and some marine animals [119], nonetheless it is consistently found to have fibrillar nature [132]. In paper-manufacturing process, moist cellulose fibres extracted from natural sources are compressed together and dried. Printing paper is opaque and white, where the thicknesses of the fibres and their packing density determines the optical properties of the material and consequently its appearance [131]. Conventional fibres in paper are several tens of microns in diameter, and therefore, they are not ideal to produce a strong scattering response. Visible light is more effectively scattered in the condition where the particles are of the order of the wavelength (λ) rather than nanometer scale. To achieve this we use a smaller component of cellulose, cellulose nanocrystals depicted in Figure 2.1, typically of the order of 100 nm in length and a few nm in diameter. Due to their rigid nature, high aspect ratio and stiffness, highly porous networks have only recently demonstrated in the form of foams [133, 134, 135] by freeze drying (technique covered in section 4.4.1).

Here we show the first inverse photonic glass made soley of CNCs which enhanced the scattering strength of the material. We aim to reduce packaging costs, eliminate the need

for special coatings and bleaching as well as increase contrast in sensors, whist maintaining the robustness and controllable surface chemistry [119, 136, 137].

2.2 Fabrication

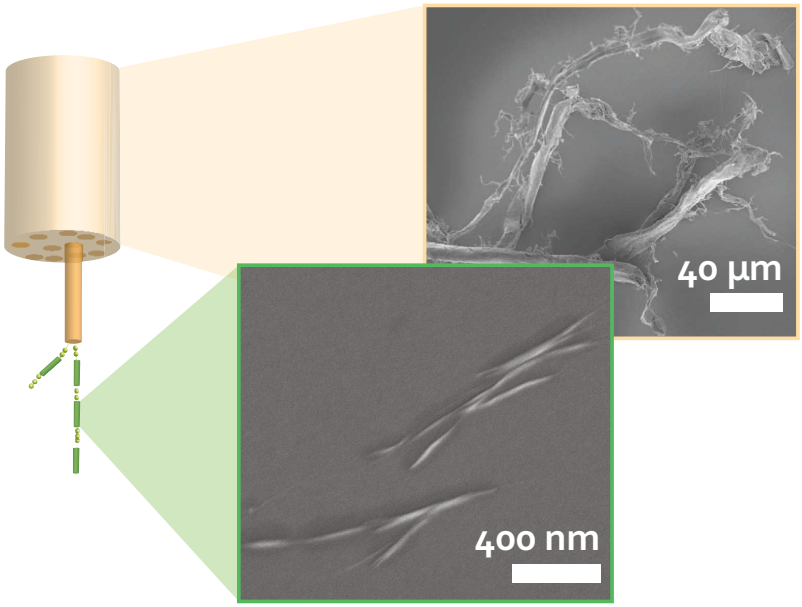

Figure 2.1: **Diagram of the structure of a cellulose fibre.** Cellulose fibre is composed of fibrils (orange cylinder) with alternating crystalline (dark green rods) and amorphous (light green spheres) sections. On the top, cellulose fibres used to fabricate white paper is shown on the top SEM image. The bottom SEM image shows the isolated crystalline portion of the cellulose fibril, cellulose nanocrystals.

Bulk cellulose, as many other natural polymers, is transparent to visible wavelengths of light [138], in the absence of absorption and dispersion the transport properties are dictated by the shape of the interfaces. By creating a disordered structure of cellulose in air it can become opaque. Nature cellulose does not occur as an isolated individual polymer chain element, instead they can be found as fibrous units. An individual cellulose fibre, illustrated in Figure 2.1 in beige and in the scanning electron microscope (SEM) image on the right, is composed of fibrils, represented in orange in Figure 2.1. Subsequently fibrils are made up of alternating crystalline and amorphous sections, dark green rods and light green spheres respectively. The ordered regions, called cellulose nanocrystals (CNCs), result from a tight packing of cellulose chains. Individual CNCs have needle/whisker like geometries evidence in the bottom SEM in Figure2.1. Due to their appealing properties,

such as nanoscale dimensions, high surface area and mechanical strength, amongst others, CNCs are a promising material for reinforcing agents in nanocomposites [139] and our material of choice to construct cellulose paper with improved light-matter interaction.

2.2.1 Extracting CNCs from cellulose

The CNCs used throughout the thesis are commercially available from Forest Product Laboratory Canada in powder form. These specific CNCs are extracted from wood-pulp via a sulphuric acid treatment, leaving negative charged sulfate half-esters which are neutralised with Na^+ ions. The dimension of these crystals are around 5 nm in diameter and ranges from 150 to 200 nm in length, but this can very according to the fabrication technique used. The pH of the suspension is neutral, whereas the surface change is 278 ± 1 mmol/kg estimated by conductometric titration [140].

2.2.2 Inverse photonic glass

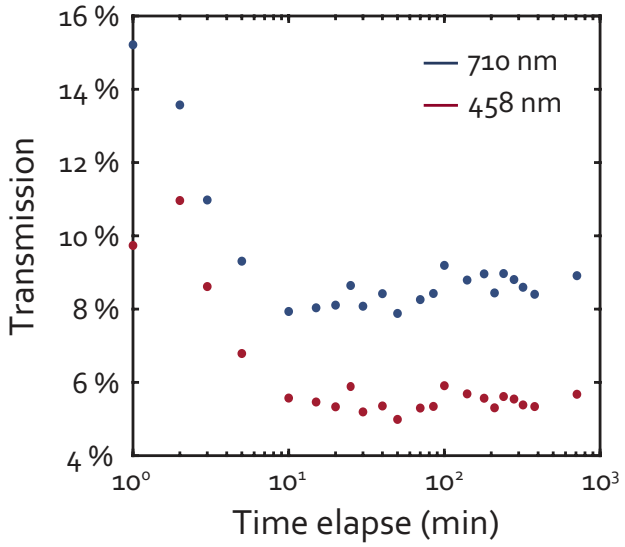

Figure 2.2: **Transmission through an inverse photonic glass made of CNCs immersed in toluene**. Initially the beads and the cellulose are close to index matched, the transmission decreases as the toluene dissolves the polystyrene beads and leaves an increasing void of solution of lower refractive index. Once most of the PS is dissolved the transmission flattens out.

Photonic glasses can be used as a template to implement disorder in a film of CNCs, similar to fabrication procedures for inverse opals [47, 48]. Conventional methods are conducted with the infiltration of the photonic glass with the polymer used. However, we find that a

co-deposition of PS beads and CNCs in solution is successful and simpler. Given the size of the individual CNCs with length up to 200 nm, infiltration would be difficult to achieve. Lack of compactness of the CNCs would yield a brittle sample, as the hydrogen bonds between CNCs would be weaker. At high filling fraction of the PS beads the gaps between the spheres can be as small as tens of nm comparable to the CNCs building blocks used.

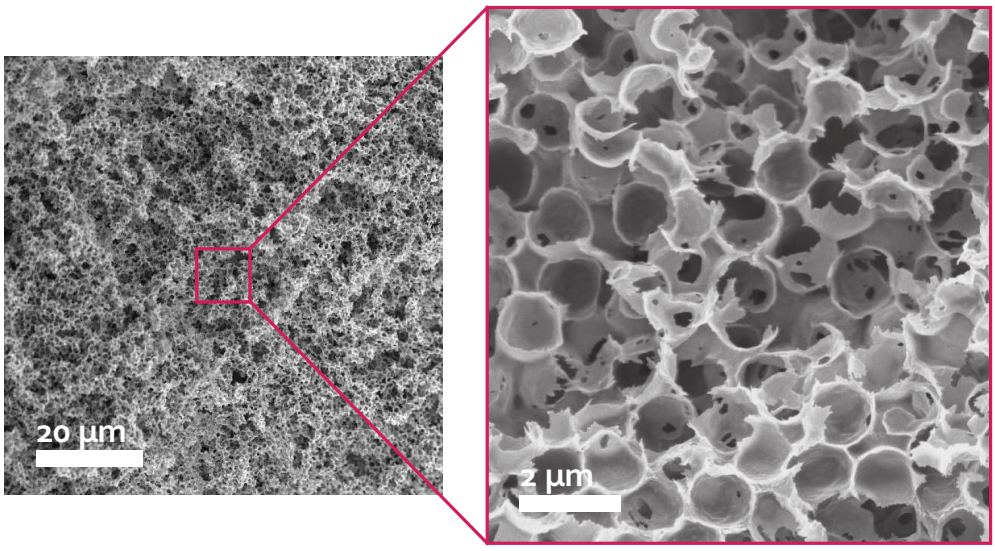

Figure 2.3: **Cellulose inverse photonic glass morphology**. SEM images of cellulose inverse photonic glass. On the left a large field of view highlights the randomness of the packing and homogeneity of the sample. On the right a close up of the sample which shows the interconnected voids.

A cellulose inverse photonic glass is fabricated using a templating technique that consists in the co-deposition of monodisperse PS spheres and CNCs and subsequent chemical etching of the PS spheres. Powdered CNCs are dissolved in deionised water using ultrasonication at room temperature to yield a 4 %wt CNC aqueous solution. The solution is mixed with colloidal monodisperse polystyrene (PS) spheres of diameter $d = 1.27\,\mu m$ (Micro particles GmbH), such that the dry weight ratio between CNCs and PS spheres is 2:3 respectively. This ensures a close and homogeneous packed system. The obtained suspension is then cast into a hollow Teflon cylinder attached to a glass substrate with PS. Prior to this, the Teflon cylinder is immersed in a NaOH bath to improve the hydrophilicity of its surfaces, while the glass is coated with PS to stabilize the film (to avoid cracking during drying). The samples are kept in partially sealed containers and dried for 1-2 weeks in a quasi-saturated water vapour atmosphere kept at a constant temperature (30^oC). Such

conditions allow a slow evaporation rate of the water in solution, this further improved the film quality by avoiding cracking and de-lamination.

Once the sample is dry, the PS spheres are selectively etched in a bath of toluene for approximately 3-9 hours, depending on the sample thickness ($50-500\,\mu m$). Toluene also removes the PS coating from the glass substrate and separates the Teflon cylinder from the glass; this facilitates the detachment of the sample, yielding a free-standing cellulose inverse photonic glass, a nanostructured paper. The CNCs properties are unaffected by the toluene bath [141, 142], as confirmed by the transmission experiments conducted for a time span of over hours 10h, illustrated in Figure 2.2. No significant change in transmission through the sample immersed in toluene is observed after the initial etching, over all visible wavelengths. In the eventuality of damage to the cellulose, the scattering is expected to decrease resulting in an increase in transmission, which is not observed in the etching timescales.

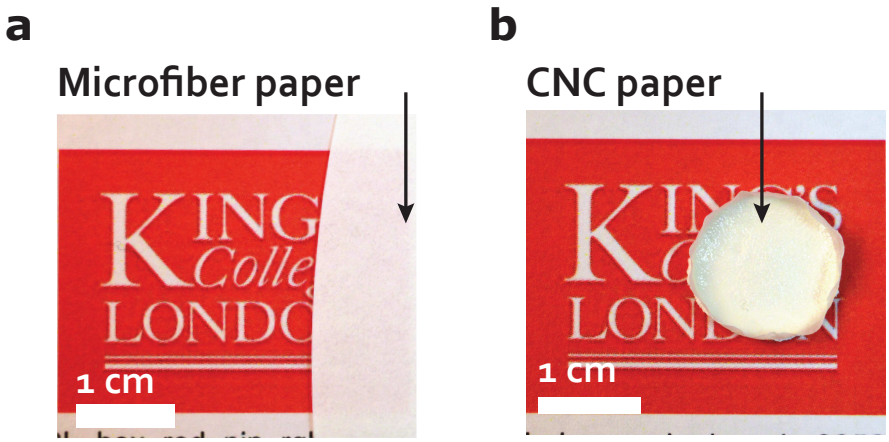

Figure 2.4: **Comparison of the opaqueness of conventional filter paper with CNC paper.** A microfiber paper 180 μm thickness is more translucid than a CNC inverse photonic glass 100 μm thick.

After the drying process and etching, a cellulose inverse photonic glass is obtained, the sample is placed in a fumehood overnight to ensure complete evaporation of toluene before it is used for any experiments. SEM inspection reveals a random close-pack arrangement of air voids in an CNC matrix, shown in Figure 2.3 made evident by the interconnected voids of around 1.3 μm in diameter. Throughout the thesis samples imaged by SEM are uncoated, unless stated otherwise. Optically there is lack of iridescence and enhanced normal reflection made evident by Figure 2.4b.

The only observable change in the sample's appearance is a minor reflection from the

surface in contact with the glass i.e. where the cellulose layer is more compact. This geometry is particularly convenient to optimise light-matter interaction because it provides the right to balance between the size of the scattering elements (at the edge of the spherical voids), and a high filling fraction. In addition, a photograph of one of the samples fabricated is shown in Figure 2.4b (approximately 1.5cm in diameter and 100μm thick): the increased opaqueness of the photonic glass paper is visible even by the naked eye, when compared to conventional paper of similar thickness in in Figure 2.4a.

A close up of the a broken section of the sample is sputter coated with Au-Pd in illustrated in Figure 2.5. The figure reveals the packing of CNCs within the inverse photonic glass. Au-Pd prevents charging and allows high magnification imaging. The needle like geometry of the CNCs is apparent, furthermore they tend to align surrounding where the polymer spheres once were, analogous to the alignment of matches in a box which tend to align parallel to each other when shaken. We hypothesise that the interaction between the CNCs at high concentrations given the repulsion between CNCs is outweighed by the charges of the polymer spheres deterring the transition to an aligned nematic phase as observed with pure CNC films [143, 144, 145].

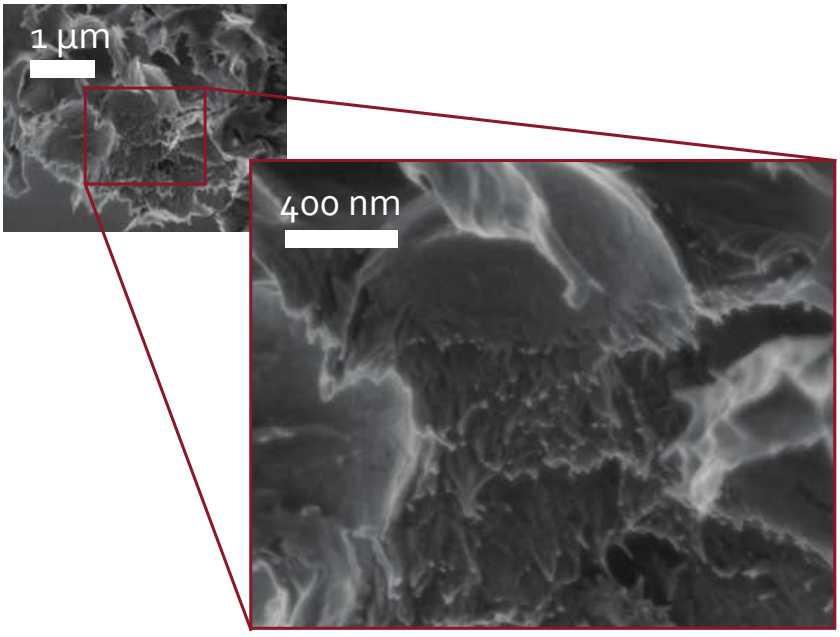

Figure 2.5: **High magnification SEM image of the cellulose photonic glass.** The whisker like geometry of the CNCs which arrange in close-packing is visible. The sample was sputter coated with a few nm of Au/Pd to prevent charging.

2.3 Measuring scattering

The transport mean free path ℓ_t is a measure of the scattering within a diffusive media, simultaneously it gives us an estimate of the minimum dimensions required for complete scrambling of the light propagation and consequently the opaqueness of the media. In the subsequent sections we will measure ℓ_t for both conventional filter paper and for the inverse photonic glass paper obtained. Experiments will use an integrating sphere, method described in the introduction.

2.3.1 Transport mean free path of paper

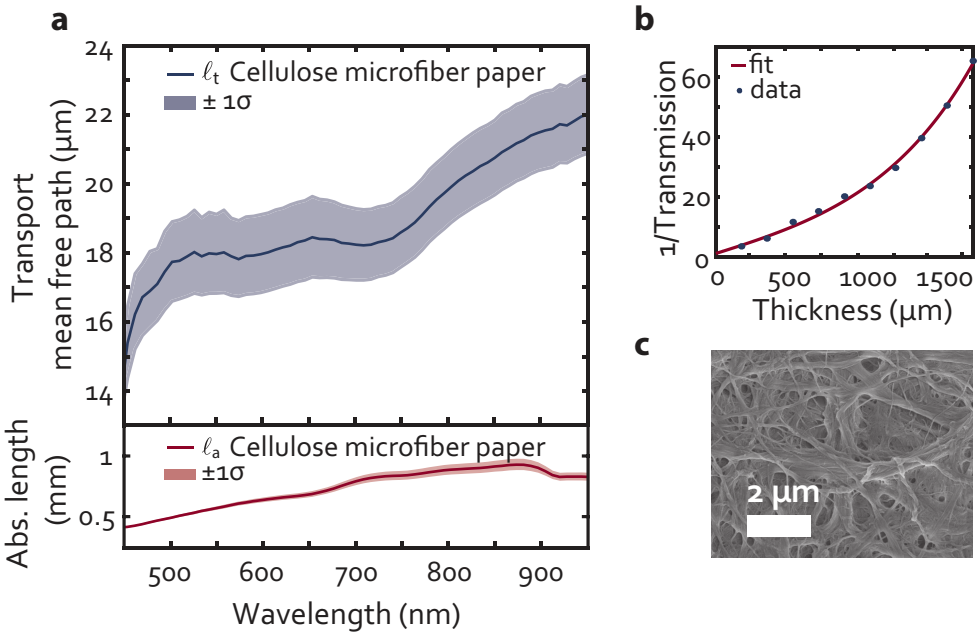

Figure 2.6: **Transport mean free path of paper.** a) Experimental results obtained from 1-10 stacked sheets of filter paper b) Example of the fit for $\lambda = 600\,nm$. In red the fitted curve and in blue circles the effective thickness. c) an SEM of the surface of the filter paper, depicting the disordered interwoven cellulose fibres.

The ℓ_t of conventional paper is typically of the order of $\sim 20\,\mu m$ measured in reference: [12]. Here we characterise Whatman® filter paper, Grade 1 with a reported thickness of $180\,\mu m$ confirmed by SEM inspection. To measure transmission for different paper thickness, multiple sheets of paper were compressed together increasing the effective thickness. The transmission spectra of cellulose fibre paper, averaged over 10 measurements, was fitted with equation 1.10 for each wavelength, an example fit at $\lambda = 600\,nm$ is shown in Figure 2.6b. Each blue circle in is the transmission of n layers of filter paper at $\lambda = 600\,nm$.

For increasing thickness the effect of absorption induces an exponential dependence of the inverse transmission T^{-1} on the slab thickness L, i.e.: $T \alpha e^{-\ell_a L}$ in contrast to a linear dependence of $T \alpha L^{-1}$ in absence of absorption. The exponential dependence follows the Lambert-beer law in equation 1.8. In dark red is the result of the fit of equation 1.10 with two free parameters: ℓ_t and ℓ_a.

We have used a multi-step fitting routine:

1. $\ell_t(\lambda)$ and $\ell_a(\lambda)$ were taken to be free parameters of the fit. Approximate value of both for each wavelength were obtained;

2. We fix one of the parameters, for example $\ell_a(\lambda)$, and allow the other, for example $\ell_t(\lambda)$ to be the free parameter of the fit. This is done interchangeably until convergence is achieved (after 4 iterations);

Additionally, to avoid the effect of stochastic noise and improve the convergence, the fitted value from each wavelength was used the previous fitted value for $\lambda_i(z_0)$ as the starting point of the next fit $\lambda_{i+1}(z_0)$. The measured ℓ_t ranges between 15 and 22 μm in the visible spectra as depicted in Figure 2.6a, while ℓ_a is of the order of a millimetre. The measured ℓ_t is an underestimation of the actual value. There are two competing effects: the air gaps between the sheets and the reflection at the interface of each sheet. The air gaps between the sheets are expected to increase the apparent ℓ_t, as the presence of the air gaps increases the effective sample thickness, however the air gaps are estimated to be less than 10% of the sample thickness. The reflection at each interface (about 40% for each sheet), has a more pronounced effect on ℓ_t. It increases the total reflectivity thus lowering the transmission and the measured ℓ_t. The error bars of the fit are represented by the shaded regions in the plots.

2.3.2 CNC inverse photonic glass

The measurement of ℓ_t in the case of the photonic glass paper was performed by comparing six samples with different thicknesses in the range 100–400 μm. The thicknesses are estimated by SEM inspection averaged over different points on the sample, to account for possible variability of the thickness within the sample. An error of the mean was found to be around 5%. The transmission spectra of the cellulose photonic glass was also averaged

over different regions of the sample and a dispersion less than 5% is measured. Using the same procedure depicted above, the data was fitted with Equation 1.13. As $\ell_a \gg L$, lossless Ohm's law is valid, as shown in Figure 2.7b a typical fit at $\lambda = 600\,nm$, where the sample transmission dependence on the slab thickness is linear, unlike for fibre paper. Therefore, for simplicity and stability of the fit, we have chosen $\alpha = 0$.

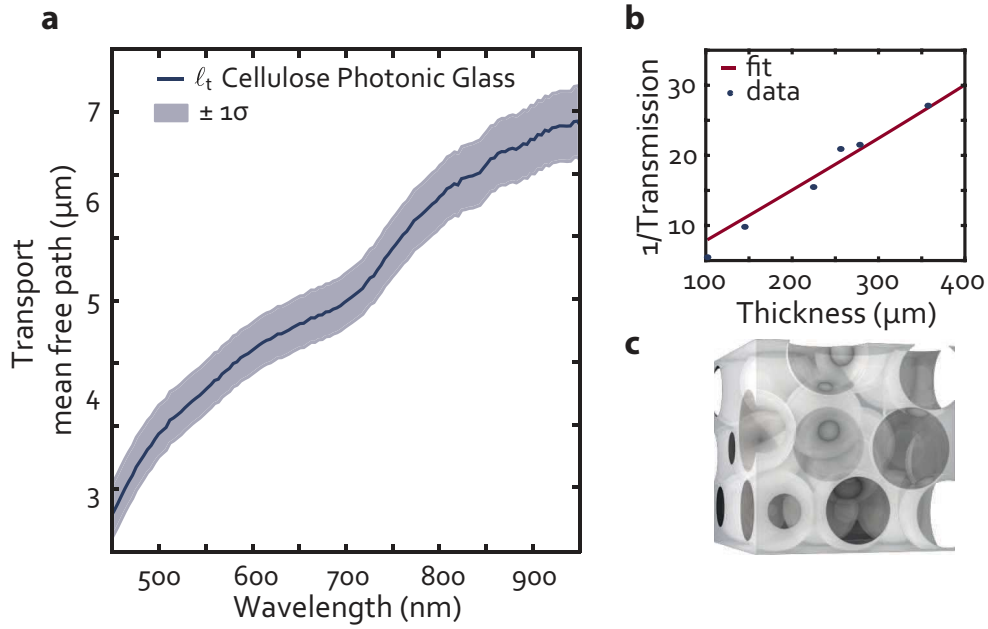

Figure 2.7: Transport mean free path of CNC inverse photonic glass. a) Experimental results obtained from 6 inverse photonic glasses of different thickness. b) Example of the fit for $\lambda = 600\,nm$. In red the fitted curve and in blue circles the samples each of a single thickness. c) a diagram of the structure measured.

Figure 2.7a shows the result of the fitting routine, ℓ_t obtained as a function of wavelength. The statistical error of the fit is accredited to minor sample-to-sample variation and is estimated to be less than 10%. The measured ℓ_t is in the range $\ell_t \approx 3-7\,\mu m$ for the visible range of light, with very shallow resonances. The lack of resonances is expected, as air voids in a higher refractive index matrix are poor resonators, in contrast with high refractive index spheres which show appreciably stronger resonances [16].

The ℓ_t dependence on wavelength is corroborated by Mie theory, where confinement increases towards shorter wavelengths, shown in Figure 2.8. The theoretical calculations plotted are performed via Mie theory and independent scattering approximation of a sphere of air in a cellulose matrix for $d = 1.27\,\mu m$. Comparing to previous works [43] we expect

the photonic glass paper to have a filling fraction around f = 50-55%, smaller than the theoretical limit for hard-sphere random packing [10]. We take into account polydispersity of 0%, 2% and 25% [2, 4], where 2% corresponds to the realistic polydispersity of the PS spheres used and 25% corresponds to the effect of using a cheaper building block, polydisperse spheres. Since the resonances are weak, they are unaffected by the small polydispersity. For a 25% polydispersity we observe a complete flattening out of the already weak resonances. In the condition where the average sphere size is $d = 1.27\,\mu m$ we do not expect a large change in the overall scattering of the device.

By characterising the scattering response of the CNC-based photonic glass we obtain a scattering more than 400% stronger than for standard cellulose fibre paper. The experimental results compare well with a diffusive model, as seen in Figure 2.8.

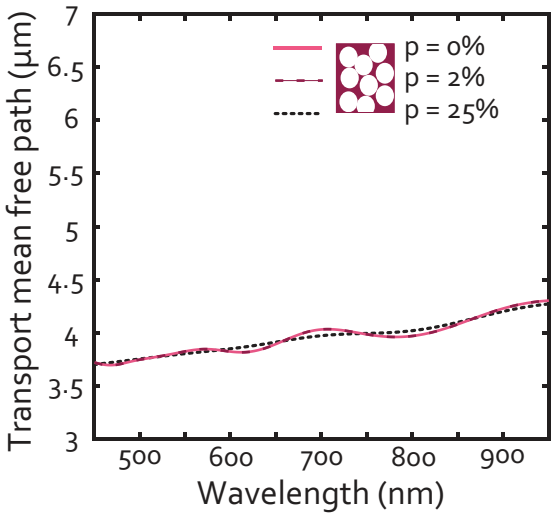

Figure 2.8: **Modelling experimental transport results for an inverse photonic glass.** Theoretical transport mean free path calculated for air spheres in cellulose matrix $n_{cellulose} = 1.55$ at with filling fraction of $f = 0.55$ as a function of wavelength (full red line) assuming polydispersity of 2% (dashed red line) and assuming a polydispersity of 25% (dashed black line).

2.4 Enhancing light scattering

We investigate the optimum void diameter for maximal scattering using the model described in the introduction. Figure 2.9 plots ℓ_t for different void diameters (at $\lambda = 600nm$), both in the absence of polydispersity, at 2% polydispersity and with 25% polydispersity. At small sphere size an abrupt increase of ℓ_t is observed. The polymer microspheres are

less than half of the wavelength and therefore the scattering is much weaker, dictated by Rayleigh scattering. At $d = 250\,nm$, ℓ_t is at its lowest value, around $\ell_t \sim 1.3\,\mu m$. For increasing diameter ℓ_t increases. PS spheres are cheaper and easier to produce than its monodisperse counterpart, therefore we explore here the effect of polydispersity in the templating matrix. Our calculations show that even for large polydispersity, as high as 25%, the average value of ℓ_t is unaffected, only the resonances are damped, as shown by the dotted black line in figure 2.8 and 2.9. This of course requires the average size of the spheres to be $d = 1.27\,\mu m$.

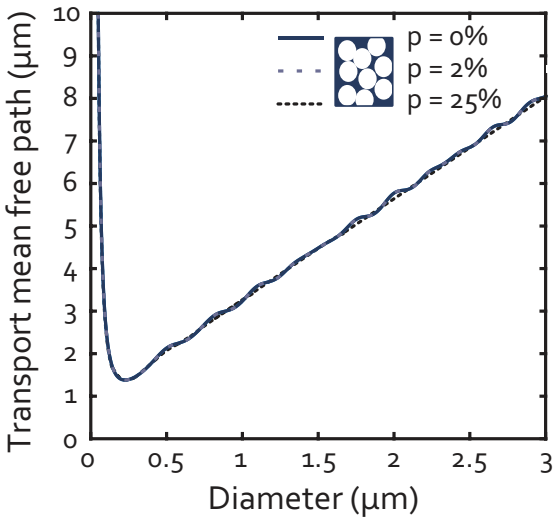

Figure 2.9: **Theoretical scattering strength with different void diameter.** Theoretical transport mean free path calculated for air spheres in cellulose matrix $n_{cellulose} = 1.55$ and with a filling fraction of $f = 0.55$, as a function of different void diameters at $\lambda = 600\,nm$.

Although scattering may be increased by using smaller PS sphere to nanostructure the CNCs, smaller CNCs than the ones used here are required to ensure maximal close-packing of the sphere.

2.5 Outlook/Conclusion

Here we presented a highly scattering nanostructured CNCs paper with $\ell_t \approx 3 - 7\,\mu m$. The inverse photonic glass made of CNC scatters 4 times more than standard cellulose fibre paper. By post-treatment of the film, or by adding other materials in suspension, the properties of the produced photonic glass can be further improved in terms of mechani-

cal properties and moisture resistance [146, 147, 148, 149]. Increased scattering implies that the same visual contrast and whiteness can be achieved in a thinner sample. With a simple theoretical model, we identify the optimum sphere diameter of about half the light wavelength, for which the scattering strength can be maximized. Large scattering strength allows for larger contrast in sensors, thinner paper, which would reduce coating and packaging. Furthermore, nanophotonic enhanced paper offers the additional benefit of large porosity together with increased light—matter interaction. This work builds towards improving scattering in polymeric systems which can host dyes and lead to low threshold random lasers.

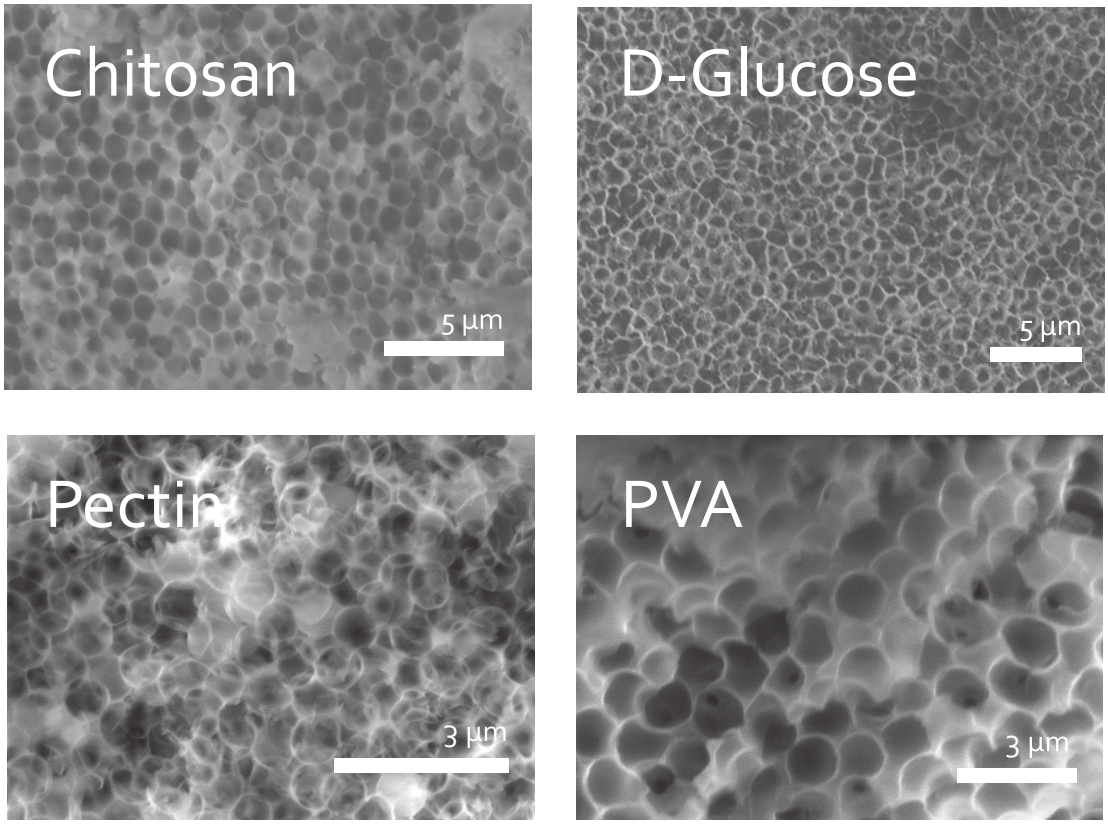

Figure 2.10: **Inverse photonic glass of different biomaterials.** Scanning electron images of nanostructured Chitosan, D-Glucose, Pectin and PVA.

Future work on this material will require the fabrication of CNC inverse photonic glasses using different PS sphere sizes to nanostructure the CNCs and obtain maximal scattering given the large size of the CNCs. Chemical functionalisation of the CNCs is required to make the paper more water resistant and more or less flexible considering the possible applications.

This chapter presents a method to add and increase scattering to a transparent poly-

mer with the intent of creating a platform for multiple scattering for random lasing. The nanostructuring is not limited to CNCs and has been accomplished to date with many other materials such as: Pectin, D-Glucose, chitosan, PVA, BSA, silk and silica. The prerequisite for this fabrication method is that the biomaterial be water soluble and once dry be resistant to the etching solvent, toluene. For example, cellulose in its molecular form was used as a building block, and we found that selective etching of the spheres was not possible, as molecular cellulose would dissolve at similar rates to the PS beads.

The inverse photonic glass structure of Pectin, D-Glucose, chitosan and PVA is depicted in Figure 2.10, the other mentioned materials will be discussed in chapter 4.

3 Whispering gallery mode microsphere lasers

Biolasers obtained from biomaterials are attracting a wealth of interest for their potential as future biosensors with enhanced sensitivity and advanced cell tracking. Here, miniature biolasers are reported, which are formed by bovine serum albumin (BSA) protein and biosourced polysaccharides derived from land plants such as cellulose and pectin. Using a green processing route aided by simple emulsions, solid-state microspheres with diameters of 5–300 μm are fabricated and utilised as whispering gallery mode lasers with thresholds of a few $\mu J/mm^2$ and quality (Q) factors of up to 3000. Furthermore, BSA microlasers are found to be compatible with cell growth and resistant to the aqueous environment of cell culture media. This environmentally friendly and biocompatible design shows promise for future implantable biosensing devices opening a path between laser science and medicine.

3.1 Introduction

Lasing in biocompatible materials has taken on many conventional lasing geometries. The simplest form is the living cell laser where the gain, mutant Green fluorescent protein (eGFP), was expressed by a living cell which was placed into a conventional high-Q microcavity. Other geometries have been used such as, distributed feedback gratings [113, 150, 151]; optofluidic lasers [152, 153]; microspheres [75]; microdisks [154] and in random lasing in human tissue [86, 87, 155] as well as in other biomaterials [85]. Specifically, whispering galley mode (WGM) microsphere lasers have grown in significance to the biosensing community since their integration into living cells [8, 78]. The microspheres were employed as intracellular sensors, and cell tagging and tracking agents. The addition of sodium chloride caused a wavelength shift by a change in refractive index of the cell's interior. Furthermore, the spectrum fluctuations spanning from the distortion of the cavity are a measure of the internal stress of a cell [8]. Due to their intrinsically high quality factor and small mode volume, [156] there lies a great potential for the development of low threshold microlasers and sensors [70, 72, 157].

In this chapter we will focus on the fabrication and characterisation of solid state WGM microspheres. High Q-factor WGM lasers are made with versatile and simple fabrication techniques. We will show that the technique is applicable to a variety of materials and micron sizes ($5-300\,\mu m$) and uses inexpensive tools.

3.2 Fabrication of WGM lasers

Microspheres lasers made of biologically produced materials are of interest for implantable biosensors as they are expected to offer excellent biocompatibility in medical applications [85]. Here I will first address different classes of materials for biocompatible WGM lasers addressing a simple multi-material fabrication technique, which yields high lasing quality factors.

There are an abundant number of biomaterials which meet our immediate requirements to constitute a spherical dielectric cavity capable of sustaining lasing. A few predicaments are transparency, biocompatibility, stability during measurement but degradability over time in biological media and facile fabrication. We chose a protein, Bovine serum albu-

min (BSA), and two readily available polysaccharides, cellulose and pectin, all of which are biocompatible and biodegradable materials. Their chemical structure can be found in the first chapter in Figure 1.22. Specifically, these polysaccharides have recently picked up considerable attention for the elaboration of a wide range of biomaterials and biocompatible devices [158, 159, 160, 145] .

Here, we demonstrate a novel method for fabricating solid microresonators using biomaterial aqueous solutions.

3.2.1 Self-emulsifying microsphere formation

A substantial effort has been directed at minimising the laser size and developing fabrication techniques which use all-biocompatible materials. Liquid droplets, formed by surface tension where first used an optical resonantor in 1977 [161]. Lasing was observed later in fluid microdroplets with observed in organic dyes [162, 163, 164, 165, 80], quantum dots [166] and nematic crystals [7, 167] and was recently acheived in a biocompatible setting with cavities smaller than 40 μm [75]. Instead, solid-state all-biomaterial lasers have so far been limited to millimetre-scale size, which is too large for practical integration with living tissues and cells [78]. Here we will address a novel simple, yet versatile, technique to produce miniature solid-state biolasers.

The fabrication of solid dye-doped biopolymer microspheres was developed in our group by Duong Ta and myself. It is schematically shown in Figure 3.1. The biopolymers are dissolved in deionised water with a lasing dye, rhodamine B (RhB) or sodium fluorescein. The doped biopolymer solutions are aspirated into a micropipette which is then immersed in a clean glass recipient containing uncured Polydimethylsiloxane (PDMS) resin (Base of Sylgard 184 Silicon Elastomer, Dow Corning). PDMS is a very viscous material; it is an inert, non-toxic, hydrophobic silicon-based organic polymer and immiscible with water based solutions. PDMS sees applications ranging from contact lenses to medical devices [168, 169]. By emulsion processing similar to previous work [77], the doped polymer solution is dispersed in uncured PDMS. An emulsion implies the mixture of two or more immiscible liquids, like water and oil, whereby if the solution is stabilised, it results in the formation of droplets. Other examples of emulsions are milk and mayonnaise, which gain their white colour from multiple scattering of suspended particles. They tend to need emulsifiers, a stabilising agent, such as a surfactant. In this procedure, surfactants are

not necessary and the spheres are formed by a process called spontaneous emulsion. The micropipette is dragged and a fibre like structure is drawn within the PDMS, illustrated in Figure 3.1a. Water is a polar molecule with a partial positive and partial negative charge which leads to high cohesive forces between its molecules in liquid state. It is responsible for surface tension; the tendency of the surface to resist rupture [170], which is the reason that insects such as the water strider have the ability to stay afloat on the surface of the water.

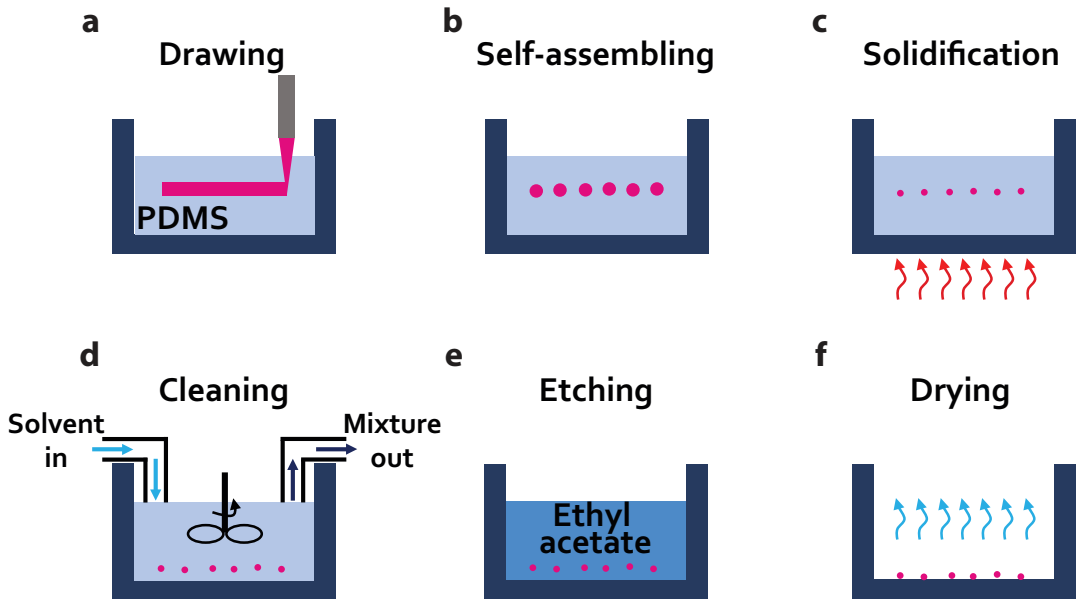

Figure 3.1: **Schematic diagram shows fabrication process of biomaterial microspheres.** a) A sharp tip containing doped polymer solution is immersed and subsequently dragged in PDMS solution b) The fibre spontaneously splits into microspheres of solution c) The PDMS is heated and the water evaporates, solidifying the spheres d) The PDMS is removed by washing the spheres in ethyl acetate e) The spheres are submerged in ethyl acetate to remove the PDMS entirely f) The ethyl acetate is allowed to evaporate, leaving polymer microspheres.

The fibre breaks into smaller portions in order to minimise the surface area, seen in Figure 3.1b. After less than a minute the droplets become spherical, an emulsion. The size of the spheres can be reduced further by mechanically disrupting the aqueous biopolymer-rich domains using a sharp needle, allowing for a wide range of sphere size, as illustrated in Figure 3.2. Once the emulsion process stabilises, the droplets are stagnant over the duration of the experiment and hover in the PDMS solution where no creaming or flocculation is observed.

The droplets were subsequently annealed on a hot plate at 100^{o}C to induce dehydration and subsequent solidification of the droplets; this is facilitated by the permeability of PDMS to water vapour, which is accelerated at high temperature [169]. The annealing time was tuned for each material and was found to be 10, 60, 90 min for complete solidification for BSA, pectin, cellulose spheres respectively. The times were kept to a minimum to avoid damaging the doping agents.

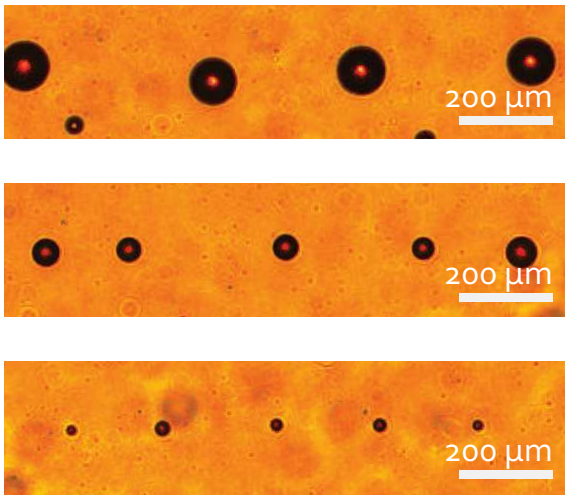

Figure 3.2: **Liquid doped biomaterial droplets in PDMS.** Sizes range from 100 μm (top figure) to 30 μm in diameter (bottom figure).

Finally, the obtained microspheres were separated from PDMS by washing in a relatively green solvent: ethyl acetate. The spheres were irrigated in ethyl acetate several times until the PDMS was visibly removed, subsequently they were left in ethyl acetate with manual agitation to ensure the PDMS was completely removed, as illustrated in Figure 3.1d and 3.1e. As PDMS base resin is well dissolved in ethyl acetate [169] the solid spheres can be easily separated from the liquid phase. Ethyl acetate has a relatively high vapour pressure at ambient temperature; as a result, the evaporation of the remaining solvent was left to proceed at room temperature for several hours in a fume hood prior to characterisation. It is important to note that the PDMS not only helps to produce liquid droplets, but also allows the formation of solid spheres. Generally, water droplets can be made using common oils, but in that case it is very hard to evaporate the water and solidify the droplets to obtain solid spheres; in contrast PDMS is water vapour permeable. The fabrication technique is flexible and a variety of microspheres of different sizes can be produced by changing the droplet

volume and density. To illustrate the flexibility of the fabrication, Figure 3.3c plots the size distribution of 80 BSA spheres. The broad cavity size dispersion from 10 to 120 μm is a result of the manual fabrication process. To extend the size variability of the process, the concentrations of biopolymer in the solution can be increased or decreased beyond what is reported. The resulting BSA microresonators are shown in Figures 3.3b and 3.3c illustrating optical and scanning electron microscope (SEM) images of dye doped BSA microspheres with different sizes.

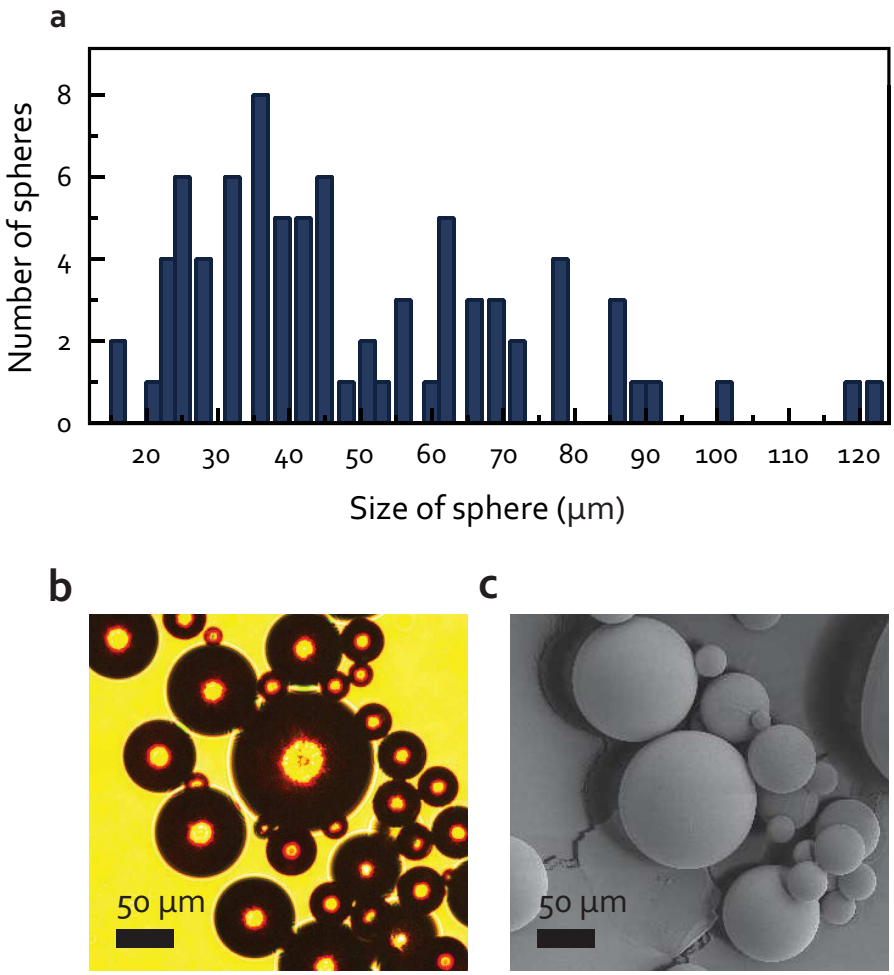

Figure 3.3: **BSA Microspheres** a) Size-distribution histogram of 80 BSA microspheres. b,c) Optical and SEM images of dye doped BSA microresonators, respectively.

3.2.2 Inkjet printed microspheres

For sensing purposes, one might see the advantage of mass producing WGM microsphere lasers with a fixed size with relative ease and speed. A direct writing process is a possible

approach. Inkjet printers are a cheap and powerful writing tools for highly controlled cavity size [171, 172, 173]. Duong Van Ta and myself have begun working on an ink-jet printer. This device uses an inkjet printing piezoactuator to dispense droplets on demand from an inkjet printing tip, illustrated in Figure 3.4. The droplets detach from the tip and land on a glass coverslip covered in PDMS. The glass is moved manually such that the droplets do not overlap. Currently the manual processing limits the fabrication to 5-10 microspheres per second; larger dispensing speeds lead to many instances of merging droplets. The implementation of a mechanical motor stage could lead to a larger dispensing frequency.

The process is versatile and there are a few ways of tuning the microsphere size:

1. Concentration of the polymer in aqueous solution;
2. Change the inkjet printer tip size;
3. Changing the voltage on the piezoactuator, this will result in different volumes being dispensed.

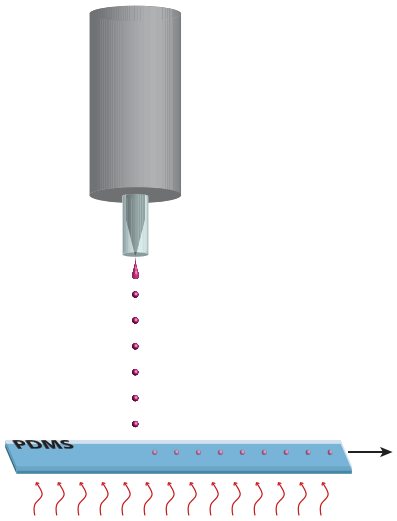

Figure 3.4: **Schematic of the inkjet printing.** The tip dispenses a fixed volume of doped polymer on to a glass substrate covered in PDMS. The substrate moves ensuring no more than one droplet falls in a single location. The substrate is heated to evaporate the water and solidify the doped polymer into a spherical geometry.

Due to the probability of clogging the tip with dried polymer, and to avoid multiple droplets being dispensed, we have kept the voltage high and constant and chosen the two other options as varying parameters. For the concentration of the polymer, we are typically

limited by the solubility of the polymer and dye in water, as well as the increase in likelihood of clogging the tip. To create larger droplets, we can use the mechanical stage previously suggested to produce multiple droplets in the same spot, causing them to merge to create a larger one. Lastly, the size of the tip dictates the volume dispensed, in our case we have purchased different diameters: 80 μm , 60 μm and 30 μm.

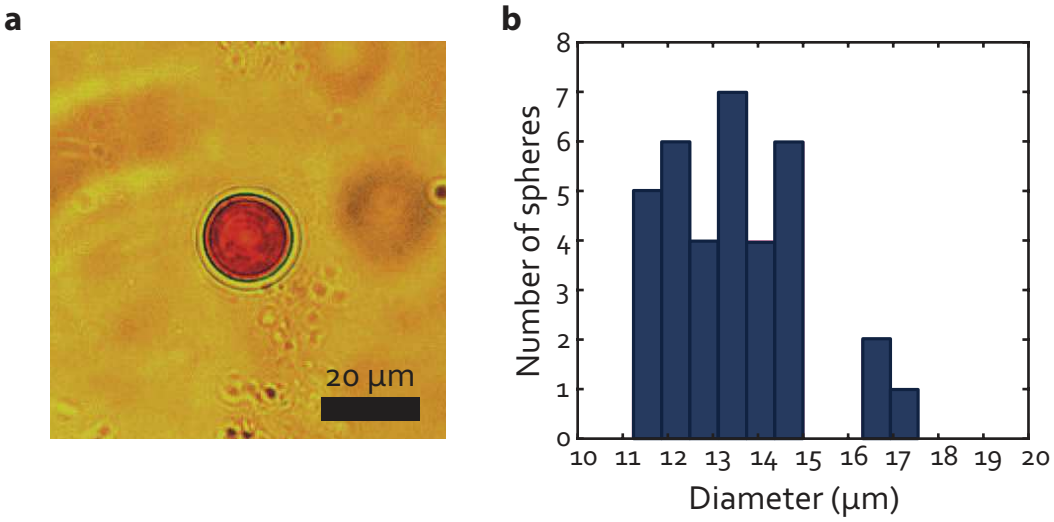

Figure 3.5: **Size distribution of PVA doped microspheres** created by inkjet printing of PVA solution of 3% wt and utilising an 80 μm diameter tip. a) Optical image of an inkjet printed WGM resonator b) Histogram with the size distribution of the microresonator diameter, revealing a mean size of 13.4μm

Preliminary tests have been conducted with doped polyvinyl alcohol (PVA); the concentration used was 3 %wt in deionised water: the tip used was the 80 μm. The size distribution of the diameter of 35 spheres is depicted in Figure 3.5b where the mean diameter was found to be 13.4 μm ±0.3μm. An optical image of one of the spheres obtained is depicted in Figure 3.5a. The sample size is not large enough to retrieve the Gaussian-like distribution expected. Additionally, a second distribution can be identified around D = 17 μm, volume calculations reveal that the diameter corresponds to roughly twice the volume of the 13 μm sphere and is thought to extend from a double droplet.

3.3 Lasing action in biocompatible microspheres

The lasing emission of the doped microspheres is characterised in the following section. The majority of the measurements reported here are performed in air unless stated otherwise and with an excitation $\lambda = 532$ nm and 500 ps pulse duration. The cavity loop is expected

to form in the region with lowest losses of the sphere. The emission can couple out of the sphere by scattering, which is subsequently collected by the microscope and measured by the spectrometer.

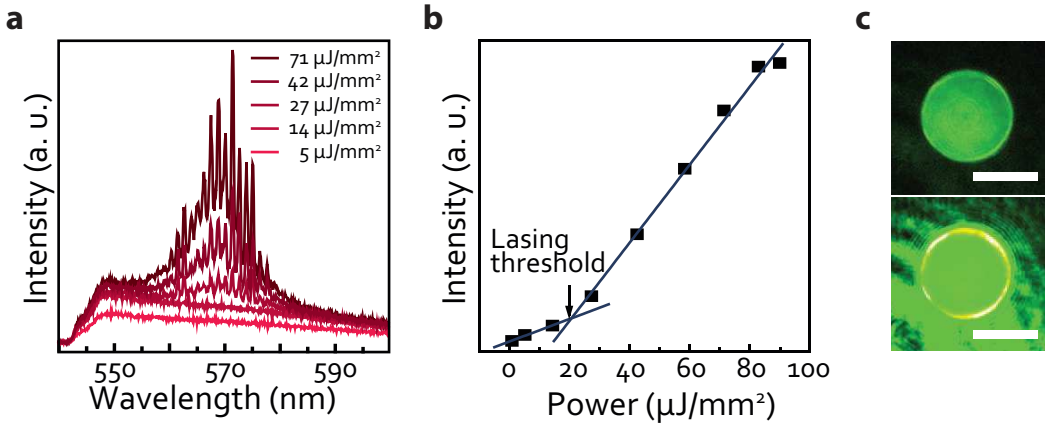

Figure 3.6: **Lasing emission of a biocompatible BSA microsphere laser.** a) The lasing spectra obtained from a fluorescein doped BSA sphere as function of pumping energy density. b) The corresponding integrated fluorescence intensity versus excited fluence. c) Presents fluorescence images of the studied sphere that is below and above lasing threshold. The bright ring observed above the threshold shows the evidence of WGMs. All scale bars are 30 µm.

3.3.1 Lasing of microspheres made of doped BSA, cellulose and pectin.

The fluorescence-to-lasing transition is best observed in the power dependent spectra as shown in Figure 3.6a. We experimentally observe WGM lasing from the fabricated dye doped microspheres upon pumping with a high-energy laser, as shown in Figures 3.6 and 3.7.

Firstly we evaluate microsphere lasing using fluorescein sodium salt as gain and BSA as the host material. BSA was dissolved in deionized water with concentration of 1g/1mL by leaving the mixture in a fridge (~4 °C) for about 24 hours. after complete dissolution a thick tubid solution is obtained and the relevant dye is added in aqueous solution. The mass of fluorescien added compared with the mass of the polymer is 0.8%wt. Fluoresceins as a class of dyes are efficient laser dyes, however are considered to be of low toxicity, instead for Rhodamines there is evidence of carcinogenicity in animals [174]. The absorption maximum for sodium fluorescein is $\sim 490\,nm$ depending on the solvent [175]. This is highly mismatched with the excitation wavelength. In practice this signifies that the

$\sigma_a(\lambda_{ex})$ is lower and a larger photon density is required to achieve lasing. Unexpectedly, we find that fluorescein has sufficient gain at the excitation wavelength ($\lambda_{ex} = 532\ nm$) given the limited energy density. A clear threshold behaviour is observed, as seen in Figure 3.6b. Under low pumping density ($< 20\ \mu J/mm^2$), the spectrum exhibits a spontaneous emission characterised broad linewidth as seen in Figure 3.6a in lighter pink. The emission from the sphere is uniform as observed in a camera image, depicted in the top image in Figure 3.6c. When the excitation density reaches $27\,\mu J/mm^2$, sharp peaks with wavelength from 560 nm to 580 nm start to appear, seen in dark pink in Figure 3.6a. Additionally, the WGM emission above threshold is evidenced by the bottom image in Figure 3.6c, where a yellow emission ring is visible above the laser scattering. As the pumping density increases, the output energy increases rapidly. The integrated fluorescence intensity shows a nonlinear increase versus excitation density (Figure 3.6b), indicating a distinct lasing threshold, which is about $20\,\mu J/mm^2$.

In the second case, the gain media selected was RhB, which matches our pump with an absorption maximum around 555 nm [176]. We fabricate RhB doped microspheres with BSA, cellulose and pectin where the ratio of dye weight to polymer is 0.33%, 2% and 1% respectively. The quantities are optimised for sphere formation (due to surface tension), dissolution of the dye and maximal gain. In the condition where distance between dye molecules is short, dimer are formed and excitation can migrate to neigbouring dye molecules, self-quenching the emission. This is the reason why not many rhodamine or fluorescein derivatives can be loaded on a single protein as they become non-fluorescent [177]. Dimer formation differs between different chemical envioroments, for example Rh6G in water exists as the monomer in concentrations below $\sim 8 \times 10^{-7} M$, however in ethanol Rh6G is in monomeric form for concentrations in the range of $1 \times 10^{-4} - 1 \times 10^{-5}$ [178].

The typical lasing spectra are plotted in figure 3.7a, b and c respectively, where the lasing modes are well recognised above the fluorescence background. With regards to the lasing threshold for spheres of similar sizes, the cellulose sphere has the highest value of $24\,\mu J/mm^2$, while the pectin and BSA spheres are considerably lower, around $5\,\mu J/mm^2$ and $1\,\mu J/mm^2$ respectively (Figure 3.7d-f). As expected, the threshold is greatly reduced when comparing RhB doped BSA and fluorescein doped BSA. For similar sizes of spheres the threshold for RhB doped BSA is more than an order of magnitude lower. The threshold is comparable to previous works on solid state lasers reported such as: intracellular droplet

lasers based on polystyrene cavities [8, 78], polymer ring resonator lasers [179], and performs better than the starch solid state lasers [180]. Since for consistency we choose to pump the full microsphere rather than the focus the laser light on the spheres edge we cannot do a full extensive comparison with further works.

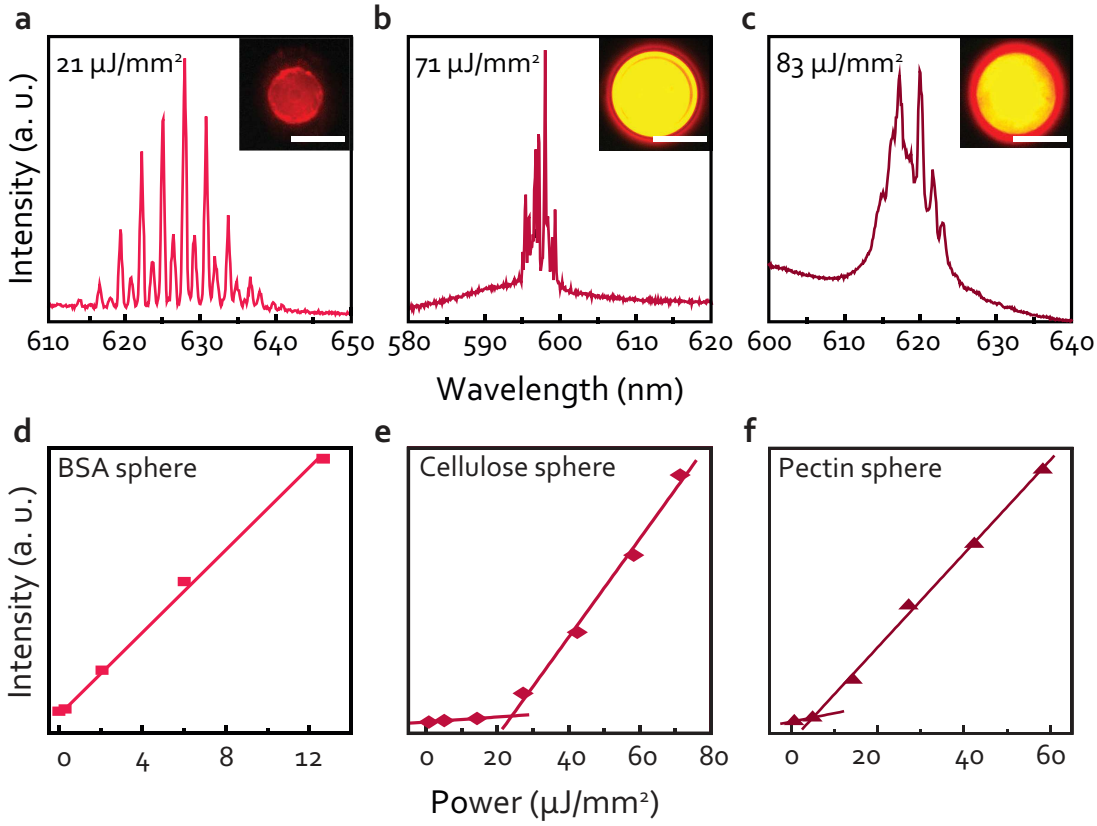

Figure 3.7: **Lasing emission and threshold of RhB doped biomaterials.** a - c Lasing spectra from typical RhB doped BSA, cellulose and pectin spheres respectively. The inset presents fluorescence images of the studied sphere above lasing threshold. All scale bars are 30 μm d-f Integrated fluorescence intensity versus pumping density for a typical BSA, cellulose and pectin microsphere respectively.

Generally, the lasing threshold increases with decreasing sphere size. As a result, the smallest lasing spheres would depend on the maximal allowed pumping energy. Given the maximum pump energy used for this experiments was$\sim$ 100 $\mu J/mm^2$; the smallest spheres to lase are 20 μm in diameter for BSA and 40 μm for pectin and cellulose. SEM inspection indicates that irrespective of the material used, the obtained microspheres have round shapes and diameters in the range of $D = 10 - 100\,\mu m$, evidenced by Figure 3.8. The high threshold obtained from the cellulose sphere is attributed to a high optical loss due to scattering of the sphere, which appears to be rougher at SEM image, seen in Figure

3.8c and f. The BSA spheres look very smooth in the SEM image in Figure 3.8a and d and exhibit the clearest mode spacing, which is convenient for investigation of the lasing mechanism. Cellulose exhibits the largest roughness as seen in Figure 3.8c, that said it is expected to have the largest losses and in consequence the largest threshold. On the other hand the pectin laser in Figure 3.8b and e is not as smooth as spheres made of BSA, yet the thresholds are very similar, this can be due to the higher concentration of dye present, although the confinement losses are larger, the gain is also larger.

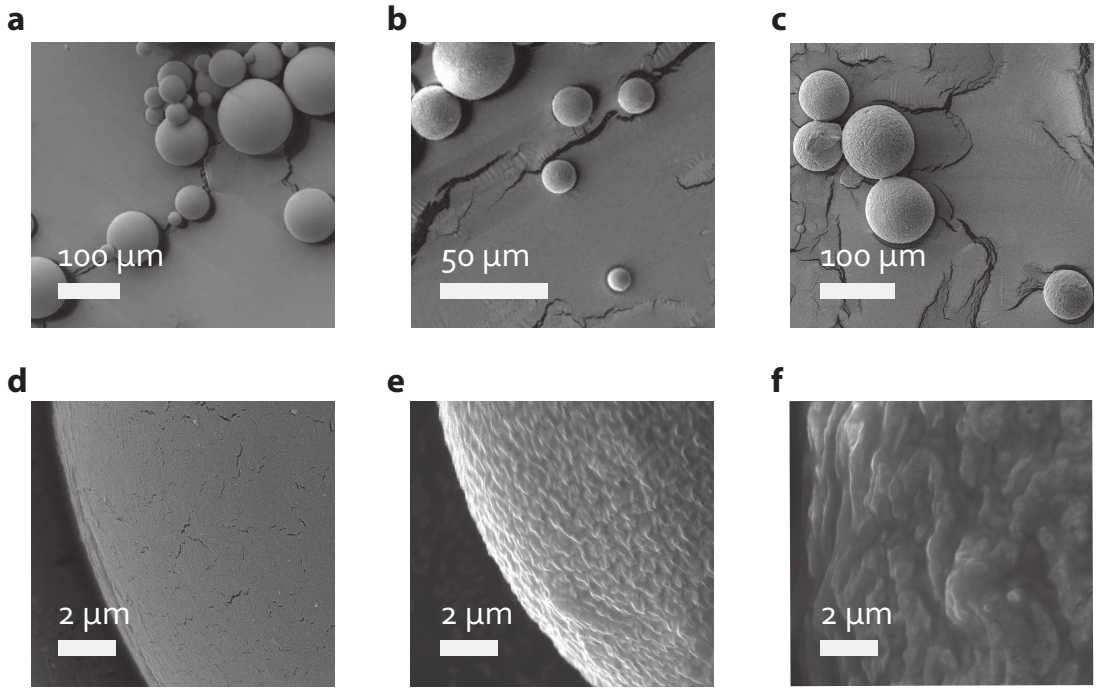

Figure 3.8: **SEM inspection of RhB doped biomaterial lasers.** a) - c) SEM images of dye doped BSA, pectin and cellulose microspheres respectively. d) - f) High magnification SEM images of BSA, pectin and cellulose spheres respectively the spheres were coated with a thin gold layer by means of thermal evaporation prior to SEM analysis.

3.3.2 Mode spacing of BSA microsphere laser

The quality of the WGM lasers can be inspected further by characterising the mode spacing. Given that RhB doped BSA yields the lowest threshold and clearest mode spacing, we evaluated a typical lasing spectrum from a 32 μm diameter RhB doped BSA microsphere seen in Figure 3.9.

The spectrum exhibits two separate envelopes with different intensity. The lasing envelope and mode position can be well explained by WGM theory. It is well known that

WGMs can be characterised by radial mode r, angular or azimuthal mode m and its polarisation, either transverse electric (TE) or transverse magnetic (TM) modes [79]. For a spherical cavity, TE modes are generally expected to have higher Q-factor than TM modes [181]. With this assumption, the lasing envelope with higher intensity is referred to TE modes while the other are referred to as TM modes. Consequently, lasing frequencies can be well-fitted by the asymptotic solutions of Mie scattering formalism [79].

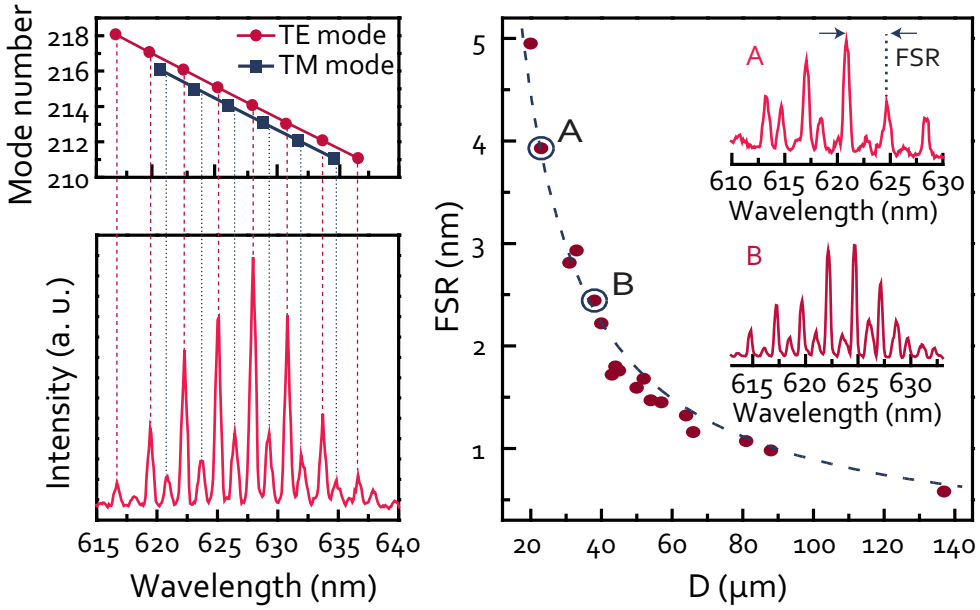

Figure 3.9: **Spectra characterisation of RhB doped BSA microlasers** a) Matching between experimental observation of lasing wavelengths and calculated lasing modes. b) FSR as a function of sphere diameters. The insets show spectra of two typical spheres with diameter of $D = 23\,\mu m$ (A) and $D = 38\,\mu m$ (B).

The TE modes are well matched with mode numbers of 211 to 218 and TM modes are indexed as 211 to 216 (all modes are first radial modes r = 1 as they have the highest Q value) assuming diameter of the sphere is $D = 31.53\,\mu m$, refractive index of the sphere $n_1 = 1.42$ and surrounding medium is $n_2 = 1$. The spectral linewidth, $\Delta\lambda$, of the lasing modes is as small as $0.2\,nm$, limited by the resolution of the spectrometer. The corresponding Q-factor, defined in the equation (1.24), is approximately 3×10^3. This Q-factor is ~ 3 times higher than a recently reported solid-state protein ring laser [182]. In order to better verify the WGM mechanism, the free spectral range (FSR) defined in equation (1.28), of microlasers with different sizes was investigated. Considering the resonant wavelength λ is about $625\,nm$. Using equation (1.28) the FSR of two WGM lasers of diameters: $D = 23\,\mu m$ and $D = 38\,\mu m$ is calculated to be $3.8\,nm$ and $2.3\,nm$ respectively. The spectra of each

sphere is seen in the inset of Figure 3.9b A and B, from which the FSR is determined to be 3.9 nm and 2.4 nm. The result shows an agreement between the theory and experimental observation, further verifying the WGM mechanism. Furthermore, as λ is similar for different spheres, the FSR of spheres of different size should follow a α/D function, where α is a constant. This is clearly seen in Figure 3.9b where the FSR as a function of sphere diameter is well-fitted by the function $89.2/D$ with $\alpha = 89.2$.

3.3.3 Photobleaching studies of a BSA microsphere laser

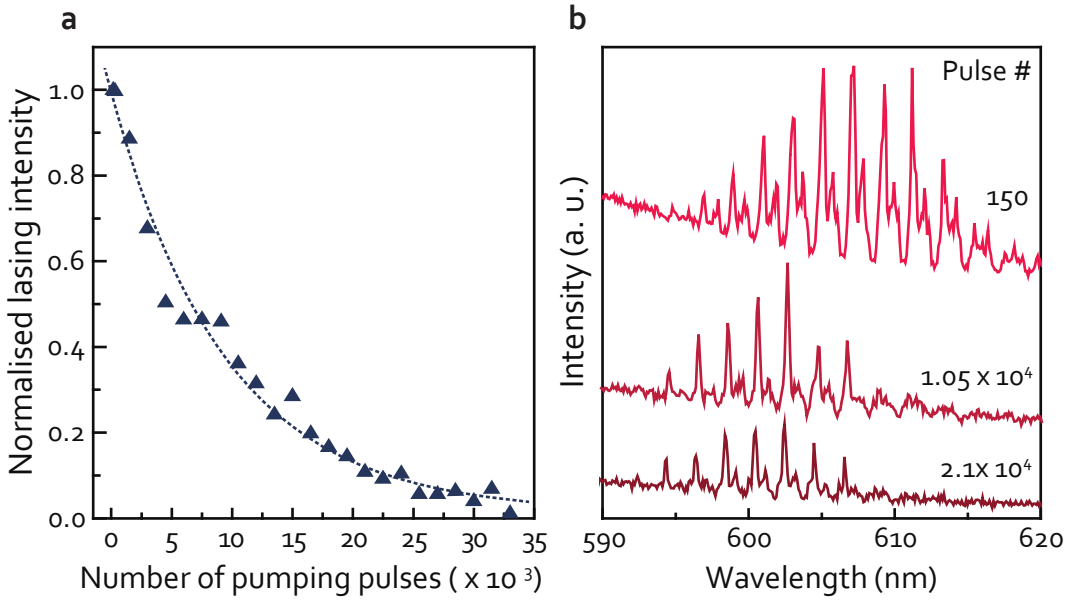

Figure 3.10: **Bleaching of RhB doped BSA micro laser.** a) Integrated lasing intensity from a typical RhB doped BSA sphere as function of pumping pulse operated in ambient conditions. b) Lasing spectra after a number of excited pulses.

To evaluate the lasing operation of RhB doped BSA spheres in air, a photobleaching study was conducted. Figure 3.10a shows the intensity degradation of a BSA sphere pumped sequentially with pump power 5 times greater than the threshold. The sphere continues lasing for as many as $\sim 3 \times 10^4$ excitation pulses. The laser lifetime is defined as the number of pulses by which the laser intensity decreases to $1/e$ of the original value; the intensity degradation decreases exponentially with the number of pumping pulses and has been fitted to Figure 3.10a. From the fit we obtained that $1/e \sim 10^4$ pulses. In Figure 3.10b the spectra sees a dramatic total intensity reduction between excitation number 150 and 2.1×10^4. Moreover, the maxima of the spectra is blue-shifted, thought to be due to the

oxidation of the laser dye, although the peak positions remain the same. Total intensity and peak spacing are both realiable sensing transducers in this configuration, due to the blue shift of the spectra single peaks could not be used as indicatores. Although here we aim to demonstrate stability over high energy pumping of BSA sphere lasers, one could consider to reduce the pump to lower a lower energy still above threshold to improve the stability and blue shift.

Overall we have shown that RhB doped BSA microsphere laser are very stable in ambient conditions and can be pumped hundreds of times without a significant change in the spectral output. For potential application in the medical field, stability and durability are essential traits which our BSA microspheres possess.

3.4 Biocompatibility of BSA microsphere lasers

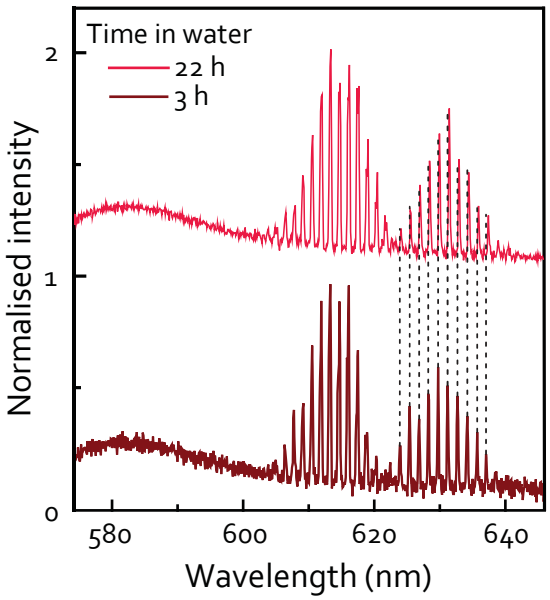

Figure 3.11: **Lasing spectra from a typical RhB doped BSA sphere operated in water versus time.** The spectra of a single BSA microsphere laser (D $\sim$ 30 μm) is compared after 3h (magenta) and 22h (pink) in deionised water. The spectrum is vertically shifted for clarification. Little variation is observed after a timelapse of almost 20 h.

It is paramount for a potentially implantable device to be able to operate under biological conditions: in liquid, as well as to have low levels of toxicity. In this section we will evaluate the laser operation in water and the biocompatibility of the device in a very simple manner by putting a laser in cell culture and qualitatively observing the effect on the cells.

3.4.1 Lasing operation in aqueous media

A BSA laser ($D \sim 30\mu m$) is placed in deionised water and lasing experiments are conducted with a pump power of $\sim 100\,\mu J/mm^2$. We use the degradation of the modes as a measure of the stability of the laser. The spectra after 3h and 22h in water is plotted in Figure 3.11, correspondingly on the bottom and top of the figure. The lasing mode and intensity of an individual sphere only changes slightly ($0.1\,nm - 0.2\,nm$) after immersion in water for 22 hours, this is consistent with a slight swelling of the BSA sphere. In contrast, cellulose and pectin spheres tend to hydrate, swell and dissolve in water after several hours in the case of cellulose and a week for pectin. Consequently, we did not observe lasing from those spheres when they were in water.

3.4.2 Cell compatibility

To qualitatively assess the biocompatibility of our lasers, a simple experiment was carried out based on the replication rate of a human cell line, HeLa, when incubated in presence of biolaser microparticles. At least 50 spheres per culture well were immersed in culture medium with HeLa cells and incubated for up to 4 days. All optical characterisation of cell-containing samples were conducted under ambient conditions for no longer than 1h after removal from the incubator to minimise cell damage. The presence of BSA spheres did not prevent cell growth or division. Additionally, no inhibition area was observed surrounding the laser particles. When compared to a control sample without spheres, the cells were found to split at similar rates and reached confluence after 4 days. In addition, during the 4 days of measurement, BSA spheres continued to lase in the culture medium with only a minor decrease in the lasing intensity. While this is an indication of biocompatibility, a full cytotoxicity study should be conducted once a specific cell type of interest is identified for a specific biomedical applications. Furthermore, BSA spheres kept in culture conditions for more than a month continued to lase with a minor degradation of the threshold. Figure 3.12 shows a BSA sphere microlaser surrounded by many HeLa cells after 3 days of incubation. Here, the cells have been fixed and stained for 3D confocal imaging. The cells were incubated with 5% Formaldehyde for 10 min, washed several times with phosphate buffer solution (PBS) and subsequently stained with Alexa Flour 488 for 10 min, and washed repeatedly with PBS; this process fixes the cells and stains the cellar membrane green. Images

of each channel were captured with a Nikon Eclipse Ti-E Inverted microscope using a 40X Plan Apo objective. The green channel represents 488 nm excitation and 525 nm emission, while the red channel represents 562 nm excitation and 595 nm emission. The leaked RhB from the microspheres is thought to permeate the cellular membrane and as a result stains the mitochondria of the cell, giving the cell a red colour. Images were processed with NIS-Elements.

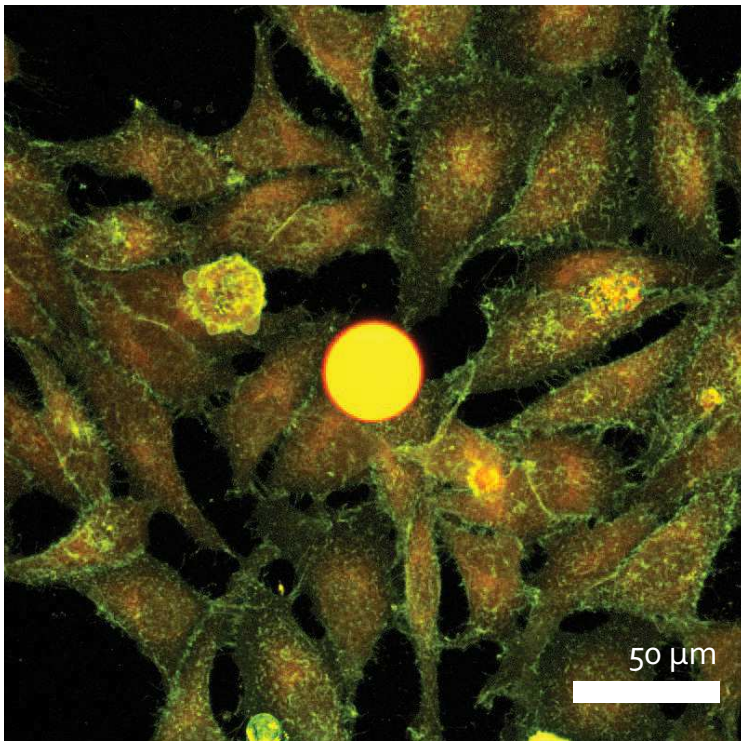

Figure 3.12: **HeLa cells cultured with RhB doped BSA lasers.** Confocal 3D scan (top view) of a biocompatible microlaser made of a RhB doped BSA microsphere (in orange) surrounded by HeLa cells after 3 days of incubation. The cells were fixed with 5% formaldehyde and the cellular membrane was stained with Alexa Fluor 488.

3.5 Other biocompatible materials

Several biocompatible materials were exploited for WGM lasing, namely fibroin protein from silk and Silica.

Fibroin was mixed in solution with RhB and the solution was drawn in PDMS following the procedure illustrated in Figure 3.1. Initial results lead to deformed microspheres like the one seen in Figure 3.13a. A zoomed in image of the surface is depicted in Figure 3.13b,

showing a very uneven surface with a roughness on the μm scale. The surface tension between the water and the silk was greatly reduced when compared to other materials described, the assembly of fibres into microspheres took several minutes, forming non-spherical objects. It is thought that the sensitivity of amorphous silk to external stimuli (e.g. heating and stirring) may be causing gelation, followed by wrinkles formed during evaporation of water. The formation of smooth spherical lasers is essential for high Q-factor WGM lasing with low threshold.

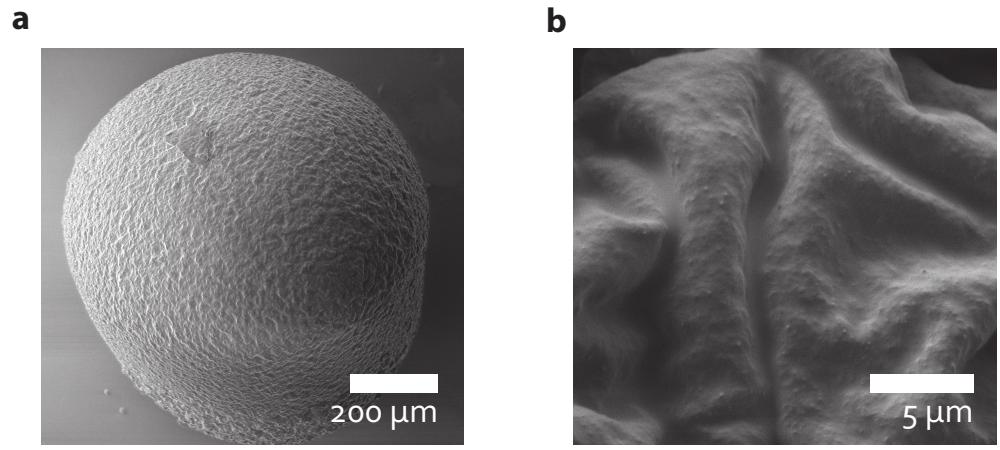

Figure 3.13: **RhB doped silk microsphere.** a) SEM of a silk microsphere. b) Surface of a silk microsphere.

Silica is doped with RhB and processed using methods described above. In contrast to silk, silica yields smooth spheres with good properties, as illustrated in Figure 3.14. Silica is a biocompatible material, which can be obtained through the hydration of tetraethyl orthosilicate (TEOS). Hydrochloric acid (HCl) is added and serves as a catalyst, increasing the rate of reaction. Initially the compounds do not mix, and stirring is required. Once the solution is homogeneous dye is added.

The lasing properties of a small $D = 8\,\mu m$ is evaluated as seen in the top inset of Figure 3.14a. The lasing spectra yields four very sharp peaks, with an estimated Q $\sim 3 \times 10^4$, an order of magnitude larger than that for the BSA lasers. The modes spacing matches the theoretically predicted by equation for a sphere of such size. Furthermore, preliminary studies indicate that silica WGM lasers operate in aqueous environment.

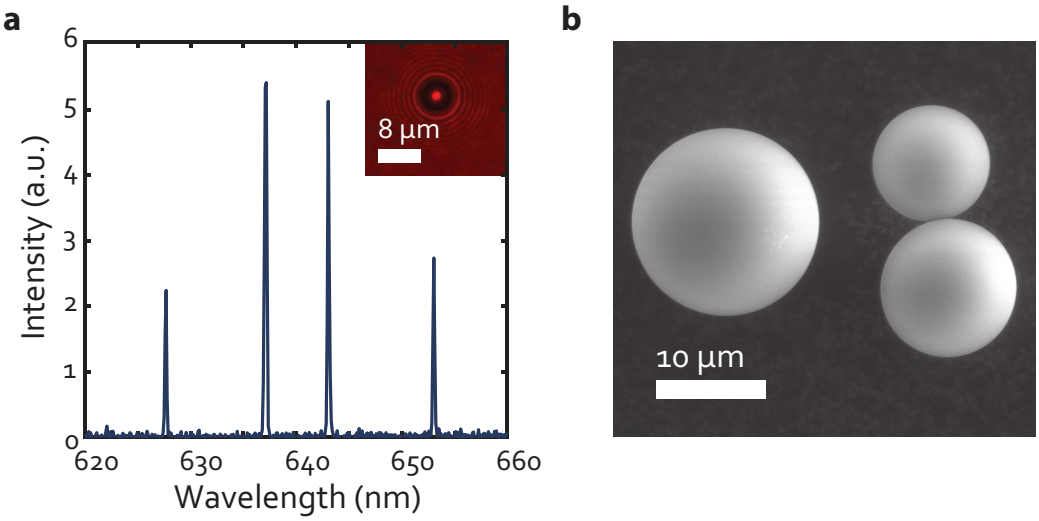

Figure 3.14: **RhB doped silica WGM laser**. a) Spectra of an 8 μm silica microsphere with pump energy 140 $\mu J/mm^2$, integrated over 4 pulses using a X20 objective. In the inset is an optical image of the sphere in question. b) SEM of the silica WGM lasers, imaged in low vacuum and in absence of coating. The microspheres appear very smooth.

3.6 Outlook/Conclusion

In conclusion, we have demonstrated solid-state miniature biolasers based on natural proteins and polysaccharides. Laser size ranges from 10 to 100 µm. The lasing mechanism is attributed to WGMs. Owing to low optical loss, the lasing threshold is only a few $\mu J/mm^2$, which similar to other solid state lasers reported such as: intracellular droplet lasers based on polystyrene cavities [8, 78], polymer ring resonator lasers [179], and performs better than the starch solid state lasers[180]. With Q factors of lasing modes as high as $Q \sim 3\times10^3$, BSA microlasers were found to be resistant to the aqueous environment and cell culture media, and biocompatible to cell growth. Stability in biological condition could be improved using a specific coating, for example in the form of a silica layer. The fabrication process relies on aqueous solutions, thus it is flexible and compatible with other biomaterials and other biocompatible gain media like vitamins [75] or Green Fluorescent Protein (GFP) [183], enabling different kinds of all-biomaterial solid-state microlasers.

Silica WGM lasers as small as D $\sim 8\,\mu m$ show lasing behaviour, opening doors for possible integration into living cells. At the moment the largest microspheres to be engulfed by a microphages and non-phagocytic cells (such as HeLa cells) are placed at $\sim 20\,\mu m$ [8].

Due to the simplicity of operation and ease of fabrication, WGM biolasers are promising

for future biosensing applications. These lasers have potential for future ultrahigh-sensitive sensors, and could allow scientists to monitor biological interactions in real time.

4 Biocompatible Random lasing

Lasers made from disordered biological materials have the potential to produce new coherent light sources, flexible and compatible for living tissue integration [56]. Additionally, biolasers have the ability to harness the power of stimulated emission for biosensing and cell tagging and tracking [78]. So far all-biological lasers have been devised using conventional lasing schemes, such as spherical microresonators [75], microcavities [151] and recently even implanted into live cells [8, 78]. While high-Q cavities favour lasing, their requirement for precise geometry limits the applications for dynamic systems like living tissues. Instead, random lasing is emerging as a simple, robust, and easy to integrate, source of stimulated radiation, relying on disorder and multiple scattering to fold the optical paths inside the gain medium to trigger lasing [9, 184]. Moreover, it is not influenced by the material's overall shape but instead it relies on its internal heterogeneity, therefore it can easily adapt to biological media with the ability to withstand stretching, wetness, and heat: its form is naturally biocompatible.

4.1 Introduction

In recent years random lasing with biocompatible materials has been a growing interest for photonic applications. Random lasing has been observed from a multitude of different biomaterials such as: DNA [92, 185], starch [186], cellulose [84, 85, 187] and in biological tissues [87, 86].

This chapter focuses on different strategies for fabrication of biocompatible random lasers, their optical characterisation and their operation in biological media.

4.2 Silk random lasing

Silk fibroin is a very versatile protein, it is biocompatible and biodegradable, and has outstanding mechanical properties [110, 188]. In particular, silk lasers with conventional geometries have been reported [150, 189]. In this section, building upon fabrication strategies discussed in previous chapters, we will discuss the fabrication of the highly scattering fibroin incorporated with gain, the first fibroin random laser. Additionally, its optical properties will be examined in both air and liquid.

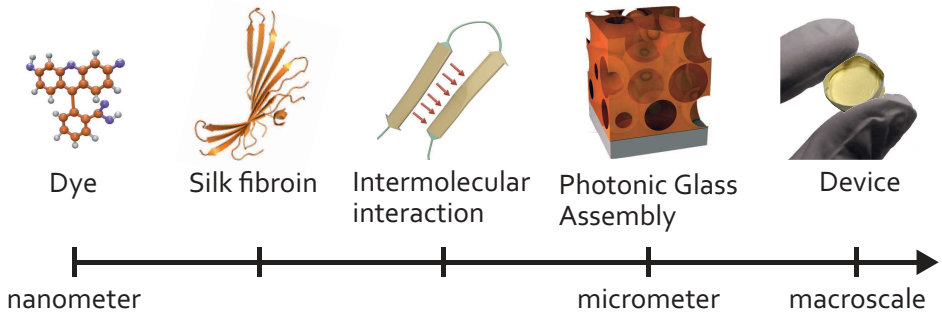

Figure 4.1: **Material multi-scale integration from the nanoscale to the macroscale.** The dye, fluorescein sodium salt is interfaced with silk fibroin. As the water is evaporating from the solution the molecule assembles into a pseudo-crystalline structure. The inverse photonic glass is made with this solution. The final device is illustrated on the right hand side of the figure.

Bulk silk is obtained from *Bombyx Mori* silk worm. The silk cocoons are boiled and purified. Glycoproteins which provoke an immunogenetic response in humans are removed such that a pure solution of silk fibroin is remaining. Details on the purifying procedure are reported in reference [110].

Silk films, fabricated by casting the aqueous solution on to a substrate and dried or by spin coating, are transparent and very flat, making them interesting for photonic applications. Here, using fabrication methods described in chapter 2, silk films are cast and nanostructured giving rise to a white and opaque slab of silk. Gain, paramount to lasing, is obtained from laser dyes and incorporated by intermolecular interactions into the silk matrix before the drying process. Fibroin is especially suited to interface with organic and inorganic molecules in its matrix without affecting its emission [114]. Therefore, many sources of gain could in principal be used and interface with silk. Here we use two organic molecules: sodium fluorescein and rhodamine 6G (Rh6G), with low toxicity they could be well suited for future implantation in the human body [63].

The fabrication schematic is shown step by step in Figure 4.1 which describes the multi-scale integration of the various components. Gain molecules, fluorescein, depicted in Figure 4.1, or Rh6G, are dissolved in deionised water and subsequently added to an aqueous solution of silk $(3-7\%wt)$, such that the dry ratio is 99.5 $\%wt$ of fibroin and 0.5 $\%wt$ of dye. Polystyrene spheres (PS) of diameter d $= 1.27\,\mu m$ and silk are mixed together directly, as the protein destabilises the colloidal suspension, forcing the flocculation of the PS spheres, analogous to what was observed for cellulose nanocrystals in chapter 2. The dye molecules are encapsulated in the silk during the drying process, through hydrophobic interactions established with the protein, denominated in the Figure 4.1 as the stage of intermolecular assembly. The silk scaffolding is expected to provide thermal dissipation and decrease intermolecular quenching, similar to that reported for DNA matrices [92].

The films are dried in an oven at constant temperature (30^0C) to avoid cracking. Once dry, the samples where chemically etched in a 99% toluene bath for 72 h, in order to selectively dissolve the PS sphere. A small fraction of the dye was released in the toluene solution during the etching process. There is no evidence to suggest that the toluene disrupts the secondary or tertiary structure of the silk protein. At the macroscale the pore size is consistent with the PS beads used and the transport properties evaluated in the next section are consistent with those measured for CNCs inverse photonic glass. Denaturing of the protein is not directly investigated in this thesis, nevertheless we are able to form an insoluble matrix of silk consistent with a high degree of crystallisation of the protein [190], which suggests a the fibroin does not suffer a high degree of denaturing.

The result is a disordered fibroin matrix with connected spherical pores, in other words

a 3D inverse photonic glass structure. The spheres arrange in a solid packing, with a final filling fraction of ≈ 45%–55% estimated by volume measurements via electron microscopy. A scanning electron microscope image (SEM) in Figure 4.2 presents the nanostructured silk structure. In addition, the silk nanostructured material can be made free-standing with no loss of functionalities, by simply growing the material over a PS film cast on the glass substrate, film which was then dissolved during the same sphere etching process, similar to the procedure described for cellulose.

Fibroin naturally crystallises during the drying process, however it can be influenced by external factors such as humidity and temperature and in consequence the speed at which is dries. For reproducible conditions, more sample stability in water and slower degradability, a high degree of crystallisation, than that accomplished in ambient conditions, was achieved by exposing it to water vapour for 12 h in a vacuum desiccator at 70^oC [191]. This technique could be utilised further for control of the mechanical strength, degradation rate and cell response [191].

Whereas in the absence of dyes the silk sample is white and opaque, when doped with fluorescein it takes on a yellowish colour as illustrated in the photo in the last step of Figure 4.1. For Rh6G doping the sample takes on a bright pink colour.

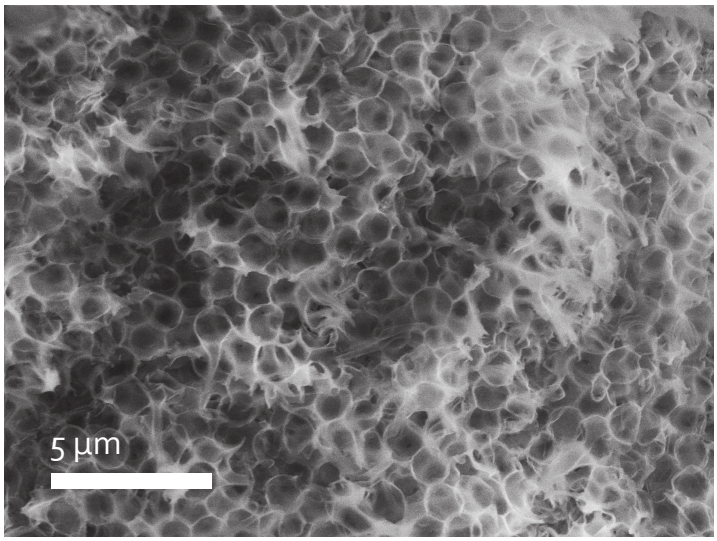

Figure 4.2: **A scanning electron microscopy image of the final structure**, highlighting the pores and the silk structure.

The final amount of dye in the samples discussed is $< 0.3\,mg$, which corresponds to$\approx$ $10\,ng$ for a $100 \times 100 \times 100\ \mu m$ sample; less than $0.1\,mg/mL$ which is considered a non-

toxic amount of fluorescein. It is important to note that the silk in solution is sensitive to pH changes and an abrupt change can lead to instantaneous gelation of the silk. Gelation of fibroin is accompanied by a structural transition from random coil to β-sheets in solution and the formation of hydrogen bonds between the fibroin molecules into a gel network. To avoid this the dyes were added in dilute concentrations ($< 0.1\%$ of the dye in deionised water).

4.2.1 Transport of light in nanostructured silk

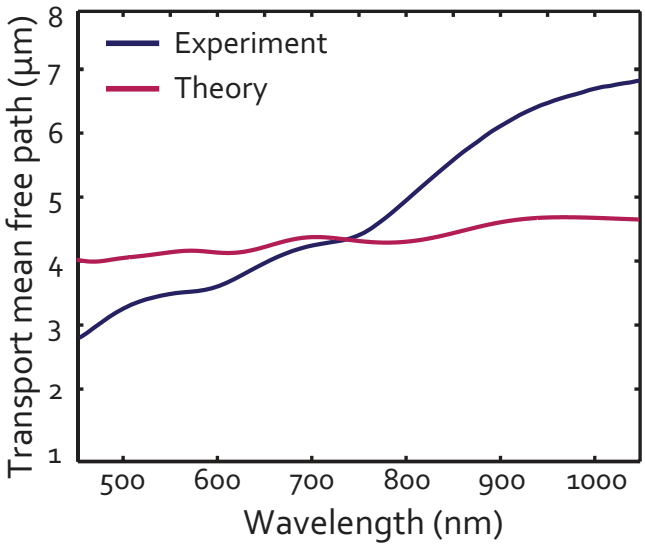

Figure 4.3: **Transport mean free path of an inverse photonic glass made entirely of silk.** In blue is the experimental result, while the theoretical result for $n_{silk} = 1.6$ and $f = 0.5$ is plotted in pink

In the following section the light transport properties of a silk inverse photonic glass in the absence of gain will be investigated. The total transmission through undoped nanostructured silk is measured using a integrating sphere for films of different thickness. A more complete description of the experimental method can be found in the introduction. The optical Ohm's law in equation (1.13) is used to fit the transmission as a function of slab thickness and the light wavelength. The silk inverted photonic glass is characterised in Figure 4.3. The measured transport mean free path ℓ_t is in the range $\ell_t \approx 3-7\,\mu m$ (blue line), with minor resonant modulations due to collective Mie scattering resonances, which can be engineered either by changing the diameter of the air voids or their refractive index. The thickness of the inverse silk photonic glass has been measured via scanning electron microscopy images, with an error smaller than 10% (statistical error from repeated mea-

surements). The theoretical calculation of ℓ_t (pink line) puts it between $\ell_t \approx 4-5\,\mu m$. Although, a qualitative agreement between theory and experiment is evident, the shift in the resonances and intensity discrepancy are attributed to the limited validity of the independent scattering approximation for a closed-packed system such as the one investigated here.

4.2.2 Lasing in nanostructured silk with gain

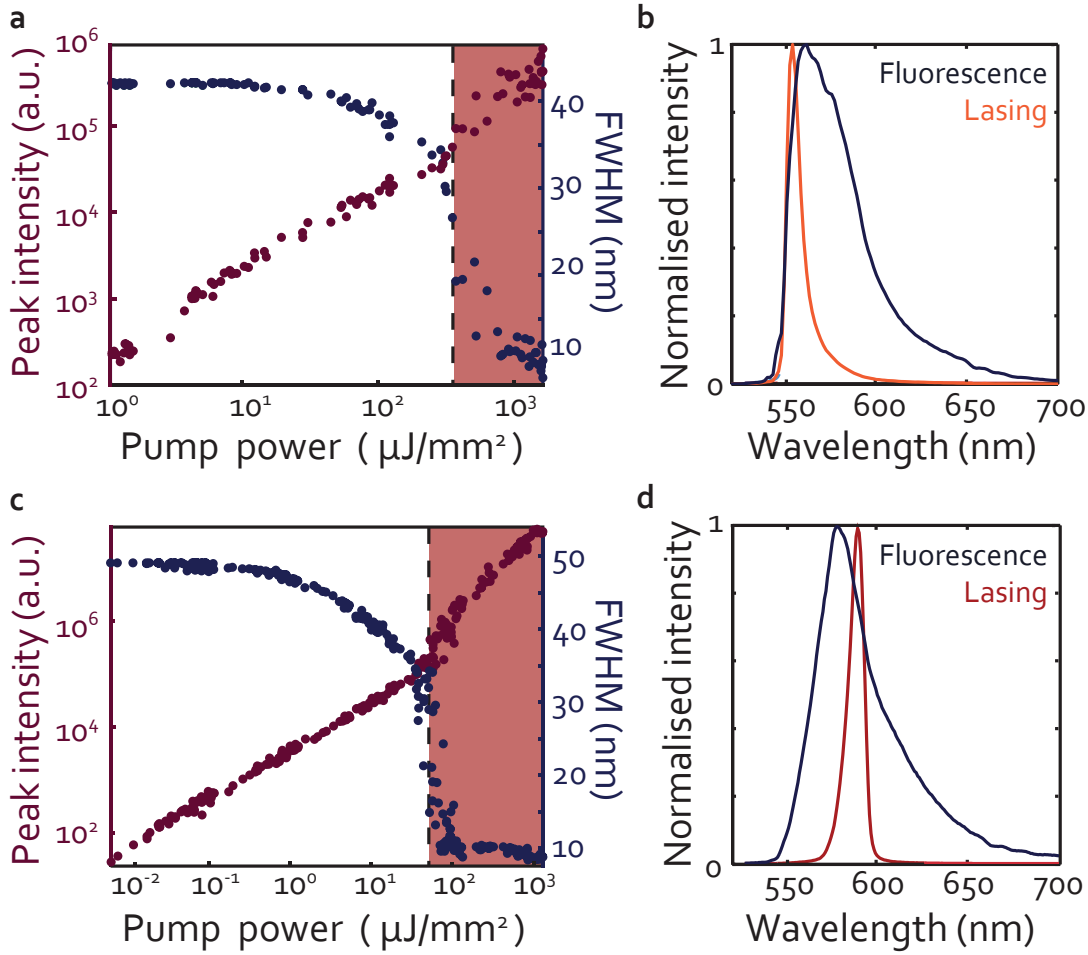

Figure 4.4: **Lasing plots from Silk doped inverse photonic glass.** a) Typical lasing plot for silk doped with Sodium fluorescein. The laser peak intensity (purple circles) and the evolution of the emission line (blue circles) are both plotted as a function of pump power. The red rectangle illustrates the lasing region above threshold $P = 380\,\mu J/mm^2$. b) Comparison of fluorescence spectra and the lasing spectra above threshold. c) Typical lasing plot for silk doped with Rh6G. The laser peak intensity (purple circles) and the evolution of the emission line (blue circles) are both plotted as a function of pump power. The red rectangle illustrates the lasing region above threshold $P = 70\,\mu J/mm^2$. d) Comparison between the fluorescence spectra and the lasing spectra above threshold of Rh6G doped silk.

The emission properties of the silk random lasers are evaluated in this section. The pump used was a second harmonic of an Nd:YAG Q-switched pulsed laser. Single excitation pulses were used at 532 nm wavelength, 6 ns pulse duration with a pump diameter of $\approx$ 2 mm. The detection software registers single pulse energy and emission spectra for each pulse. The large energy range of 5–6 orders of magnitude is achieved by a combination of neutral density filters for the coarse control and a half-waveplate and a polariser for the fine control. The crossover from fluorescent to lasing emission can be observed by recording the emission spectrum while increasing the exciting laser power.

The silk random laser proves to be a very efficient lasing system as illustrated in Figures 4.4a and b and Figures 4.4c and d for fluorescein and Rh6G as doping agents respectively. At low pump power the sample is limited to spontaneous emission, also known as fluorescence. Fluorescence is characterised by the broad emission, seen in Figure 4.4b and 4.4d in dark blue for fluorescein ($270\mu J/mm^2$) and Rh6G respectively ($40\mu J/mm^2$). A sudden increase in the emitted light intensity (purple circles) and sudden spectral narrowing (blue circles) is observed when the pump power reaches a critical value, i.e., the lasing threshold. The threshold occurs at $380\,\mu J/mm^2$ of pump energy for fluorescein and $70\,\mu J/mm^2$ for Rh6G, which compares favourably to similar systems in other material hosts [91, 192].

After the threshold, stimulated emission becomes the dominant emission process and random lasing action occurs. The spectral linewidth above threshold is plotted in Figure 4.4b in blue for the sodium fluorescein random laser, at 1000 $\mu J/mm^2$ pump power, in orange. For the Rh6G doped inverse photonic glass, the spectra, for a pump well into the lasing regime (pump power of 1600 $\mu J/mm^2$) is plotted Figure 4.4d in red. The smallest linewidth observed for both dyes was around 8 nm. The threshold is conventionally defined as the point of inflection in the emission plot in Figure 4.4. Given this definition, the threshold is clearly identifiable in the Rh6G plot, in Figure 4.4c, seen in logarithmic scale as a shift in the y-axis. Due to the noise and non-linearity of the lasing system it is not clear in the case of fluorescein. Here, we have defined the threshold as the point where the full width half maximum (FWHM) reaches a mid point between the fluorescence and lasing FWHM.

A small frequency shift of the emission upon increasing pumping energy is observed, from 559 nm to 552 nm for fluorescein, and from 578 nm to589 nm for Rh6G, typical for random lasing, as the lasing frequency depends on the interplay of scattering and net gain

[91, 192]. The emission spectra are smooth curves as one would expect for diffusive or incoherent random lasing with non-resonant feedback [9, 184].

The silk fibroin lasers are capable of lasing even after being stored for one year. Additionally the lasers prove to be stable over many excitation cycles and no significant difference is observed in the lasing output besides a small dye bleaching. The bleaching statistics are shown in Figure 4.5, the intensity decay follows an exponential curve. The samples were excited with single pulse around $P = 325\,\mu J/mm^2 \pm 33\,\mu J/mm^2$, in both cases well above threshold. Measurements were taken every few minutes for almost an hour in the case of fibroin doped random laser. By fitting the curve we obtained that $e^{-1} \approx 2400$ pulses for sodium fluorescein doped inverse photonic glass and $e^{-1} \approx 13600$ pulses for Rh6G doped inverse photonic glass. Results indicate that Rh6G doped silk is more resilient than silk doped with fluorescein. This is probably due to the dye interaction with the fibroin, as further supported by the more significant leaching of fluorescein when the sample is placed in water.

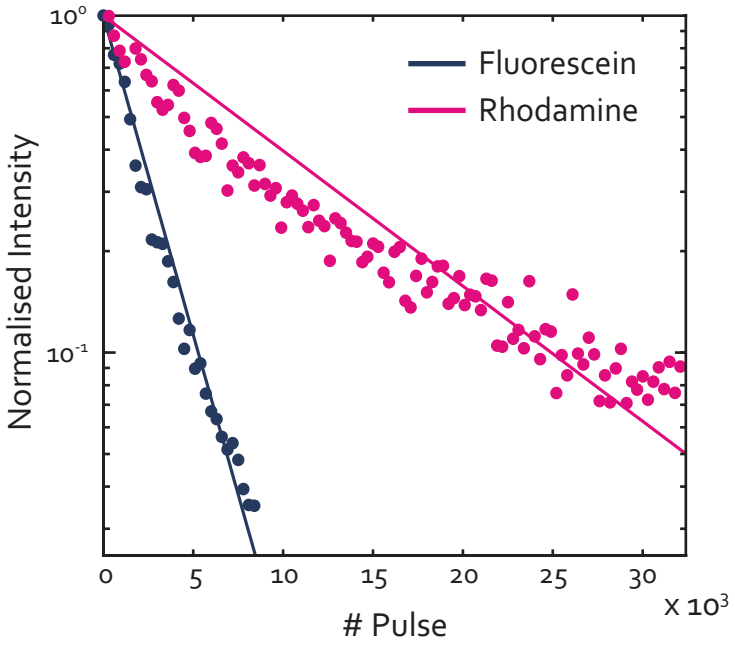

Figure 4.5: **Bleaching of the inverse photonic glass random lasers**. In blue circles is the intensity attenuation as a function of the number of pulses for the sodium fluorescein doped random laser in blue circles and in pink circles and for Rh6G doped random laser. The blue and pink line represent the exponential fit for the sodium fluorescein and rhodamine laser respectively.

4.2.2.1 Lasing in aqueous media

The body is largely made up of water, therefore operation under biological conditions are paramount for the application in the human body. In this section we present the operation of silk random lasers in aqueous environment. Additionally we will study how the transport and lasing properties both theoretically and experimentally.

When the random laser is operated in an aqueous environment such as a biological media, the scattering strength is reduced as compared to air operation. For a fixed sample size L the threshold will increase, given a smaller refractive index contrast between the silk matrix and the voids.

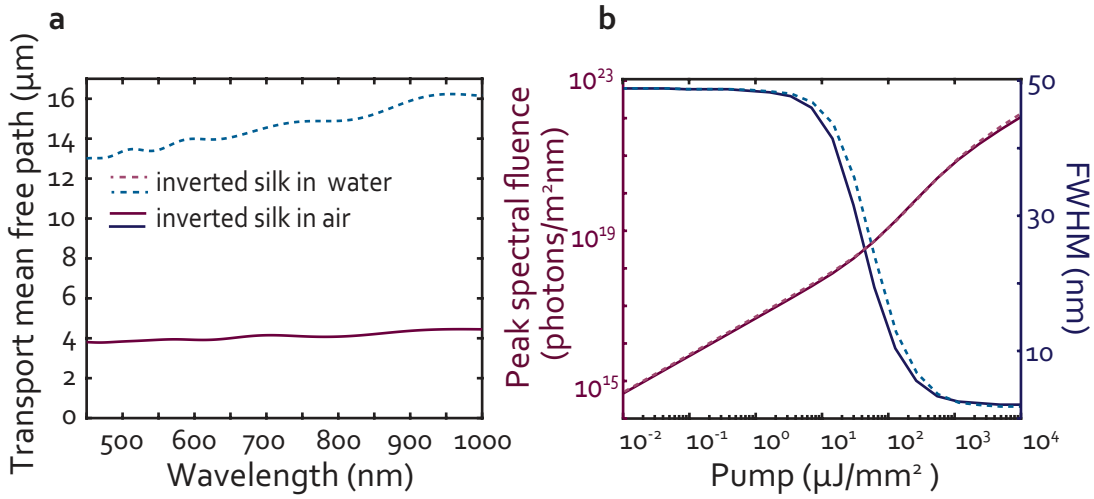

Figure 4.6: **Theoretical calculation of the modified scattering and laser properties when in water.** a) Shows the predicted transport mean free path length of the inverted silk photonic glass structure obtained from Mie theory and independent scattering approximation. The purple line is the inverse structure when in air composed of air voids in silk while the blue dashed line is the calculation in water. The transport mean free path increases by a factor of 3-4 from $\sim 4\,\mu m$ to $\sim 14\,\mu m$. b) Shows the predicted random lasing action with the parameters $L = 100\,\mu m$, but with different scattering length (full line air-operation, dashed line water-operation) which results in an increased threshold from $50\,\mu J/mm^2$ to $70\,\mu J/mm^2$.

The change in the transport and lasing dynamics can be calculated using theoretical models expressed in the introductory chapter 1. ℓ_t is calculated in Figure 4.6a where ℓ_t increases from $\sim 4\,\mu m$ to $\sim 14\,\mu m$. For a Rh6G doped inverse photonic glass the increase of a factor of $3-4$ times in ℓ_t, leads to a theoretical increase of threshold of 30% from $50\,\mu J/mm^2$ to $70\,\mu J/mm^2$ as seen in Figure 4.6b for a sample $L = 100\,\mu m$. Experimentally, we evaluate the spectra as a function of pump power for the sample in the dry state and in

the wet state, as seen in Figure 4.7. The threshold suffers a 50% increase when the device is immersed in water, from 150 $\mu J/mm^2$ to 290 $\mu J/mm^2$. Lasing operation is still achieved with low thresholds, this is due to the small active length compared to the L. When the ℓ_t increases in water, the diffusive volume also increases and the increased gain available partially compensates for the loss of light confinement. Despite the increase in threshold, random lasing action can be achieved experimentally, albeit in practice the laser threshold increases by 50% as shown in Figure 4.7.

We can calculate the critical length of our slab random laser, that is the minimum thickness below which lasing cannot be achieved. Given that $\ell_g \approx 5\,\mu m$ that leads to a critical length $L_{cr} \approx 10\,\mu m$ in air and $L_{cr} \approx 20\,\mu m$ in water. Given the limit on the pump power available the practical limiting thickness is expected to be much greater.

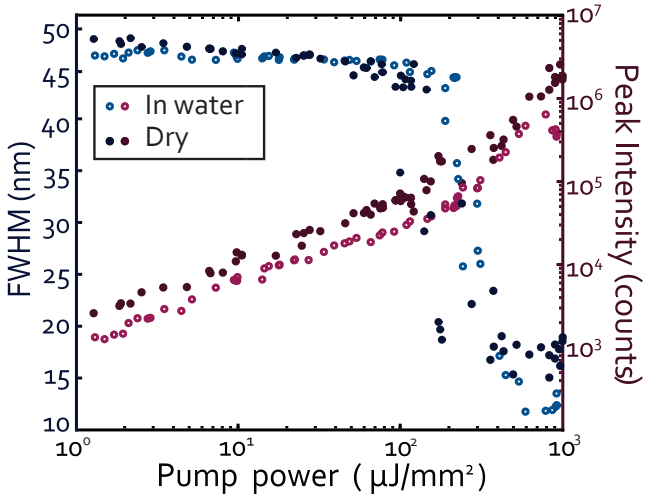

Figure 4.7: **Experimental laser properties when in wate**r. Lasing action for rhodamine-doped silk random laser in air (dark blue and purple circles) and water (light blue and pink circles). The blue open and full circles are the FWHM plotted versus pump power, while the purple and pink circles are the peak intensity. When the device is immersed in water the lasing threshold is shifted toward larger values (≈50% increase).

4.3 Miniaturisation of Random lasers

Lasers are widely employed in biomedical applications, including imaging, therapeutical treatments, and diagnostics. The ability to implant miniaturised lasers, smaller than a few microns is promising and may lead to new opportunities in medicine. For example, they have the potential to be implanted and offer access to a spatial map of the compound we aim

to probe, while offering very close interaction with the target tissue. Micron sized lasers have been achieved using biocompatible materials, reliant on WGM microsphere lasers such as the ones we have presented before. There are still vast opportunities to exploit both for materials and geometry, with downfalls related to each. Semiconductor materials of certain types such as ZnO [193], perovkites [60] and GaAs [50] have intrinsic gain and high refractive index and therefore can be easily sub-micron in size, however biointegration is a challenge [78].

Miniaturisation of random lasers is a key aspect to address for to in body implantation, on tissue and in cell sensing. Thus far we have produced a sample of 1.5 cm in diameter and 100 μm in thickness. In this section we will focus on a technique developed for the miniaturisation of biocompatible random laser. The most straight forward method is derived from fabrication techniques discussed previously.

4.3.1 Fabrication of spherical random lasers

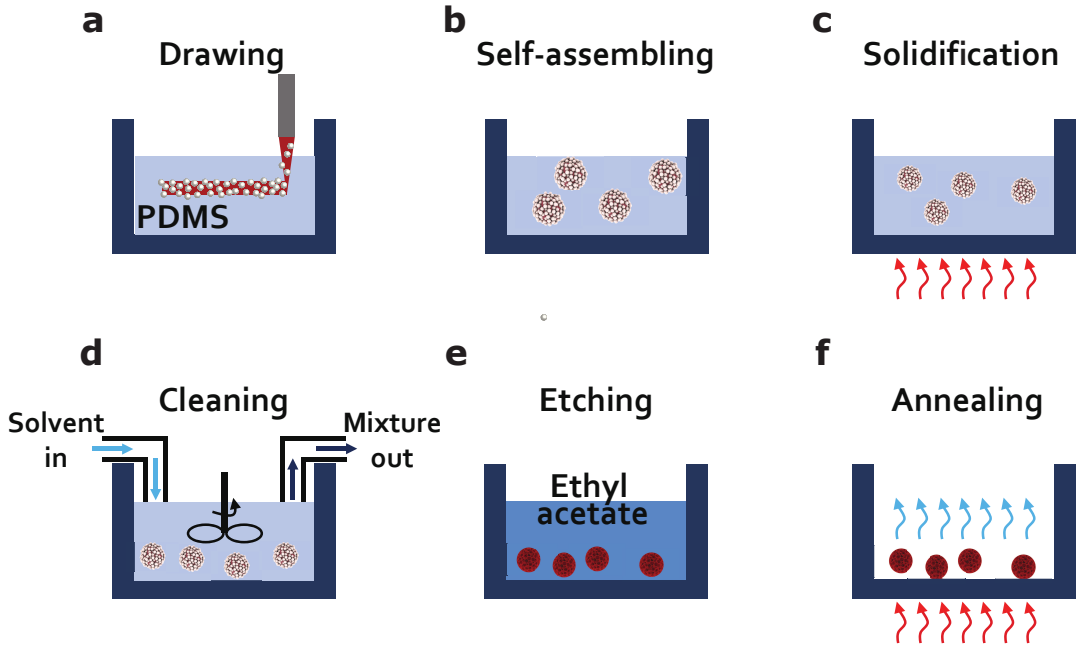

Figure 4.8: **Schematic diagram shows fabrication process of porous microspheres.** a) A sharp tip containing doped polymer solution with immiscible PS beads is immersed in PDMS solution. The tip is dragged in PDMS. b) The line spontaneously splits in to spherical droplets of solution c) The PDMS is heated and the spheres solidify with the PS spheres d) The PDMS is removed by washing in ethyl acetate e) The spheres are submerged in ethyl acetate to remove the PDMS entirely as well as the PS beads f) The ethyl acetate is allowed to evaporate and the porous spheres are annealed.

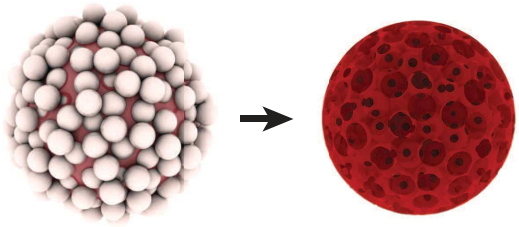

Figure 4.9: **Sketch of the direct and inverse structure.** On the left is an spherical matrix of disordered monodisperse polymer spheres infiltrated with doped polymer (red). On the right is the resulting spherical inverse photonic glass, once the polymer beads are etched.

A self-assembled spherical random laser is obtained using the fabrication methods employed for the formation of WGM lasers detailed in chapter 3. In this case we start from a solution containing the doped biocompatible polymer mixed with polystyrene (PS) beads in suspension. Similarly to previously reported, the solution is aspirated into a pipette. A micropipette tip immersed in PDMS draws the solution and the surface tension leads to the separation and formation of spherical droplets. The microspheres of biocompatible polymer and PS are formed as exemplified by the 3D rendered image in Figure 4.9. Similar to the procedure described previously, the water is evaporated from the solution by placing it on a hot plate at $T < 70^oC$ well below the glass transition for PS ($T \approx 100^oC$) [194].

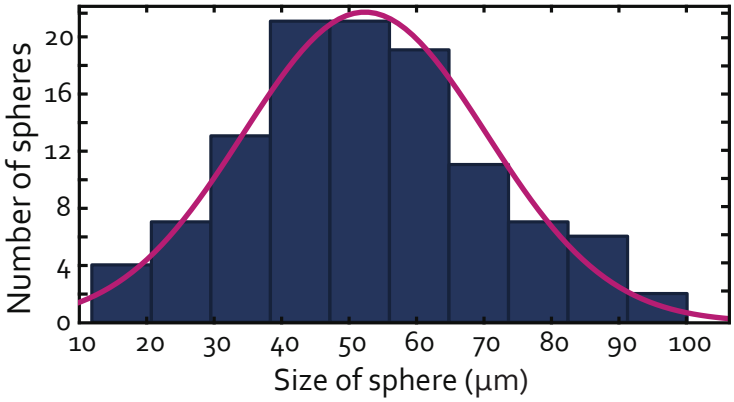

Figure 4.10: **Size distribution histogram of 111 PVA porous spheres.** The histogram is fitted with a normal distribution which is plotted in purple. The mean of the distribution is $D_{mean} \approx 53.9\,\mu m$

When the hot plate is placed at too high temperature a deformation of the spherical voids is observed. The solvent ethyl acetate is used to wash the PDMS and dissolve the PS beads, toluene had been used previously for inverse photonic glass slabs, however ethyl acetate is a less harmful solvent and dissolves both PDMS and PS, with similar results for

both compounds when compared to toluene [169, 195]. The washing process removes the PDMS and the PS spheres. Subsequently the porous spheres are annealed on a hot plate. The resulting structure is depicted on the right hand side of Figure 4.9.

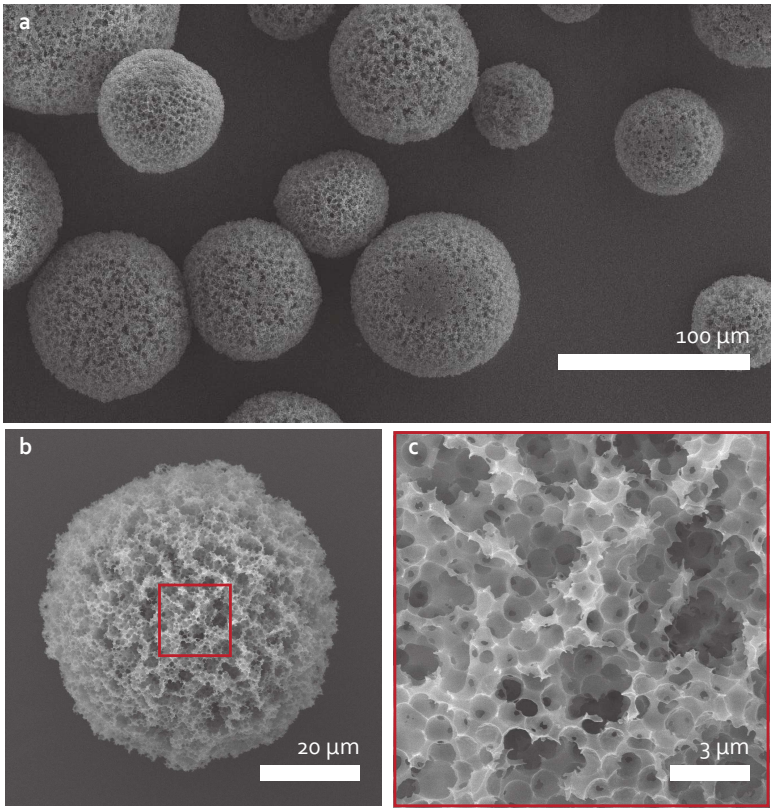

Figure 4.11: **A scanning electron microscopy image of PVA porous spheres.** The samples have been coated with a thin layer of gold to reduce charging and improve imaging qualities. a) Overview of many spherical particles, highlighting the homogeneity of the spherical shape and internal structure. b) A single sphere of $D \approx 50\,\mu m$ showing the porous nature of the structure. c) Shows a zoom in of the red square in figure b) highlighting the disordered nature of the structure, showing the small holes originating from touching.

Initial studies were conducted with PVA. Many spheres can be obtained in one sitting. There is however a lack of control of the sizes of the individual spheres. To evaluate the distribution of spheres obtained, over 100 arbitrary spheres diameters are measured in SEM configuration. The resulting distribution is plotted in Figure 4.10, which is quite similar to that obtained for BSA WGM shown in chapter 3. The size varies from $10\,\mu m - 100\,\mu m$ and the histogram arising follows a normal distribution, fitted to the figure in purple, with a mean value of $D_{mean} \approx 53.9\,\mu m$ and a standard deviation of $\sigma_{fit} = 20.5\,\mu m$. As future work the inkjet printer will be employed to obtain random lasers. Initially experiments are promising showing that we can indeed print many random lasers of similar sizes.

In Figures 4.11a-c are a few examples of the porous random lasers obtained out of PVA. An overview of the porous spheres formed is found in Figure 4.11a showing the homogeneity of the spheres, both in terms of their spherical shape, as well as their porous nature. In Figure 4.11b is a single porous laser with $D \approx 50\,\mu m$; the disordered nature is very obvious and further evidenced by a zoom image of the red square, in Figure 4.11c.

4.3.2 Characterisation of the lasing from spherical random lasers

In this section the lasing output of RhB doped PVA porous spheres will be characterised. A typical lasing plot from a porous microsphere $D \approx 90\,\mu m$ can be seen in Figure 4.12a and b. In the top right corner of Figure 4.12b is an optical image of the measured porous sphere. The roughness due to the nanostructuring of PVA is evident. At low excitation power the spectral shape is due to fluorescence of RhB. The fluorescence is broad with FWHM$\sim 35\,nm$ as seen in Figure 4.12b in the lightest shade of pink. Stimulated emission of the dye narrows the emission with increasing power and the minimum FWHM$\sim 5\,nm$. The narrowing is seen in dark red dots in Figure 4.12a, while the evolution of the peak intensity as a function of power is observed in the same figure in dark blue. The threshold of this particular disordered microsphere is $P_{thres} \sim 50\,\mu J/mm^2$, comparable to the silk slab of similar geometries discussed previously.

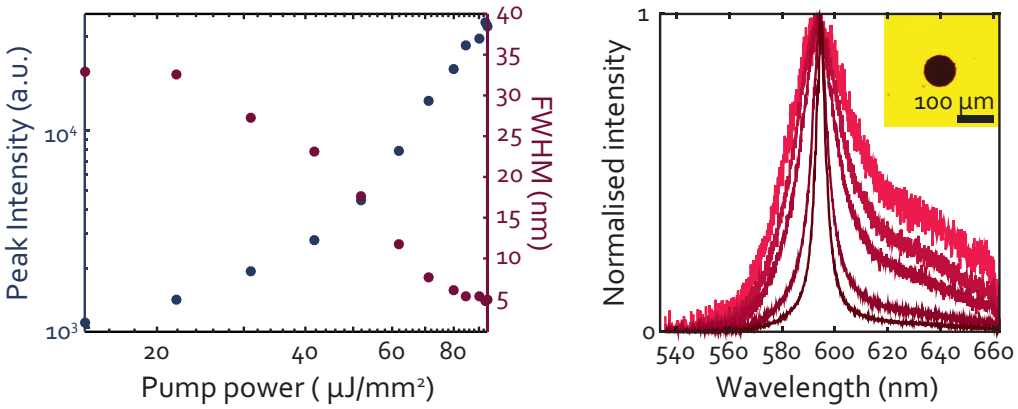

Figure 4.12: **Lasing from a RhB doped PVA porous sphere of** $D \approx 90\,\mu m$. a) Typical lasing plot, in Purple is the evolution of the FWHM with pump power while in dark blue is the evolution of the peak intensity. At low power the FWHM is broad, and the intensity low at threshold $P_{thres} \sim 50\,\mu J/mm^2$ the peak intensity increases abruptly and the FWHM narrows. The narrowing of the emission is seen in the normalised spectral plot in b).

4.3.3 BSA microsphere random lasers

PVA random lasers exhibit a good morphology and low threshold lasing. However, when in contact with water the spheres swell and almost instantaneously lose the ability to lase. For the application we propose, in body sensing, the PVA random lasers do not meet the requirements. Therefore, a different material is necessary. Previous results for BSA-doped WGM laser were very promising showing a stable operation in aqueous media and cell culture media even after several weeks. Porous BSA spheres were made using the fabrication procedure described above. An example of a sphere obtained with BSA is depicted in the SEM image in Figure 4.13a, a close up of the internal structure is illustrated in Figure 4.13b. The structure appears to be disordered, however the packing fraction is visibly lower than that obtained for PVA spheres and the walls of BSA thicker. This is accredited to the dynamic properties of BSA, since as a hydrated protein it has the ability to undergo changes in its conformation [196]. Specifically, the surfactants present on the PS beads to stabilise the suspension, are thought to interact with the BSA causing it to form hydrophobic aggregates [197]. Further tweaking is required to obtain optimised nanostructuring, nevertheless lasing properties are observed. However, lasing in water is difficult to obtain. Lasing was observed only for large particles in water. For a BSA spherical random laser of $D \sim 500\,\mu m$ a threshold of $P_{th} \sim 600\,\mu J/mm^2$ was obtained, a few times larger than the threshold obtain for a silk random laser reported in Figure 4.7. The smaller BSA spheres measured did not lase with the laser energy available, therefore, an alternative material will be exploited.

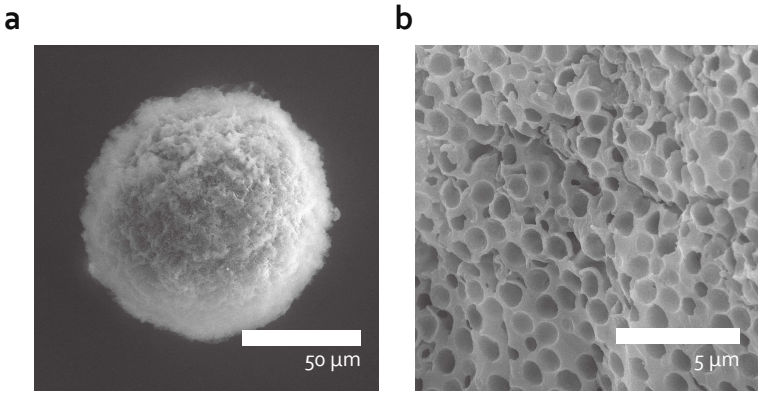

Figure 4.13: **BSA Microsphere random laser.** a) A scanning electron microscopy image of a BSA porous sphere of $D \approx 100\,\mu m$

4.3.4 Silica microsphere random lasers

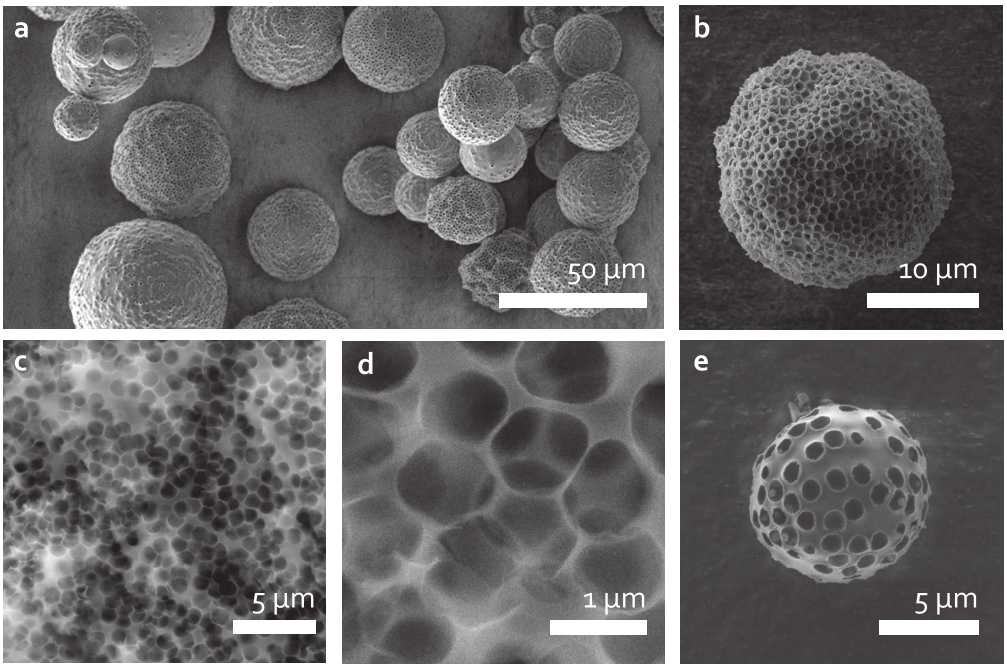

Figure 4.14: **Scanning electron images of silica microsphere random lasers**. a) Overview of a collection of silica microspheres of different sizes. b) Example of a $D \sim 20\,\mu m$ silica random laser. c) The internal structure of a silica random laser. d) A close up of the interconnected voids, highlighting the 3D disorder. e) A $D \sim 8\,\mu m$ silica microsphere. All particles are imaged at low kV and in absence of any conductive coating.

Amorphous silica is a biocompatible material and has been used extensively for diagnosis and drug delivery [198]. Amorphous silica can be obtained through the hydration of tetraethyl orthosilicate (TEOS). Dilute hydrochloric acid (HCl) is added and serves as a catalyst, increasing the rate of reaction. Initially the compounds do not mix and stirring at room temperature is required. Once the solution is homogeneous, dye is added. The remainder of the procedure is similar to that of PVA or BSA, where the mixture is drawn in PDMS and heated to evaporate the water and solidify the microspheres. Silica requires a longer washing process in ethyl acetate with solvent replacement required and typically lasts 4 days to remove all the PS beads. The resulting microspheres are depicted in Figures 4.14a-e. The surface structure varies from bead to bead within the same batch, varying from very little voids on the surface and to structures similar to Figure 4.11b. However, observations of cracked microspheres as well as absence of WGMs lead us to believe that the inside of the particles is made up of disordered voids. The packing fraction for silica

porous beads is estimated from SEM images to vary between $f = 0.4-0.5$ where according to Figure 1.11 from the introductory chapter, the transport mean free path is not expected to vary much.

In order to ascertain and confirm that the silica random lasers could preserve their lasing abilities in biological environments, we have submerged the particles in water and measured the spectra as a function of pump energy. Initially the prepared silica random lasers are hydrophobic and are buoyant in water. To promote hydrophilicity the silica particles were plasma etched for 30s in an oxygen environment. This process is expected to deteriorate the dye and therefore was as short as possible. Compared to a silica particle of a similar size sphere the threshold is almost 50% larger increasing from $P = 90\,\mu J/mm^2$ to $P = 139\,\mu J/mm^2$ after plasma etching.

In Figure 4.15 is the lasing curve of a single silica particle of diameter $D \sim 95\,\mu m$ in air (full circles) and submerged in water (open circles). The threshold of this particle increases from $P = 139\,\mu J/mm^2$ in air to $P = 199\,\mu J/mm^2$ in water, which corresponds to roughly 40% increase of the threshold.

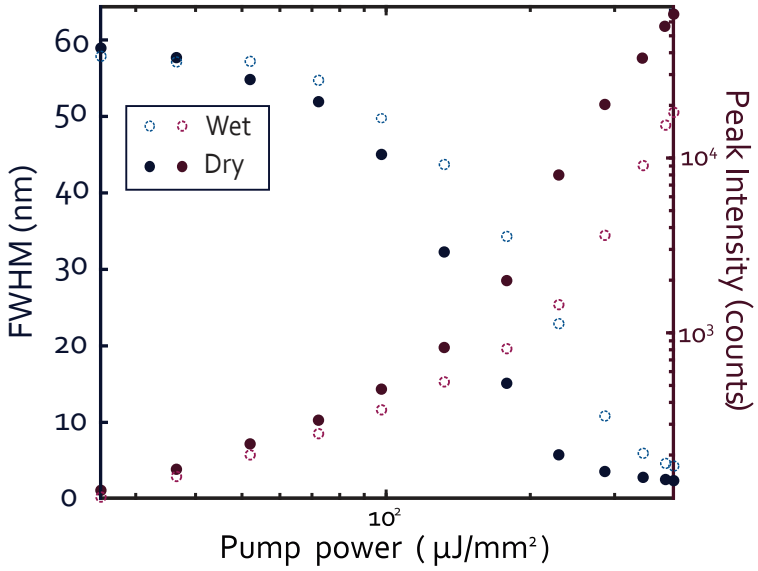

Figure 4.15: **Experimental validation of the silica spherical random lasers in water.** Lasing action for RhB-doped silica random laser in air (blue and purple full circles) and in water (light blue and pink open circles). The blue open and full circles are the FWHM plotted versus pump power, while the purple and pink circles are the peak intensity. When the random laser is immersed in water the lasing threshold is shifted toward larger values (≈40% increase).

4.3.5 Size dependence random lasing studies

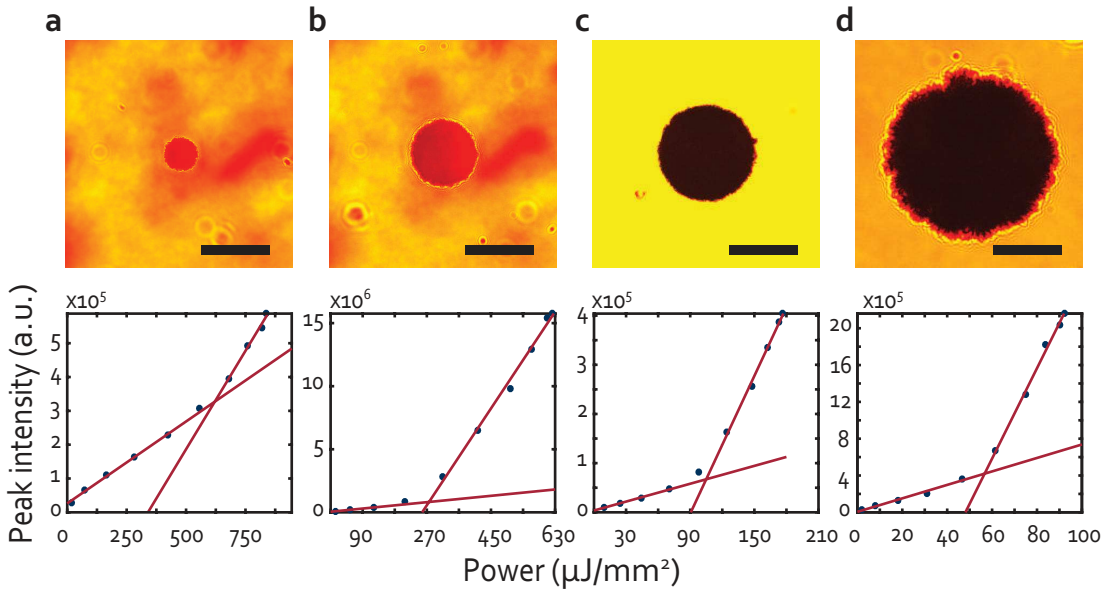

Figure 4.16: **Threshold fits for different sizes of PVA microsphere random lasers.** a), b), c) and d) Present optical image of a microsphere of $D_a \sim 30\,\mu m$, $D_b \sim 50\,\mu m$, $D_C \sim 90\,\mu m$ and $D_d \sim 160\,\mu m$ and below the corresponding fitted threshold, respectively.

To understand the practical limitations of our particles, in the following section we will study how the threshold of the spherical random lasers vary with the dimensions of the particles. As discussed previously due to the multiple scattering in a random laser there is a certain particle size below which the losses outweigh the gain available, called the critical volume or critical length. Using a solution of the radiative transfer equation (RTE) for a spherical random laser, discussed in equation 1.15, the critical diameter D_{cr} can be calculated. For sample parameters $\ell_g \sim 5\,\mu m$ and $\ell_t \sim 4\,\mu m$, the critical diameter for a spherical configuration is $D_{cr} \sim 4\,\mu m$ and $D_{cr} \sim 7\,\mu m$ in water.

To study the size dependence characteristics of the micro random lasers we have evaluated the threshold of 40 spheres of different sizes. The sizes where estimated optically, and the excitation was fulfilled with a collimated beam from an objective. The spot size was regulated by changing the objective, where the beams had $\text{FWHM}_{X10} \sim 165\,\mu m$ and $\text{FWHM}_{X20} \sim 80\,\mu m$ for the X10 and X20 respectively. The spectra was collected from the same objective and was evaluated as a function of power for each porous sphere. The power was calculated from the integrated energy for the spheres diameter approximating the beam profile to a Gaussian of the widths described above. In Figure 4.16 a, b, c and

d are four examples of the fit for different sizes of spheres, $D_a \sim 30\,\mu m$, $D_b \sim 50\,\mu m$, $D_c \sim 90\,\mu m$ and $D_d \sim 160\,\mu m$ respectively, where a and b were measured with the X20 objective and c and d with the X10.

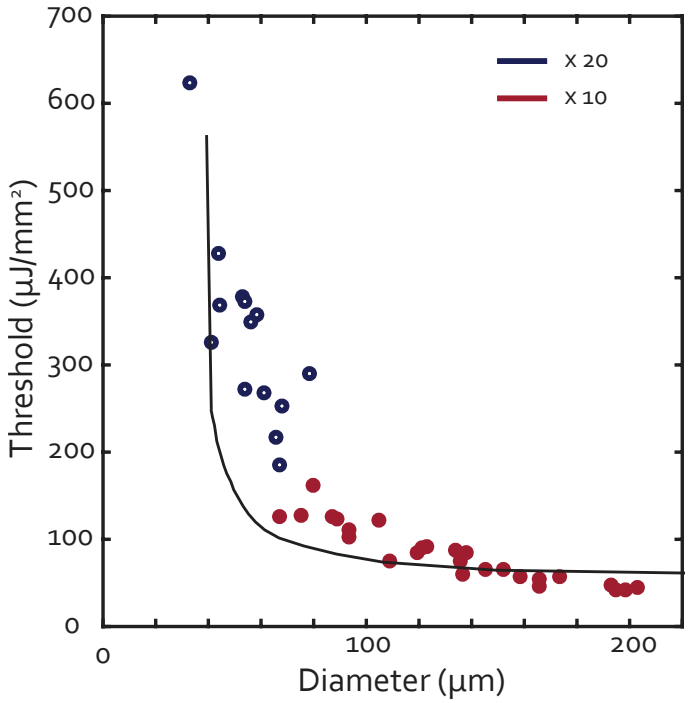

Figure 4.17: **Size dependent random laser threshold.** In red is the threshold of the spheres of sizes between 80 - 200 μm measured with the X10 objective. In blue is the spherical random lasers measured with the X20 objective. The black line depicts the threshold as a function of size using the diffusion approximation.

The energy fluctuation of the laser pulse to pulse is $> 5\%$ measured with an energy meter over a span of 1000 pulses, therefore the error bars are too small to display in Figure 4.16. The corresponding optical images for each of the microspheres is seen in the top half of Figure 4.16, the scale bar is $50\,\mu m$ for all images. Below the optical images is the plot of the total energy in function of peak intensity for each of the respective spheres in blue. This gives rise to two differing portions of data which each can be fitted linearly. The threshold is extracted from the intersection as seen in bottom half of Figure 4.16, similarly to the threshold estimation for the WGM lasers. The threshold of the microspheres expressed as an energy density decreases with increasing diameter of the sphere from a-d. The full trend can be seen in Figure 4.17. Instead at large diameters the threshold is approximately unchanged with size. As discussed previously, this is accredited to the fact that the pump is completely absorbed in the first few 10s of μm and is similar to measurements in bulk. When the

particle is smaller than the excited volume in bulk the threshold increases. A larger photon flux compensates for the reduced gain, leading to an increase of the particles' threshold. Theoretically the smallest lasing particle would be around $D \sim 7\,\mu m$. However, given the limited energy available, experimentally, the smallest lasing particle is $D_{min} = 30\,\mu m$.

Given the change in energy density with each objective a border or a narrower Gaussian distribution, there is a mismatch between the thresholds of particles of similar sizes excited with different objectives. This effect is heightened by the fact that the transition between the X10 and the X20 occurs when the threshold is increasing rapidly with decreasing particle size as evidence in Figure 4.17. For the same particle the threshold is 30% lower for the X10 than with the X20. However, this does not effect the trend or the study of the lasing properties as a function of size as the intrinsic variations from particle to particle are of the same order of magnitude.

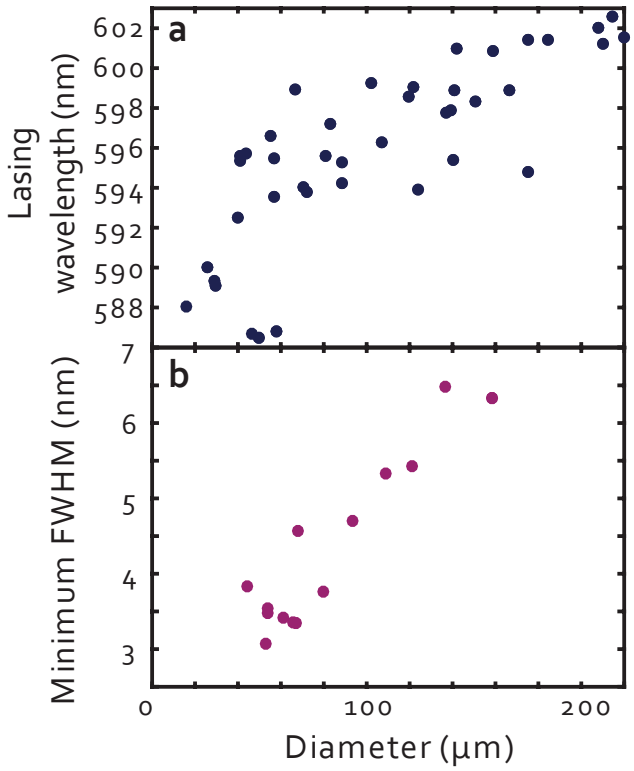

Figure 4.18: **Experimental variation of the lasing wavelength and the FWHM as a function of size**. a) The lasing wavelength as a function of size increases with increasing random laser diameter. b) The minimum FWHM is smaller for smaller particles varying from 3 nm to 6.5 nm.

We evaluated other spectra properties as a function of size, namely the peak wavelength plotted and the minimum $FWHM$ observed. The peak wavelength dependence λ_{lasing} is

illustrated in Figure 4.17b. As the random laser increases in diameter a shift in the peak wavelength is observed, from $\lambda_{lasing} = 588.5\,nm$ for $D = 30\,\mu m$ to $\lambda_{lasing} = 601.2\,nm$ for a particle $D = 198\,\mu m$. The red shift is accredited to the reabsorption of the lasing emission by the dye. The likelihood of reabsorption is increased for larger diffusion path travelled and translates to a increase in the wavelength of the emission. This occurs because there is a overlap between the fluorescence/lasing and the absorption spectra of the dye. To discredited any power dependent effects on the emission wavelength four different sized random lasers were measured. The power dependence of the peak emission for four different sized random lasers was investigated in Figure 4.19. The wavelength dependence is present even below threshold and no significant variation of the peak wavelength is observed at increasing powers.

The FWHM is evaluated for particles which are above threshold and where the spectra is independent of the power. In other words the FWHM plateaus, effect observed in Figure 4.12. Other spheres were not considered for this study. Reabsorption of the emission increases the FWHM of the emission as illustrated in Figure 4.17c. An increase of the minimum FWHM with diameter is observed with the smallest narrowing of FWHM $= 3\,nm$ for a size of $D \sim 50\,\mu m$ noted. The broadest FWHM $= 6.5\,nm$ for a particle of $D \sim 135\,\mu m$.

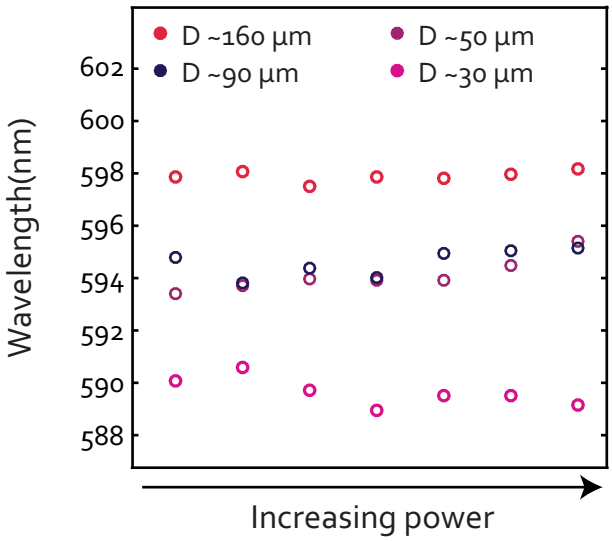

Figure 4.19: **Peak wavelength variation as a function of pump power for different sized random lasers**. The peak wavelength is fairly constant at increasing power, but is larger for larger particles.

4.4 Polysaccharide random lasing from foams

In the previous section we have shown how random lasers can be made with nanostructured biomaterials were maximal scattering is desired. Ministration of random lasers with the ability to operate in water opens new doors for body sensing. Here we present a different fabrication approach and a completely different morphology, larger porous. By using a larger system with larger pores there is the possibility of growing cells inside a random laser rather than placing the lasers inside the cells.

4.4.1 Fabrication of polysaccharide foams

Foams by definition consist of spherical or elongated pores, have isotropic properties and small filling fraction. Freeze casting, an ice templating technique, is a widely know technique and is described in detail in the following reference: [199]. Freeze casting has gained popularity to obtain foams made from biomaterials, due to the control over the material's porosity, including size, directionality and overall geometry of the pores. Moreover, it is an easy fabrication route based on biocompatible solvents, such as water [199].

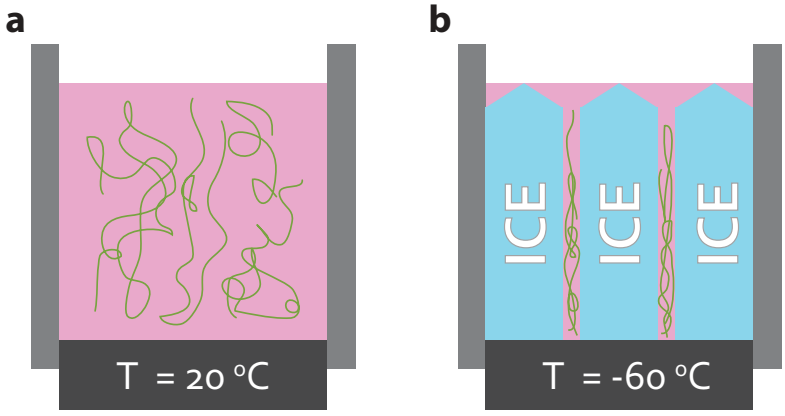

Figure 4.20: **Schematic of freeze casting of polymers.** Freeze casting is a procedure based on oriented growth of ice crystals and can be applied to the elaboration of control macroporous materials a) A solution of 4wt% polysaccharide (green chains) is placed in the PTFE mold. b) The crystallisation of water generates a phase segregation, which leads to the formation of polysaccharide rich domains confined by vertical ice columns.

The unidirectional freeze casting of foams was conducted by Sarah Christoph and Francisco Fernandes in UPMC (Paris) using a home-built setup. In a typical experiment a few mL of polysaccharide solution at 4%wt with 0.5% of laser dye typically Rh6G or RhB is used. A mould typically made of polytetrafluorethylene, known as PTFE, is place on a sealed copper

plate in contact with a nitrogen bath. The top of the mould is open to air, allowing for a temperature gradient [200]. A dedicated heating element controls the temperature of the solution, when the solution is lower than the solidification temperature a freezing front is formed and travels upwards. Ice crystals grow with lamellar microstructure, after the freezing the sample is placed at -20^oC before freeze drying. Ice sublimation, removal of ice, was conducted in a freeze dryer and left to proceed for 24h. The typical structures obtained are seen in Figure 4.21a-d, the optical image in Figure 4.21a and the corresponding SEM seen in Figure 4.21b highlight the macroporous nature of the foams. The pore size are anisotropic. The average distance length of the pore are estimated to be $\sim 90\,\mu m \pm 6\,\mu m$. While the distance between the walls is estimated to be $\sim 14\,\mu m \pm 0.5\,\mu m$. These estimates are obtained from the mean of 50 pores of a confocal scan such as the one in Figure 4.21b using ImageJ.

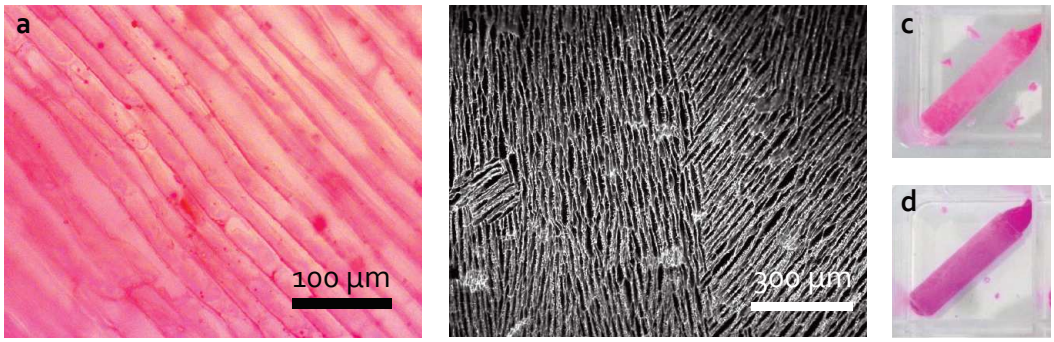

Figure 4.21: Freeze casting of Pectin and Chitosan yields macroporous foams. a) Camera image of a RhB doped pectin foam. b) Confocal scan of a RhB doped pectin foam. c) Rh6G doped foam and d) RhB doped foam.

4.4.2 Transport studies in Foams

The measurement of ℓ_t was performed by comparing 7 undoped pectin foams of different thickness in the range of $350\,\mu m - 1200\,\mu m$. The different thickness were obtained by cutting the foams, in the direction of the ice growth, with a diamond saw, such that thin and even slices were obtained with minimal damage, confirmed by SEM images of the cut surface. The thickness were estimated by optical measurements in cross section and the total transmission measurements were conducted with an integrating sphere. Each foam sample was measured in three different regions. The average of these 3 measurements was fitted with equation 1.10 for each wavelength as shown in Figure 4.21b. Each blue point

in Figure 4.21b. is the transmission of the foam of a certain thickness at $\lambda = 600\,nm$. For an increasing thickness the absorption induces an exponential dependence of T^{-1} on the thickness L. In dark red the result of the fit of the parameters ℓ_a and ℓ_t. The fit is conducted by using a multi-step routine used for determination of the transport mean free path for cellulose paper in chapter 2 :

1. $\ell_t(\lambda)$ and $\ell_a(\lambda)$ were taken to be free parameters of the fit. Approximate value of both for each wavelength were obtained;

2. We fix one of the parameters, for example $\ell_a(\lambda)$, and allow the other, for example $\ell_t(\lambda)$ to be the free parameter of the fit. This is done interchangeably until convergence is achieved (after 4 iterations);

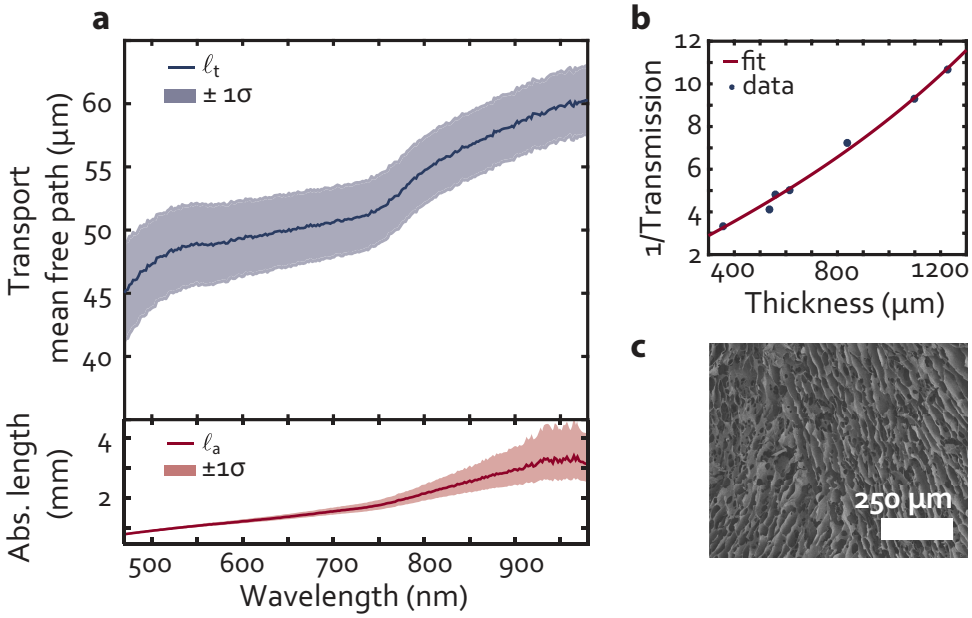

Figure 4.22: Transport mean free path of a Pectin Foam. a) Experimental results obtained from 7 foams. b) Example of the fit for $\lambda = 600\,nm$. In red the fitted curve and in blue circles the samples each of a single thickness. c) an SEM of the structure measured.

From the elliptical shapes of the foams the scattering is expected to be anisotropic, in other words to be stronger in one direction, in the growth direction. To characterise this, white light, (spot diameter $\sim 250\,\mu m$) was sent through a $\sim 1.5\,mm$ thick sample cut in the direction of the ice growth and the transmission profile after the sample was collected on to a camera. The resulting image is plotted in Figure 4.23. The image represents the

intensity profile where in yellow is the larger intensity and in green followed by blue the lower intensities. If the scattering were isotropic the spot would appear round, instead the spot is elliptical. To clarify this the plots directly above and to the right represent the cross-section through the centre of mass in x and in y respectively. The normalised superposition is seen in the top right, where a difference is clearly visible, the width of the Gaussian is 20% smaller in the x direction than in the y.

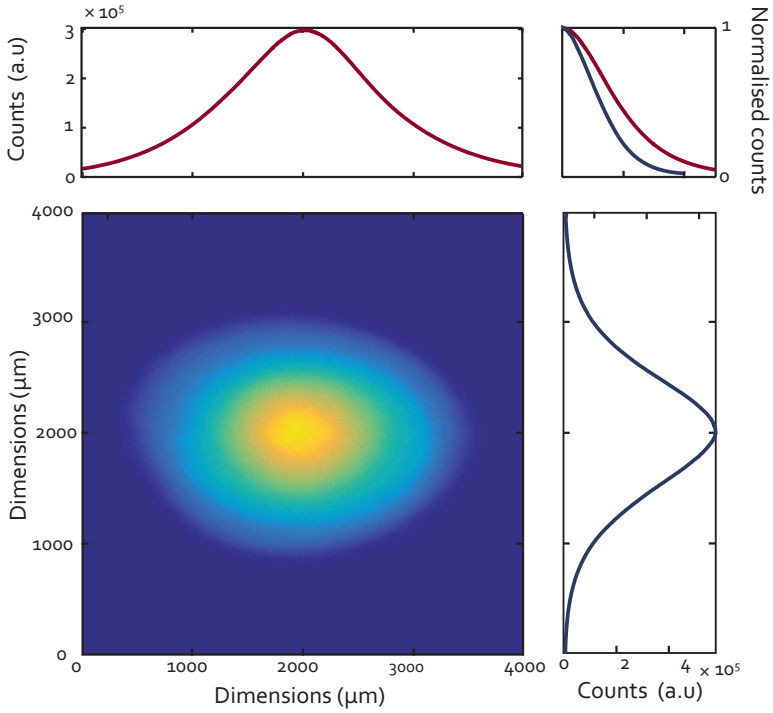

Figure 4.23: **Intensity profile of light through a foam.** The cross section of the intensity profile are plotted for the x-axis in red and for the y-axis in blue. The superimposed cross-section are plotted in the top right corner, highlighting the difference in the transport.

4.4.3 Random lasing from foams

A solution of 4%wt of pectin, chitosan and sodium alginate doped with either Rh6G and RhB were used freeze cast and dried to obtain macroporous foams. The lasing of these foams was evaluated with single pulses of the second harmonic of an Nd:YAG Q-switched pulsed laser, at 532 nm wavelength, 10 Hz repetition rate, and 6 ns pulse duration. The pump diameter is $\approx$ 2 mm, well above the ℓ_t and the critical length estimated to be $L_{cr} \approx 100\,\mu m$ (we are in the diffusive regime of the sample). Due to the anisotropy of the foams this value can be slightly higher. From the spectral evolution of the emission one can extract the relevant lasing parameters such as the lasing threshold. The threshold for a random

lasing foam is defined as the power for which the spectral width reduces to half than its low-pump power value. The lasing curves for pectin foam doped with Rh6G Figure 4.24a and a pectin foam doped with RhB is illustrated in Figure 4.24c. The lasing thresholds are $P_{Rh6G} = 230\,\mu J/mm^2$ for Rh6G and for $P_{RhB} = 150\,\mu J/mm^2$ denoted by the dashed black line. The FWHM in both cases plateaus at around $10\,nm$. The spectra below and above thresholds are plotted in Figure 4.24b and c in dark blue and dashed lines respectively.

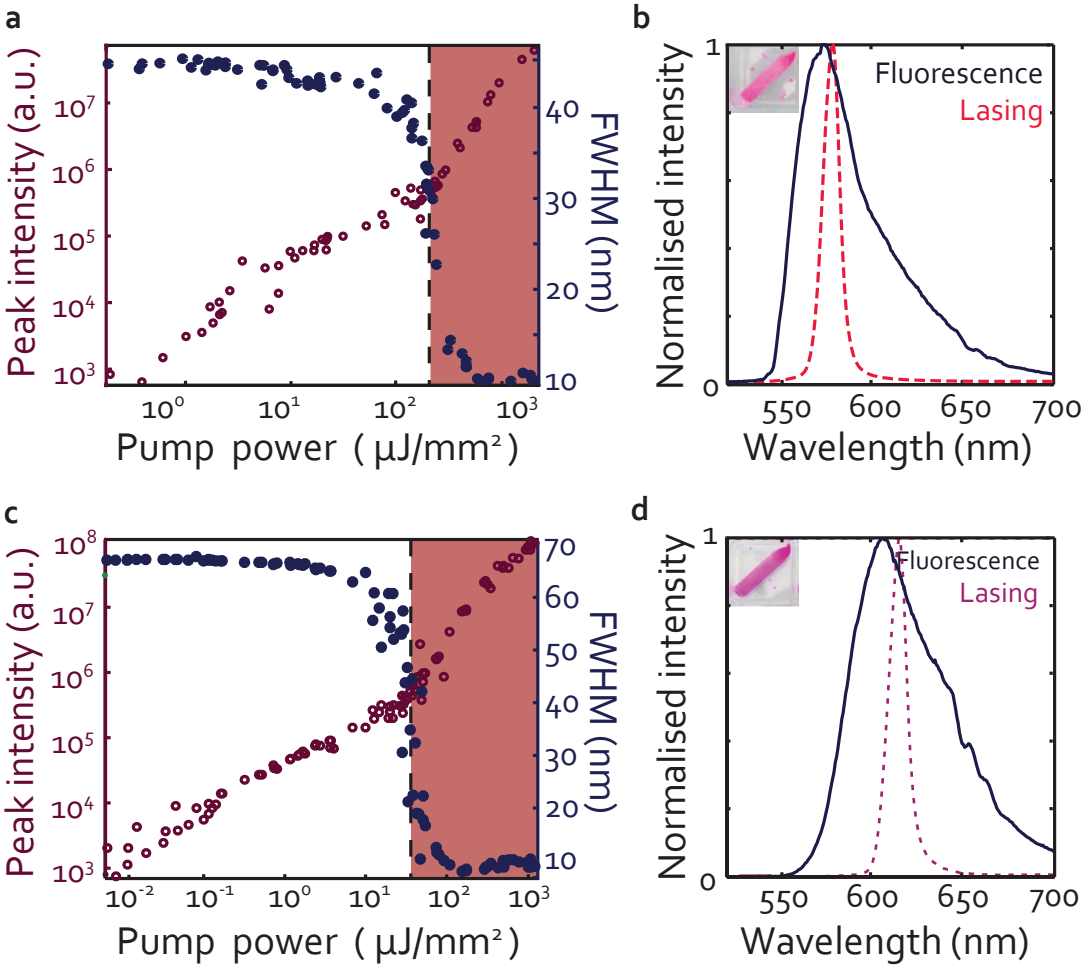

Figure 4.24: **Typical lasing plot for a pectin foam doped with Rh6G and RhB.** a,c) Illustrated are the laser peak intensity as a function of pump power (full blue circles) and evolution of emission linewidth with pump power (empty purple circles). The red rectangles illustrate the lasing region above threshold ($P_{rh6G} = 230\,\mu J/mm^2$ for Rh6G and for $P_{rhB} = 150\,\mu J/mm^2$ for RhB). b,d) Comparison of spectra above threshold and in fluorescence

The fluorescence peaks at $\lambda_{flu} = 575\,nm$ with a FWHM $\sim 43.7\,nm$ for Rh6G doped pectin and at $\lambda_{flu} = 607\,nm$ with a much larger FWHM $\sim 66\,nm$ for RhB doped pectin. The lasing at threshold peaks at $\lambda_{las} = 575\,nm$ for increasing power once the minimum

FWHM is reach the peak wavelength of the lasing is red shifted to $\lambda_{las} = 575\,nm$ and $\lambda_{las} = 617\,nm$ for $P = 2200\ \mu J/mm^2$ for Rh6G and RhB doped pectin respectively, this is due to gain saturation in the active volume, the photons are no longer absorbed by the already excited molecules and therefore a larger probability of reabsorption and a red shift of the emission.

The same morphology was attempted with chitosan, another biocompatible polysaccharide. The lasing plot for RhB doped chitosan is depicted in Figure 4.25a and b. The plot is similar to reported above with a threshold of $P_{rhB} = 100\,\mu J/mm^2$. The spectra below and above threshold is plotted in Figure 4.25b in dark blue and dashed purple lines respectively. Here the fluorescence peaks at $\lambda_{flu} = 595\,nm$ with a FWHM $\sim 64\,nm$.

The third attempt with sodium alginate was unsuccessful despite the satisfactory foam morphology and very pink appearance of the rhodamine doped samples. Both the RhB and Rh6G doped foams presented very broad fluorescence spectra of $\sim 65\,nm$ for Rh6G doping and $\sim 80\,nm$ for RhB doping and spectral narrowing was not observed, contrary to this the spectral broadness increased with pump power. When a bulk doped sodium alginate was pumped the fluorescence spectra was much narrower $\sim 40\,nm$. The interaction of the dye with sodium alginate is not fully understood, furthermore we cannot hypothesis why the dye degrades after the freeze drying process when in contact with sodium alginate.

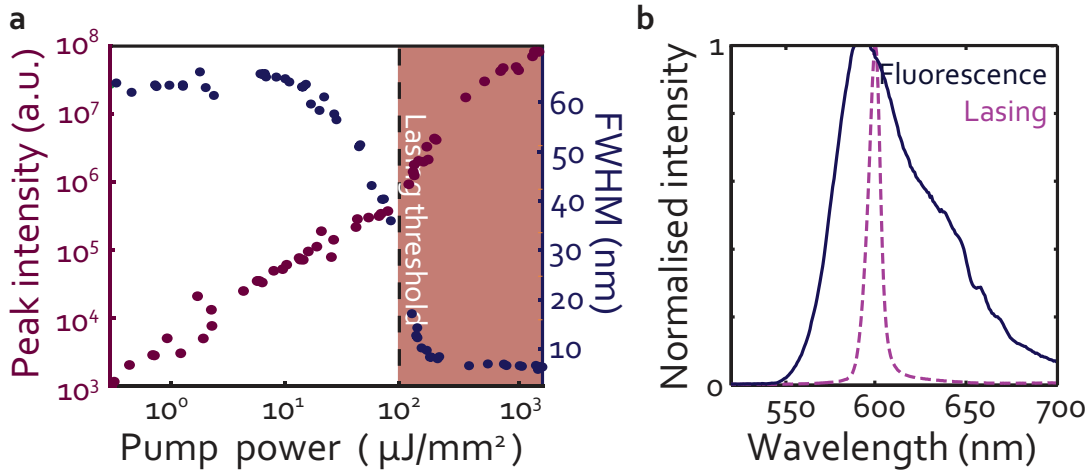

Figure 4.25: **Typical lasing plot of RhB doped Chitosan foam** a) Illustrated are the laser peak intensity as a function of pump power (full blue circles) and evolution of emission linewidth with pump power (purple circles). The red rectangles illustrate the lasing region above threshold ($P_{rhb} = 90\,\mu J/mm^2$). b) Comparison of spectra above threshold and in fluorescence at 2200 $\mu J/mm^2$ and 0.7 $\mu J/mm^2$ respectively.

4.4.3.1 Lasing in water and silica coating

For potential applications for biosensing it is essential that the foams maintain their lasing function with minimal degradation while in liquid media. The foams morphology, large pores with low filling fraction makes them easy and quick to dissolve in water. To overcome this limitation, the RhB doped pectin foams were coated with silica, to improve water stability. Although this prevented the dissolution of pectin the dye leaching was substantial ailed with the decrease of refractive index contrast, lasing could not be achieved at the pump powers available. For dye protection a dye was grafted on Pectin a derivative of rhodamine, Rhodamine B isothiocyanate (RITC). The chemical structure of the derivative is designed so that a functional group allows it to be covalently attached to many organic compounds such as BSA [201]. However, the covalent attachment affected the dyes gain and lasing was again not possible to achieve.

4.5 Summary of materials and morphologies studied for lasing

In this section we summarise all the materials and dyes worked with in the various geometries of which a few of which have been discussed in detail in previous sections and chapters. A multitude of different materials were explored ranging from polysaccharides, proteins and polymers.

Photonic glass structures were successfully obtained with Silk detailed in chapter 4, CNCs , Pectin, Chitosan, Glucose and PVA all shown in chapter 2. BSA being a protein was found to form a gel in the presence of PS bead, while Hydroxypropyl cellulose (HPC) was dissolved by toluene, acetone and ethyl acetate such that the beads could not be successfully removed.

Whispering gallery mode microspheres were obtained with Pectin and Silica with Rhodamine Isothiocyanate (RITC), Rhodamine 6G (Rh6G), Rhodamine B (RhB) as gain media. Bovine serum albumin (BSA), PVA and PVP microsphere laser were successfully obtained with RhB and in the case of BSA lasing was also obtained with fluorescein.

Slab random lasers were the first random lasers fabricated using the photonic glass architecture and adding gain to the system. This geometry was accomplished with silk,

pectin and PVA. The fabrication was expanded to spherical microsphere random lasers with silica and PVA, however, it was unsuccesful will silk, BSA and pectin.

Lastly foams, were fabricated with pectin, chitosan and sodium alginate. Sodium alginate yielded a good foam structure, nevertheless it did not lase with either RhB and Rh6G.

Biomaterial	Photonic glass	Dye	WGM	Slab Random laser	Spherical Random laser	Foams
Silk		Rh6G				
		Fluorescein				
CNCs		FITC				
		Fluorescein				
		G-FITC				
HPC Cellulose						
Pectin		RITC				
		Rh6G				
		RhB				
Chitosan		RH6G				
		RhB				
D-Glucose		RhB				
Silica		RhB				
		Rh6G				
		RITC				
		Fluorescein				
BSA		Fluorescein				
		RhB				
PVA		RhB				
PVP		RhB				
Agar						

Table 4.1: **Biomaterials nanostructured and lasing.** This table presents the different materials tested and the dyes used, where G-FITC stands for grafted FITC. The red represents the experiments attempted but unsuccesful, the green represents the succesful experiments and the yellow the experiments which were not attempted.

4.6 Outlook/Conclusion

Here we presented the first biocompatible silk random laser. The fabrication technique used is versatile and the procedure can be tailored not only to different gain molecules, but also different biocompatible materials, including: BSA, pectin, silica amongst others. The doped inverse photonic structure obtained is highly scattering with a transport mean free path of $\ell_t \approx 4-7\,\mu m$. We develop a technique to miniaturise random lasers and study

their lasing properties with varying size. The smallest random laser obtained was a silica laser with $D \sim 28\,\mu m$. Further investigation is required to understand the size dependent lasing output. The spectra obtained is composed of spikes and is not smooth as observed in Figure. However, the resolution does not permit to observe the individual peaks. Further study is required to understand if the peaks are also size dependent. Initial observation suggest that the output is composed of peaks and as the size of the particle increases they begin to smear out and smooth out the spectra.

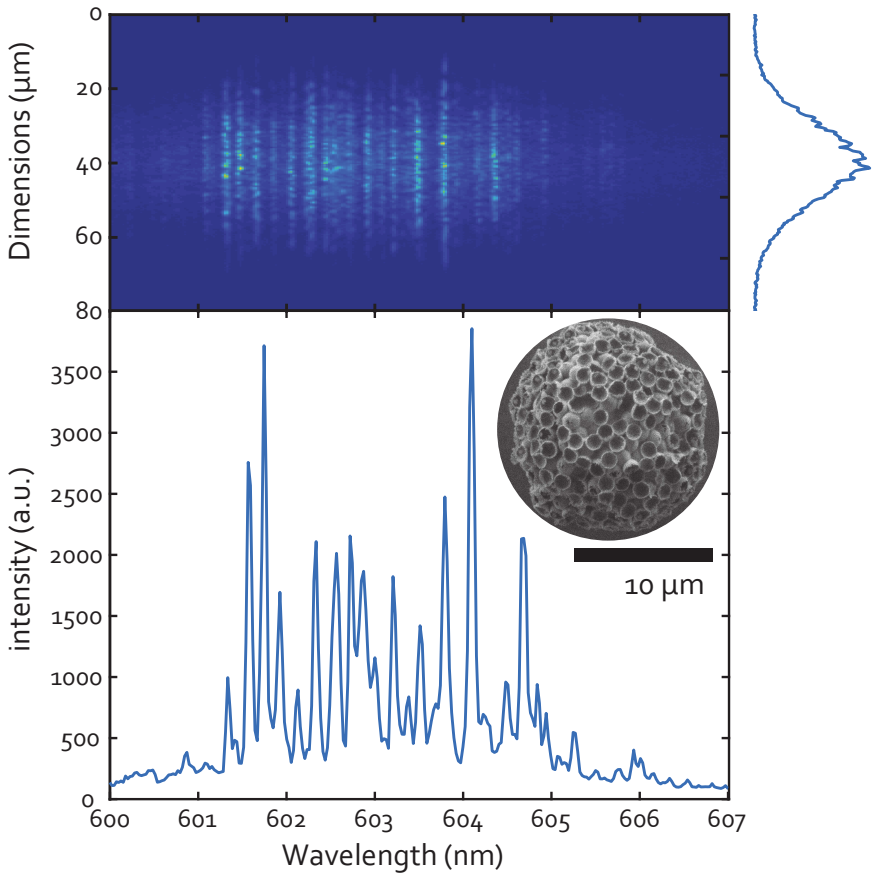

Figure 4.26: **High resolution spectra of a small random laser.** The spectra of a $D \sim 30\mu m$ silica laser is depicted spatially in the top figure. The modes are present on the full extension of the laser as evidenced in the figure on the right which shows the integration of the intensity. The bottom figure depicts the modal output of the particle.

5 Sensing with lasing

Biocompatible lasers are promising for sensing applications. Here we show how a biocompatible random laser can be an efficient pH sensor. Furthermore we investigate the mechanism of a random-lasing-based sensor which shows pH sensitivity exceeding by 2 orders of magnitude that of a conventional fluorescence sensor. We explain the sensing mechanism as related to gain modifications and lasing-threshold nonlinearities. A dispersive diffusive lasing theory matches the experimental results well, and it allows the prediction of the optimal sensing conditions and a maximal sensitivity as large as 200 times that of an identical fluorescence-based sensor. The lack of complex alignment and the high sensitivity make this mechanism promising for future biosensing applications.

5.1 Introduction

Lasing has thus far been largely overlooked as a sensing transducer owing to the geometrical complexity of conventional lasing architecture. Instead, fluorescence-based sensing exploiting spontaneous emission is among the most widespread mechanisms for bio-chemical detection [202, 203]. A chemical interaction typically leads to a change in intensity, spectra or lifetime, giving rise to a sensing signal, in some cases this signal is weak and the spectral change is not very pronounced. Lasing has the potential to outperform fluorescence due to the inherent signal amplification, increased signal to noise dynamics, the narrowed emission and non-linear dynamics [56]. To date several laser based sensors have been shown for interleukin sensing [152], explosives [204] and remote sensing of hazardous chemicals [205].

Biolasers, lasers made of biocompatible materials have the potential to produce new coherent light sources, flexible and compatible for tissue integration. Biolasers hold the potential to harness the amplifying power of stimulated emission for biosensing and cell tracking [56, 78].

Sensing with WGM lasers relies on changes in the resonance of the cavity, accomplished for example by a change in refractive index of the surrounding media or by deforming the cavity itself. The ability to detect small geometrical changes has been used to detect dynamical changes in the interior of cells with liquid WGM lasers [8].

Another sensing strategy is to use the gain molecule as the sensing transducer and the geometry as the amplifier of the molecular response to changes in the chemical environment. While high Q-value cavities lead to low-threshold and high sensitivity readings, their precise geometries can limit their application. For example dynamical living tissue may cause physical changes to the cavity. The system is therefore, unreliable to any real changes in the environment and instead becomes a reporter of geometrical changes. Large deformations can affect the output drastically and may even destroy their lasing abilities. In contrast random lasing occurs in disordered systems with optical gain [9]. The lack of an optical cavity gives this random lasers the resilience against deformation and makes it appealing for implantation in biological media.

Sensing in random lasers has been limited to the detection of changes in the scattering strength by a refractive index change [87, 206] and temperature variation [207] and is on

its own less sensitive than WGM lasers. Instead, we aim to use random lasing sensing in a similar scheme to conventional fluorescence sensing, a targeted sensing via biochemical interaction at the emitting molecule level. In other words a sensing scheme that affects the gain available to the lasing process and in consequence the amplification process.

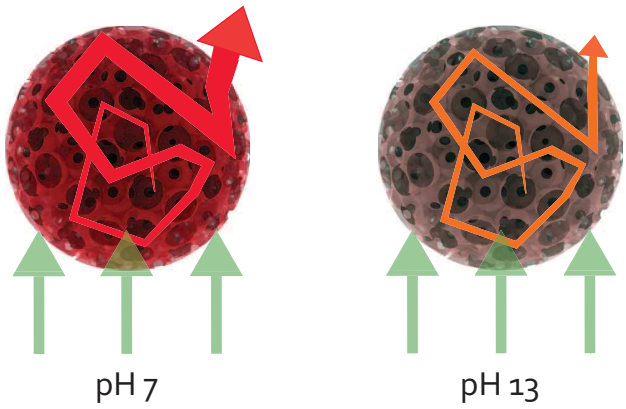

Figure 5.1: **Sensing scheme where by in the presence of large pH the emission is suppressed.** On the left the laser operation at neutral pH is strong, when the pH of the solution is increased beyond pH 13 the lasing is completely suppressed as illustrated by the image on the left.

As proof of concept we explore sensing in the silk random laser introduced in the previous chapter whose gain medium is Rhodamine 6G (Rh6G). The absorption spectra of Rh6G in aqueous solution is affected by dye concentration, pH and temperature [208]. The increase of the pH of the solution with RH6G is known to decrease the fluorescence emission and therefore will also affect the lasing [208]. The sensing scheme proposed is an on-off scheme where at low pH the lasing is on, and at high pH the lasing switches off as schematically demonstrated in Figure 5.1.

5.2 Relevance of pH sensing for biological monitoring

The detection of pH is critical in a wide range of industries including pharmaceutical and biotechnology, food and beverage, agriculture, water and waste water treatment and environmental control. Specifically for biological monitoring, variations of pH, beyond the norm, can be associated with disease. Cell survival is dependent on favourable acid-base balance and regulate their ion channels to maintain the cytosolic pH within a narrow range: 7.1-7.2. In the early stages of solid tumours the extracellular pH can be as low as 6.5 [209].

In contrast the pH environment of chronic wounds such as ulcers is found to be in the range 7.15-8.9. The rates of healing of a wound is also associated to its pH levels. Elevated levels of alkalinity translate to higher recovery time when compared to closer to pH neutral levels [210].

5.3 Experimental random laser pH sensing

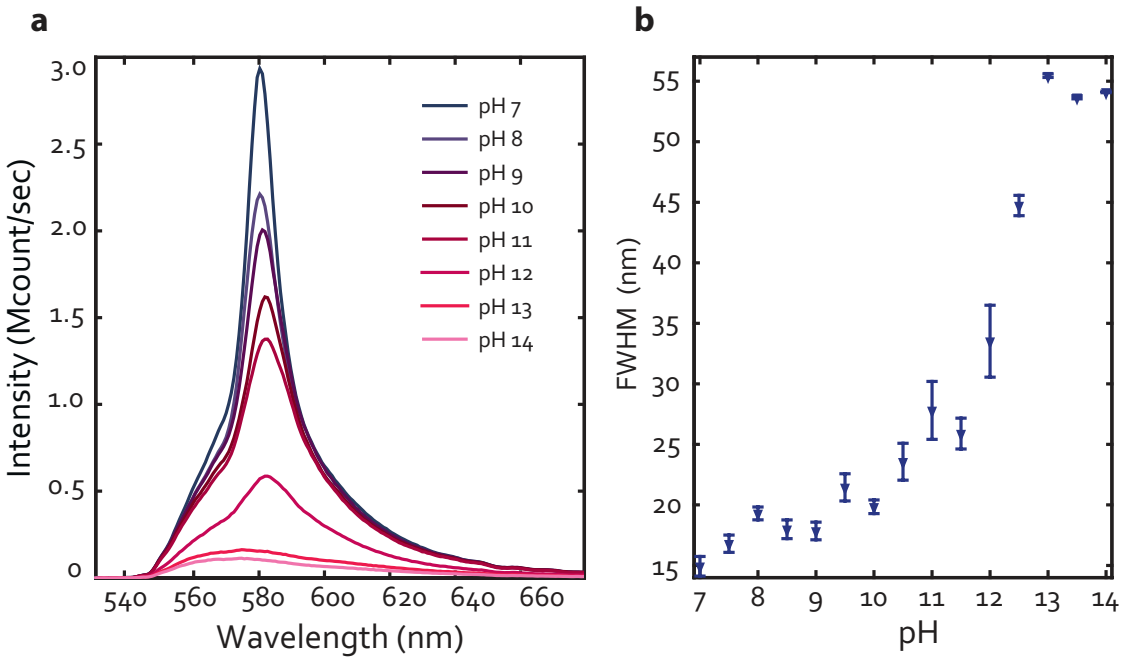

Figure 5.2: **Spectral changes as a function of pH.** a) Average of 10 spectra of silk random laser submerged in solution of different pH and excited at $P = 600\,\mu J/mm^2$. The highest intensity corresponds to the lowest pH. The lasing is subsequently suppressed with increasing pH. The lasing is completely suppressed from pH 12 to pH 13 reverting to the characteristic broad fluorescence spectra. b) Plot of the FWHM of the spectra as a function of increasing pH. The error bars come as a result of the averaging of 10 spectra and is due to both the fluctuation in the pump power as well as the non-linearity of the lasing process.The FWHM changes significantly with pH, at pH 7 it is 10 nm, the FWHM increased slowly with increasing pH reaching 25 nm at pH 10. After which there is an abrupt change from pH 11 - 13.

In the previous chapter we studied the lasing characteristics of an inverse photonic glass made solely of doped silk and showed that it can operate in water, essential for biological sensing. Here we change the pH of the water by increasing the concentration of sodium hydroxide (NaOH) from pH 7 to pH 14. The assumption is that NaOH is completely disso-

ciated in solution. All pH measurements were rectified with a pH strips.

Sensing is experimentally achieved in aqueous media, to resemble biological conditions. The porous structure of the inverse photonic glass and the permeability of silk [18, 114, 211] allow for the molecules to be responsive to chemical changed in the solution. The sample was placed in a custom holder, submerged in solution and excited with a $\lambda_{ex} = 532\,nm$ and $\sim 2\,mm$ diameter spot. The spectral change was evaluated at a fixed power of $P = 600\ \mu J/mm^2$, subsequently changing the pH solution starting at pH 7. At increasing pH the lasing properties of Rh6G are degraded. The spectra changes from pH 7 - 11.5 are small, changing from FWHM ~10 nm - 25 nm. By contrast beyond pH 12 the emission change is significant and the lasing is completely suppressed. There is no lasing and the emission is broad (55 nm), illustrated in Figure 5.2a and b.

The change in the lasing spectra is accredited to a change in the gain molecule in the presence of high pH. Rhodamines have a non-stratified COOH group which can be reversibly deprotonated in the presence of alkaline solutions. The deprotonation is thought to interrupt the π system of the molecule changing among other properties its absorption cross section (σ_{abs}).

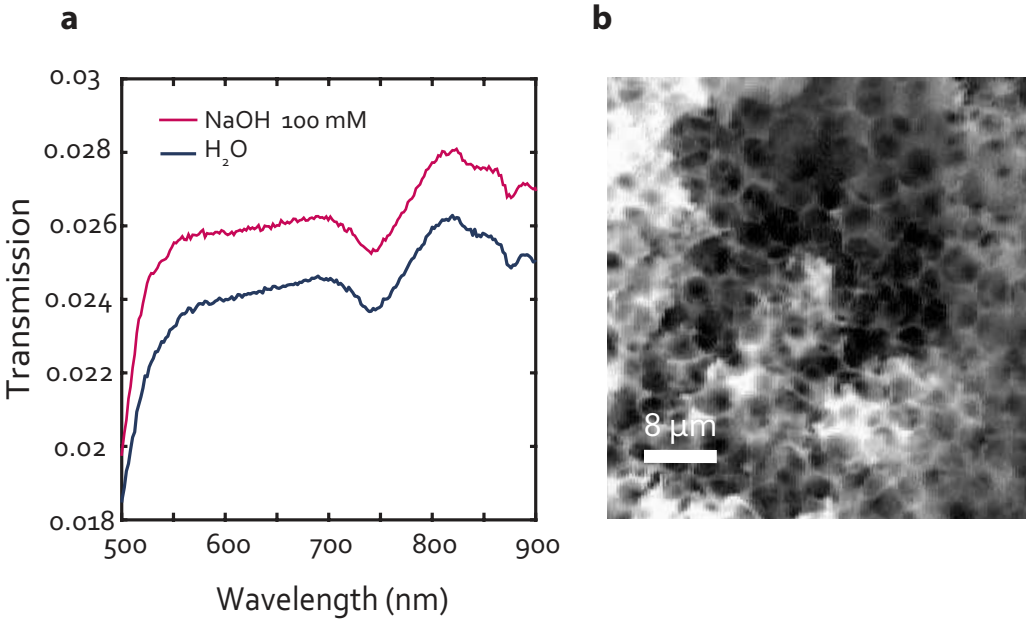

Figure 5.3: **Total transmission studies at neutral and high pH.** a) Transmission variation from neutral pH to high pH (pH = 13) and b) the SEM scan after the submersion in high pH.

To rule out the possibility of a structural or refractive index modification and degradation

of the sensor at high pH, the total transmission of silk inverse photonic glass was evaluated in high pH solution in absence of dye. A silk inverse photonic glass was placed in a neutral and pH 13 solution on top of an integrating sphere. Collimated white light was directed to its surface and the spectrum was recorded, normalised by the spectra of the white light. The transmission spectra profile is maintained upon the addition of NaOH and only a shift in transmission is observed as illustrated in Figure 5.3a , indicating a small decrease of the scattering strength (>10%), when compared to the transmission at neutral pH. The small transport change alone would affect the threshold by not more than a few percent, and is due to the slight swelling of the silk matrix, evidenced in Figure 5.3b. The unfamiliar transmission profile as a function of wavelength presented in Figure 5.3a is due to the absorption peaks of H_2O at $\lambda = 730\ nm$ and $\lambda = 875\ nm$ [212].

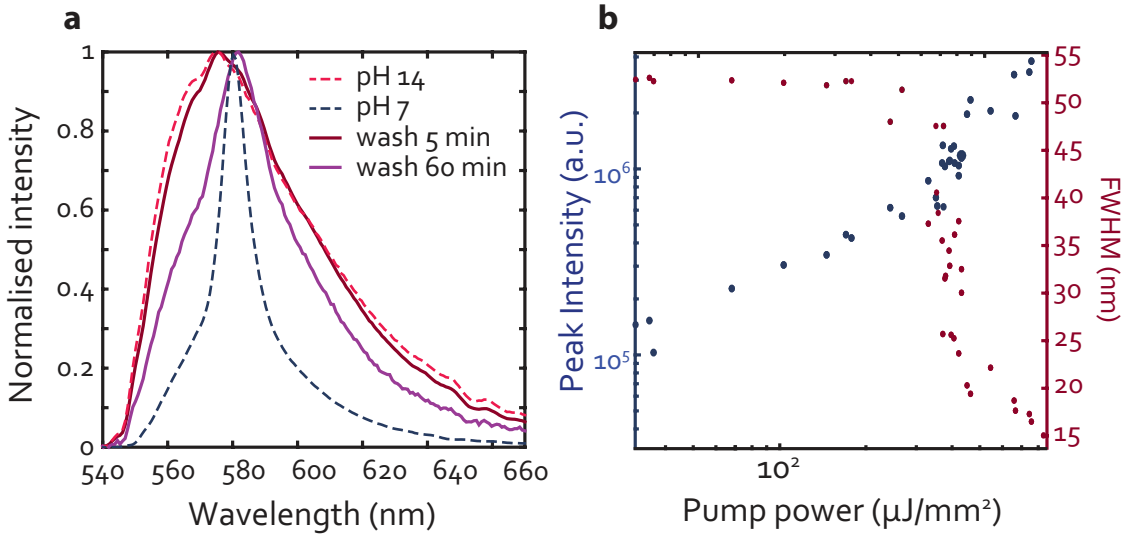

Figure 5.4: **Lasing recovery** a) Compares the spectra at 600 $\mu J/mm^2$ at different stages, in dashed blue line the spectra at pH 7 and in dashed pink is the spectra at pH 14. To show the recovery of the lasing there is a full dark pink line after 5 min of irrigation and in full purple line is the spectra after 60 min of irrigation, illustrating the recovery of the lasing. b) The Full threshold curve, showing the FWHM evolution as a function of power in purple from 54 nm to 15 nm and in blue circles the peak intensity as a function of pump power.

The lasing switches off at large pH. When maximum power is used (1100 $\mu J/mm^2$) no spectral narrowing is observed. The spectra is plotted in Figure 5.4a in the dashed pink line. However, this is a reversible sensor and when the pH is restored to neutral the lasing dynamics are recovered. The random laser is irrigated with deionised water to lower the pH. After 5 min of submergence and irrigation the spectra is almost unaltered as illustrated

in red in the plot in Figure 5.4a. After 60 min instead the spectra plotted in purple in Figure 5.4a obtained after pumping with P =600 $\mu J/mm^2$ is narrower with FWHM $\sim$ 35 nm. Nevertheless, full reversal is not achieved, which can be seen by comparing the results to the original spectra (dashed blue line in Figure 5.4a) This signifies that the lasing threshold has increased, in Figure 5.4b is typical lasing curve as were FWHM and the peak intensity are evaluated as a function of power. From the plot the lasing threshold is determined to be $P_{th} \sim 370\,\mu J/mm^2$ greater than the lasing threshold in water ($P_{th} \sim 140\,\mu J/mm^2$).

5.3.1 Sensing mechanism

Qualitatively, we can understand the lasing suppression as a reduction of the optical amplification which increases the gain length, ℓ_g. As previously discussed ℓ_t is unaffected by pH, whereas ℓ_g is pH sensitive. When the critical lasing size, $L_{cr}\ \alpha\ \sqrt{\ell_t \ell_g}$ required for lasing becomes larger than the sample size, the laser switches off.

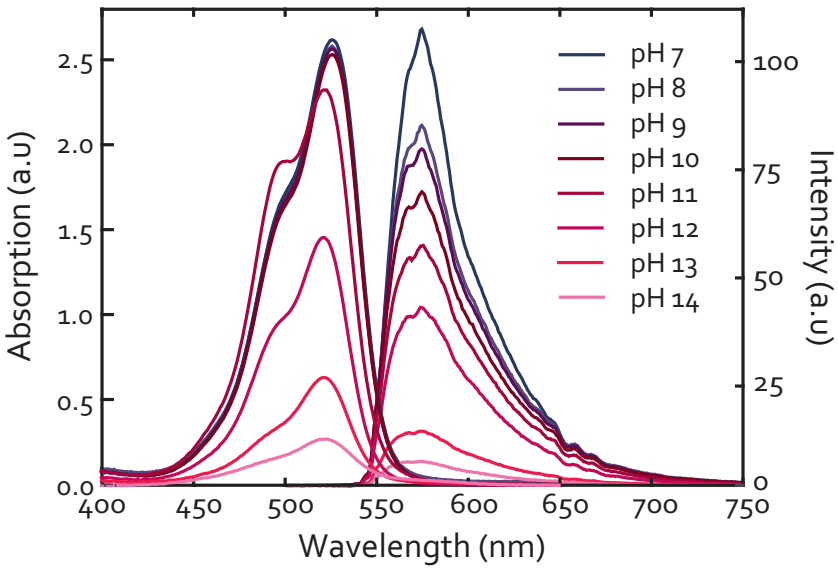

Figure 5.5: **Absorption and emission spectra of Rh6G with varying pH.** Relative absorption spectra on the left as a function of pH and on the right the emission spectra as a function of pH. The trends shows that the emission and absorption decreases with increasing pH of the environment.

To understand the mechanism behind the lasing we will measure and estimate the change observed in fluorescence parameters such as: σ_a, fluorescence emission,Φ and τ. Firstly we evaluate the absorption and emission spectra of Rh6G in a solution with varying pH. The absorption of the Rh6G is evaluated with an absorption spectrometer, which

sweeps over different wavelengths (400 nm - 650 nm). The light is transmitted through a cuvette with solution of 0.05 mM of Rh6G at a given pH. The concentration is optimised to allow for light to be transmitted through the solution as well as prevent the quenching of Rh6G by dimer formation [176, 213]. The incident light is transmitted following Beer-Lambert law expressed in equation(1.8) and gives rise to a parameter called the absorption coefficient. Here, we are interested in the relative absorption between different pH. The absorption spectra as a function of pH is plotted in Figure 5.5 on the left. For pH 7 - pH 10 there is only a slight decrease in the absorption maximum. At pH 11 the absorption maximum shifts to shorter wavelengths with the second absorption peak emerging at 480 nm, followed by a dramatic absorption decrease at from pH 11 to pH 12, which continues until pH 14.

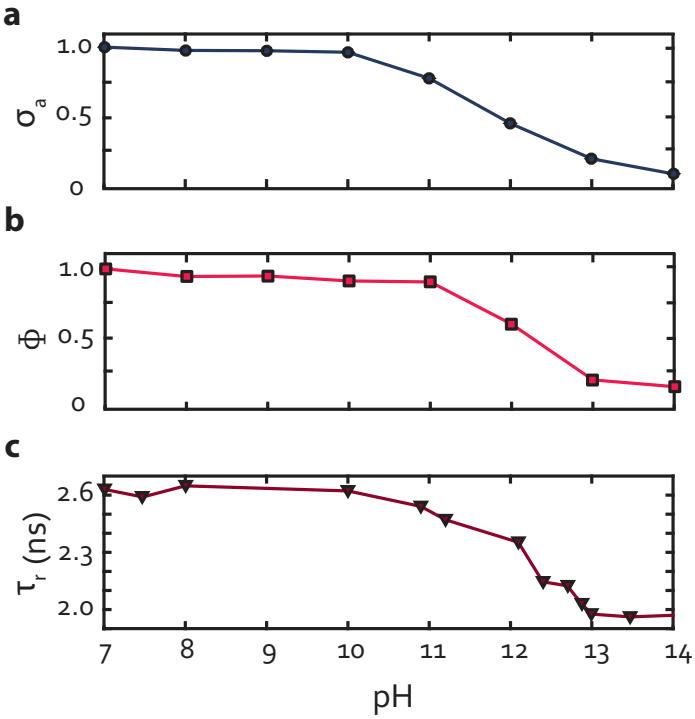

Figure 5.6: **Rhodamine 6G properties as a function of pH**. The relative absorption cross section (σ_a), quantum efficiency (Φ), and excited-state lifetimes (τ) measured as a function of pH. All quantities decrease for pH values larger than $\backsimeq$10.

The absorption spectra at pH 14 is a magnitude less than that at pH 7. These results are an indication of the relative absorption cross section of the molecule in the presence of pH and from the absorption spectra we can deduce the quantity σ_a. It is important to note that the result is in solution, where molecules can form aggregates. It isn't obvious

that this should be the case in a biomaterial matrix. Nevertheless, there is a decrease in emission of the lasing. The relative absorption cross section obtained as a function of pH is plotted in Figure 5.6a. The emission of Rh6G now in a silk matrix is also evaluated, with a fixed wavelength of λ =532 nm at powers well bellow threshold. The resulting spectra as a function of pH is plotted on the right hand side of Figure 5.5. The emission follows the absorption trend and is maximum at pH 7 decreasing progressively as the pH of the solution increases.Although the absorption between pH 7 to pH 10 is almost unchanged the emission spectra decreases significantly in this range and sees a dramatic decrease in the emission intensity between pH 12 and pH 13.

The absorption and emission spectra are used to determine the quantum yield Φ of Rh6G. The result is also determined with the variation of the transmitted laser light (picosecond pulsed excitation $\lambda = 532$ nm, 40 MHz) and fluorescence intensity when recording the light escaping from the silk inverse photonic glass with an integrating sphere. Although the first method relied on the absorption measurements in solution, Φ calculated is consistent for both methods. Given this result, we are confident that the absorption of Rh6G in solution is a good indication of the absorption of the molecule in a silk. The relative Φ at varying pH is plotted in Figure 5.6b.

Another parameter to model the lasing behaviour is the life-time τ of Rh6G in silk. Using fluorescence lifetime spectroscopy by time correlated single-photon counting and using a picosecond pulsed excitation ($\lambda = 532$ nm, 40 MHz) source τ is determined as a function of pH and plotted in Figure 5.6c. τ is constant until pH 10, beyond which it decrease from $\tau_{pH\,10} = 2.6\,ns$ at pH 10 to $\tau_{pH\,13} = 2.0\,ns$ at pH 13 above which is plateaus. With respect to the σ_a using the Stickler-Berg relation the parameter is consistent with both the τ and ϕ measured [65].

Overall the dye properties are unaffected in the pH range 7–10. Starting at pH $\backsimeq$10, we observe a pronounced decrease of absorption and lifetime, and, from pH$\backsimeq$11, a similar decrease of the quantum efficiency.

5.4 Theoretical modelling of a random laser

Random lasing can be by a dispersive diffusive model, built on light diffusion coupled to the classical molecular rate equations that includes spectra mode competition [4]. This leads

to three coupled rate equations that can be solved numerically for slab geometry, expressed in equations (1.18). This model has no free parameters— it describes the realistic sample characteristics given the scattering and gain properties of the medium either measured or taken from the literature. Albeit being a simplified model of the lasing process, the coupled rate equation model compares well to the measured data, as depicted in Figure 5.7 (code courtesy of Dr. Michele Gaio).

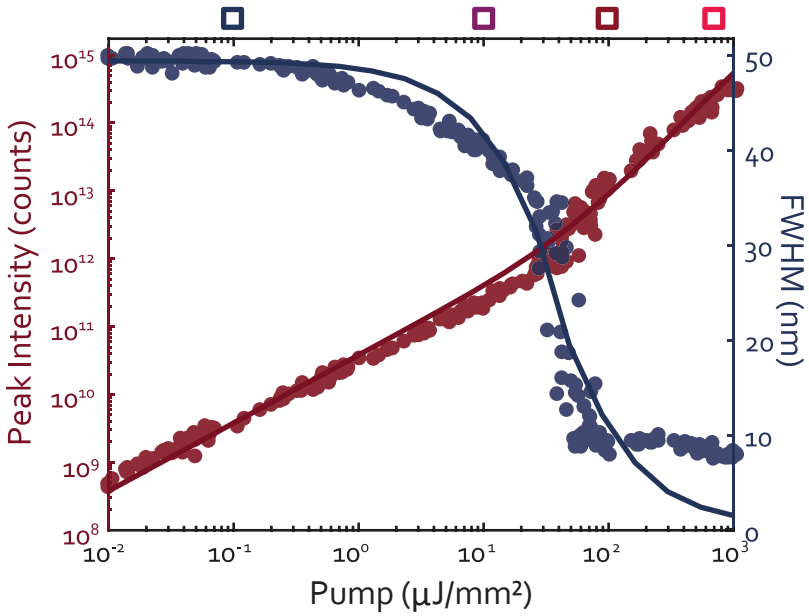

Figure 5.7: **Comparison of the experimental data with the prediction of the diffusive model.** The full circle represent the experimental data while the lines are the theoretical calculations for a slab thickness 100 μm, $\ell_t = 4\,\mu m$ and $\tau = 2.5$ ns. The experimental fluorescent spectrum of our dye was used together with typical values of rhodamine 6G absorption and stimulated emission cross-section. The model gives a theoretical threshold $P_{th} = 50\,\mu J/mm^2$ which compares well with the experimental value $P_{exp} = 70\,\mu J/mm^2$. The theoretical line-width above threshold is underestimated, as it is limited only by gain saturation.

The colour squares in Figure 5.7 correspond tot he respective colour plotted in Figure 5.8. The spectral narrowing is also consistent with the experimental result, below threshold in blue the line width is broad $\sim$ 54 nm, as the pump power increases the spectra narrows. The theoretical linewidth above threshold is underestimated as it is limited only by gain saturation, while homogeneous and inhomogeneous broadening is neglected [4].

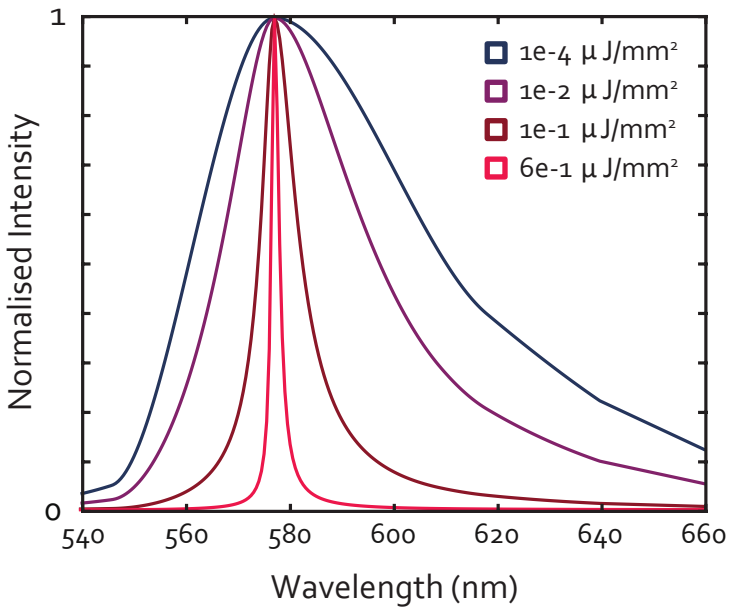

Figure 5.8: **Theoretical spectra narrowing at different pump powers.** The squares of different colours correspond to the spectra at different powers depicted in the previous figure.

5.5 Modelling random lasing sensing

The sensing dynamics can be predicted using the model used above. The parameters required to model the random laser are taken from literature or measured. A change in any of the molecular parameters would modify the lasing threshold and be detectable by the lasing sensor. More quantitatively, in the approximation of a stationary and uniform system, the lasing threshold can be expressed as:

$$T \; \alpha \; [(N\tau_c v\sigma_e - 1)\tau_r \Phi \sigma_a]^{-1} \tag{5.1}$$

where N is the molecule's density, v the speed of light in the medium, τ_c is the Thouless time (the typical time it takes for a photon to escape the disordered medium) which accounts for the losses at the surface, and the relevant properties of the molecules providing optical gain are modelled with the stimulated emission cross-section σ_e, the absorption cross section σ_a at the pump wavelength, the radiative lifetime of the excited state τ_r, and the quantum efficiency Φ. The latter two are related via the non radiative decay rate $\Gamma_{nr} = 1/\tau_{nr}$, as $\Phi = \Gamma_r/(\Gamma_r + \Gamma_{nr})$. We evaluate these parameters to investigate how a change

in the fluorescence properties translates into a change in the lasing.

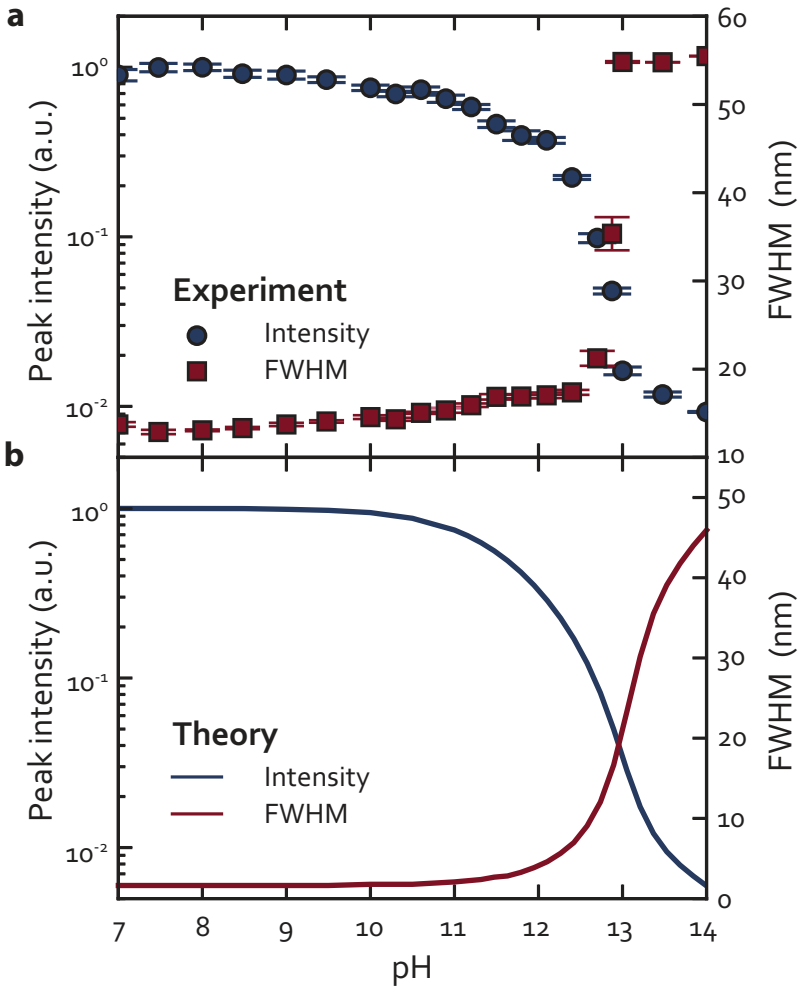

Figure 5.9: **Sensing of pH: a comparison of experiments and theory.** (a) The random-lasing system is pumped above the lasing threshold ($P = 840\ \mu J/mm^2$) and the emission characteristics as a function of the pH of the solution are recorded. The lasing is suppressed at large pH values (pH > 13), corresponding to a strong decrease of the peak intensity (the blue circles) and a sharp increase of the FWHM of the emission (the red square). (b) Theoretical prediction of the lasing response upon pH variation, which shows a similar behaviour.

Since the refractive index contrast is decreased due to the increase from air to water, an increase by a factor of 3 - 4 in the scattering strength is observed, where in air the transport is $\ell_{air} = 4\,\mu m$ and is $\ell_{water} = 14\,\mu m$. The sample ($L = 100\,\mu m$) is excited at a fixed power $P = 840\ \mu J/mm^2$ which is well above lasing threshold ($P = 80\ \mu J/mm^2$). The result is shown in Figure 5.9a , similar to the results depicted in Figure 5.2, however at larger power. A progressive decrease in peak intensity (the blue circles) is observed for an increasing pH:

beyond the value pH 13, the lasing action is switched off. The peak intensity shows an overall approximately 100-fold intensity decrease, and the FWHM (the red squares) instead increases smoothly from 14 nm at pH 7, corresponding to the above-threshold line width (shown in Figure 5.9(a), to pH 13, where it sharply reaches 54 nm, which is the FWHM of the fluorescence spectrum. This result indicates a shift of the threshold to a larger pump intensity. The error bars are calculated as the standard deviation of the average of ten repeated measurements, each by pumping with a single laser pulse. It is evident when comparing Figures 5.9 and 5.6 that the changes in the molecular properties are amplified by the lasing system, and this amplification results in a large intensity variation with a sharp transition of the lasing emission, which offers an opportunity for efficient sensing

The theoretical dependence on the sensing parameter is calculated including all measured molecular parameters, Φ, τ, $\sigma_a$while the gain cross-section (σ_e) is inferred by assuming that it scales with the absorption (σ_a) [214]. The resulting theoretical predictions are shown in Figure 5.9 b and are in very good agreement with the experimental data. As expected, the predicted lasing linewidth is underestimated, as, in the model, the narrowing is limited only by the gain saturation.

5.5.1 Limitations to experimental sensing in a biological context

Before we describe the sensing mechanism from a theoretical perspective, it is important to address the challenges and limitations of a random laser sensor, such as the one we have just described.

Biosensing relates to the detection of biologically relevant activity, this has been extensively accomplished with fluorescent probes in many configurations described in detail in the following reference [177]. However, biosensing with lasers is a field still in its infancy [56]. In the context of cavity-less lasers challenges remain in finding probes which are not only good detection targets but also have the ability to constitute a low threshold laser. In contrast, WGM laser and other cavity geometries make use of changes and deformations to the cavity or its surroundings as probes of the biological environment and therefore have more freedom when employing a dye. This added freedom also comes with a setback, for example in a cell it is becomes difficult to decouple the output from complex biological interaction that take place in the human body.

For biosensing *in-vivo* and *in-vitro* a certain level of biocompatibility is required. A mea-

sure of biocompatibility of laser sensors has yet to be extensively evaluated this is partially due to the distance from real applications. For perspective the field has gone as far as implanting lasers into cells and tissue [215, 8, 78] With biocompatibility and degradability also comes the challenge of long term stability of the lasing output. When using materials such as the ones we have explored in this thesis (polysaccharides, proteins and synthetic polymer), they tend to swell and disintegrate in biological media over time to the point where the devices stop lasing. Equally it can be problematic to decouple the change to the sensing probe from the degradation of laser. Random lasers are very robust to small changes in ℓ_t. If the device is large enough the laser can compensate by increasing the active volume as address in chapter 4.

Overall further studies on biolasers are essential to evaluate draw backs and bottleneck of the material, geometry and gain media.

5.5.2 Theoretical prediction of sensing

The sensitivity and limitation of random laser sensing can be predicted by calculating the affects of the dye parameters on the lasing threshold exploited in equation (5.1). Although these parameters are coupled in real dyes, we will consider them independently to isolate their role. We have chosen as a figure of merit the peak intensity (I) relative sensitivity, defined as:

$$S_\alpha = \left| \frac{dI/I}{d\alpha/\alpha} \right| \tag{5.2}$$

where α is the parameter examined. The linear response, $S_\alpha = 1$, is typical of the fluorescence regime. In Figure 5.6 we compute $S_\alpha$for various molecular parameters ($\alpha = \sigma_a$, τ , Φ, σ_e/σ_0) at different pump power. The colourmap highlights regions with linear response (white) for $S_\alpha = 1$ and highly nonlinear response above $S_\alpha \gg 1$ (red). The blue regions correspond to regions with negligible effect on the measured intensity. The dashed black lines are the calculated threshold, i.e.: the boundary between the fluorescence (below) and the lasing (above) regimes.

Figure 5.10 can be understood when considering the individual role of the different parameters on the lasing process. σ_a describes the absorption of the pump and therefore is directly related to the excitation probability of the dye molecules. In fluorescence sensing,

the absorption is a property typically exploited and induces a variation of the measured light intensity. Counter intuitively for lasing σ_a is a parameter of minor importance. In the regime where the size of the random laser exceeds the penetration depth of the pump, a change in the absorption can be compensated by the increase of the active area within the system. In other words, the available gain is constant, this is apparent in Figure 5.10a on the right hand side where the random laser is insensitive to changes in σ_a. For lower absorption values, left hand side of Figure 5.10a, where the absorption length is comparable to the system size, the absorbed and the emission intensity are linearly related to σ_a both for fluorescence and lasing regimes (white areas). The threshold is seen to increase slightly, Figure 5.10a dashed black line, as expected. Around the lasing threshold a twofold increase in the sensitivity is predicted where: $S_{\sigma_a} = 2.2$ (light red).

A similar behaviour is observed for parameter τ which describes the lifetime of the population in the excited states and therefore is related to the ease of inducing population inversion in the system. As depicted in Figure 5.10b the recorded intensity is largely insensitive to the change in τ, for both fluorescence and lasing regimes. Instead, a lifetime decrease induces a mild shift of the lasing threshold towards higher pump intensities resulting in a roughly linear sensitivity, with $S_\tau = 0.9$.

The quantum efficiency Φ is another quantity often exploited in fluorescence sensing techniques, as it is related directly to the emitted intensity. The wide linear region (white) below the lasing threshold, Figure 5.10c dashed line, is the linear sensitivity of the fluorescence regime. The lasing emission well above lasing threshold is marginally affected by the quantum efficiency, this is because the non-radiative decay processes are slower than the stimulated emission and therefore become irrelevant above threshold. Instead, around threshold the sensitivity peaks as shown by the red region of the plot. This can be due to the emission increasing rapidly as stimulated emission (unaffected by the parameter Φ) takes over spontaneous emission (affected by parameter Φ) The maximum sensitivity is: $S_\Phi = 201$.

The most direct way of tuning the lasing threshold is by controlling the gain value, i.e.: altering σ_e as shown in Figure 5.10d. This parameter is unique to lasing and has no effect on fluorescence. As expected, the calculated fluorescence sensitivity has no dependence on σ_e. The largest response is found around the lasing threshold. In this case a decrease of σ_e of 10% of the original value equates to a complete suppression of the lasing, independent

of the pump power. In this condition, high sensitivity $S_{\sigma_e} = 186$ is reached.

The highest sensitivities are found around the fluorescence-lasing transition, with maximum values $S_{\sigma_a} = 2.2$, $S_{\tau} = 0.9$, $S_{\Phi} = 201$ and $S_{\sigma_e} = 186$.

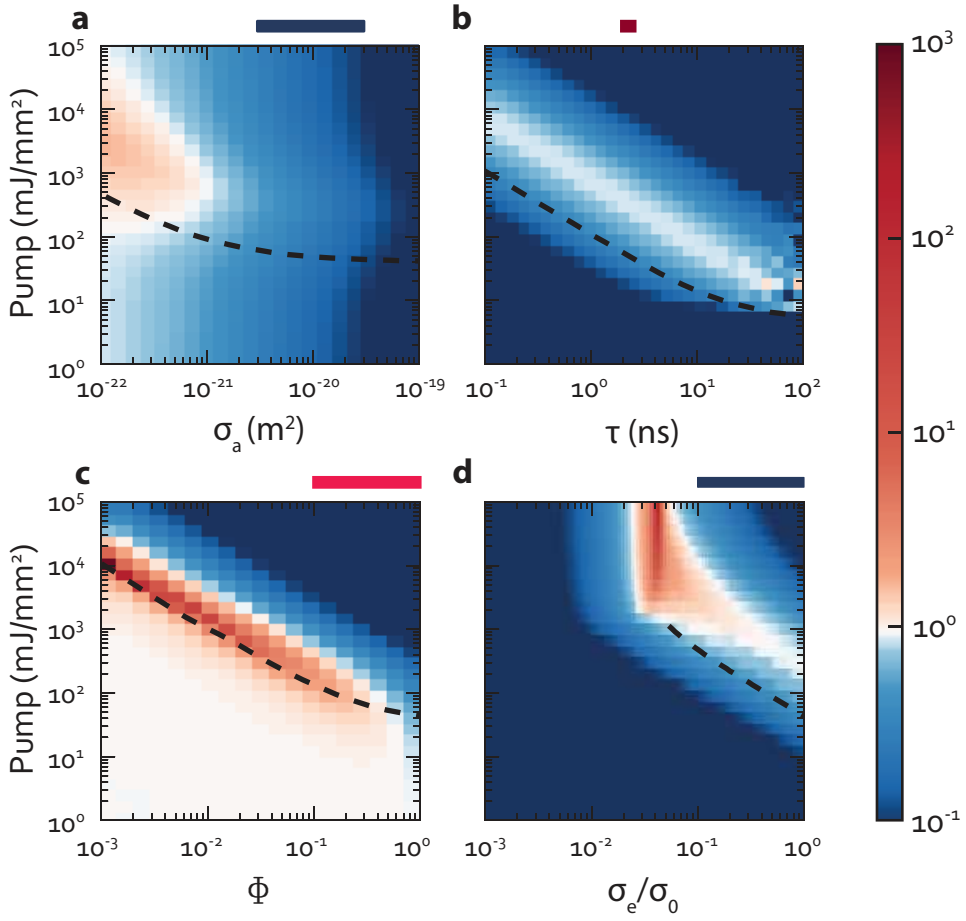

Figure 5.10: **Sensitivity analysis.** The relative sensitivity defined is calculated for the same system parameters, when varying the values of σ_a, τ , Φ and σ_e/σ_0, a, b, c, d respectively and for different pump intensities. The black dashed lines are the lasing threshold marking the boundary between the fluorescence and the lasing regime. The blue areas correspond to no sensitivity ($S_\alpha \ll 1$), the white areas correspond to linear sensitivity ($S_\alpha = 1$), and the red areas correspond to increased sensitivity ($S_\alpha \gg 1$). Each coloured bar on top of the plots indicates the measured range of variation of the corresponding parameter, as reported in Figure 5.6

We can now discuss the experimental sensing profile reported in Figure 5.9. The bars at the top of each plot in Figure 5.10 identify the measured parameter variation illustrated in Figure 5.6. Since they are coupled parameters, a response to pH variation is not surprising. Showing to be more prevalent in terms of the quantum efficiency as well as the gain. The resulting experimental sensitivity extracted from the experimental data is $S_{pH} = 200 \pm 50$

at $pH = 13$, which is larger than the theoretical prediction of $S_{pH} \backsim 60$. Finally, in the range pH = 12-13 we can estimate a limit of detection (LOD) of $\text{LOD}_{pH} \backsimeq 0.03$, defined as 3 times the signal to noise ratio.

Stimulated emission can therefore boost the sensitivity of a fluorescence sensor as well as provide an additional sensing parameter, i.e., σ_e. These advantages come at the expense of additional complexity. Lasing requires a nanophotonic architecture to promote stimulated emission, a disordered medium for random lasing, and a dye capable of providing net optical gain. The critical length limits the miniaturization of the lasing device to approximately $\sim$10 μm, which implies that the random laser sensor is not suitable for sensitivity at the single-molecule level. When compared to fluorescence schemes, random lasing requires a higher excitation intensity, in the microwatt range (> 1 μJ pulse energy) instead of the nanowatt range of conventional single-molecule spectroscopy. While this requirement could be a problem for in-vivo sensing, preliminary results in living cells [8, 78] show that these power ranges are below the damage threshold of the biological media.

5.6 Outlook/Conclusion

We introduce a random lasing sensing scheme based on the lasing intensity and FWHM modification of the gain dye parameters, which we attribute to a threshold shift. We present a detailed description of the sensing mechanism and a theoretical model which matches very well the experiments on pH sensing by silk-based random lasing. We identify the most efficient sensing scheme, with a 2-order- of-magnitude enhancement with respect to fluorescence. Given the universality of multiple scattering, its robustness against stress and deformation, and the large availability of fluorescent and lasing dyes, we foresee possible applications for biological and chemical sensing in living tissues.

6 Conclusion and future outlook

The ultimate goal of this thesis has been to fabricate and study biocompatible random lasers and evidence the enhanced sensitivity of a lasing based sensing scheme when compared to conventional techniques; we have pursued applications in biosensing, particularly in pH sensing with outlook for in body sensing.

Achieving a random lasing system which is biocompatible requires the nanostructuring of biomaterials, while interfacing the opaque material with emitting molecules. To achieve this we have separated the tasks, first focusing on the multiple scattering in biocompatible materials and subsequently studying the gain in biomaterials.

A novel fabrication technique to nanostructure and consequently enhance light interaction within biocompatible polymers is presented. Due to the flexibility of the design, the same architecture is achieved for a variety of different materials. We exploited cellulose nanocrystals to obtain highly scattering paper with potential for increasing contrast in paper based sensors while increasing porosity and allowing for a wider range functionalisation opportunities than currently explored.

Gain molecules have multiple functionalities in our sensors, not only do they provide the gain for the laser but also chemically interact and respond to changes in the chemical environment. We explored a conventional lasing structure using solid state biocompatible materials. We develop a novel and simple fabrication technique to obtain micron sized solid state lasers made with different biomaterials and studied their lasing output. BSA microlasers where found to retain their lasing action in both aqueous environment and cell culture media, and compatible with cell growth.

Stemming from the study and optimisation of light scattering and the doping of biomaterials with lasing agents, the main results of this thesis arose. We presented the first biocompatible silk random laser with the ability to sense pH with a 2-order- of-magnitude enhancement with respect to fluorescence. Furthermore, we miniaturise the random lasers

and studied the output in terms of their size. While at large sizes the threshold is constant, at smaller sizes the threshold increases rapidly and the appearance of pronounced spikes is observed. Due to our controlled geometry, the modal output of the random lasers can be in future studied in more detail and may answer help understand how the modal output depends on size. The smallest size random laser operational in water achieved is a few 10s of microns in diameter, just above the size limit which can be implemented into the cell. Further miniaturisation could be possibly achieved by optimising the gain and void diameter or more simply by using materials of larger refractive index. Although this may be a simple solution, high refractive index materials such as semiconductors, can prove toxic and unlike the materials we used throughout this thesis are in large part not biodegradable. Nevertheless, other applications are still in reach dependent upon the tailoring the sensing band to relevant pHs. Currently pH sensing is used in a variety of industries such as pharmaceutical, agriculture water, water waste treatment, environmental control and in food and beverage industries which hold the majority of the market. Although there are many pH sensors available there are still gaps in the market such as for the detection of waterborne diseases and contamination of water. Unlike most high sensitivity pH meters our device has the potential of conducting continuous monitoring of pH without the need of calibration and buffers, which can be particularly useful for fast out of the box usage for disposable devises. Perhaps the best potential application lies in localised probing on tissues. Averaging effect of measurements can cover critical differences between cells and sections of the tissue, mapping different micro regions can reveal additional information with important biological implication [216, 217, 218]. This can be accomplished either directly on the skin or in laparoscopic cavities using keyhole or minimally invasive surgery. Initial studies on a skin phantom has already indicated the possibility for integration and operation of the miniature lasers in the fibrous collagen network similar to human skin.

Bibliography

[1] Gustav Mie. Beitrzur Optik trMedien, speziell kolloidaler Metall\"osungen. *Annalen der Physik*, 330(3):377–445, 1908.

[2] C F Bohren and D R Huffman. Absorption and scattering of light by small particles, 1983.

[3] Hendrik Christoffel Hulst. *Light scattering by small particles*. 1981.

[4] Michele Gaio, Matilda Peruzzo, and Riccardo Sapienza. Tuning random lasing in photonic glasses. *Optics Letters*, 40(7):1611–1614, 2015.

[5] Frank Vollmer, Stephen Arnold, L. Rayleigh, SL. McCall, AFJ. Levi, RE. Slusher, SJ. Pearton, RA. Logan, F. Vollmer, S. Arnold, VS. Ilchenko, AA. Savchenkov, AB. Matsko, L. Maleki, P. McIver, CM. Linton, M. McIver, D. Evans, R. Porter, SJ. Chapman, DP. Hewett, LN. Trefethen, PA. Martin, T. Antonakakis, RV. Craster, S. Guenneau, EA. Skelton, DV. Evans, CM. Linton, R. Porter, DV. Evans, R. Porter, DV. Evans, CM. Linton, M. McIver, AS. Bonnet-Bendhia, F. Starling, CM. Linton, V. Zalipaev, I. Thompson, JB. Pendry, L. Martin-Moreno, FJ. Garcia-Vidal, PA. Huidubro, S. Xiaopeng, J. Cuerda, E. Moreno, L. Martin-Moreno, FJ. Garcia-Vidal, TJ. Cui, JB. Pendry, RA. Hurd, D. Sengupta, M. Makwana, A. Antonakakis, B. Maling, S. Guenneau, RV. Craster, RV. Craster, J. Kaplunov, AV. Pichugin, FWJ. Olver, W. Wijngaard, DJ. Colquitt, RV. Craster, T. Antonakakis, S. Guenneau, and COMSOL Ltd. Whispering-gallery-mode biosensing: label-free detection down to single molecules. *Nature methods*, 5(7):591–6, 2008.

[6] Martin D. Baaske, Matthew R. Foreman, and Frank Vollmer. Single-molecule nucleic acid interactions monitored on a label-free microcavity biosensor platform. *Nature Nanotechnology*, 9(11):933–939, 2014.

[7] M. Humar and I. Muševič. Surfactant sensing based on whispering-gallery-mode lasing in liquid-crystal microdroplets. *Optics Express*, 19(21):19836, 2011.

[8] Matjaž Humar and Seok Hyun Yun. Intracellular microlasers. *Nature Photonics*, (July):3–8, 2015.

[9] Diederik S Wiersma. The physics and applications of random lasers. *Nat Phys*, 4(5):359–367, 2008.

[10] N. Garcia, A. Z. Genack, and A. A. Lisyansky. Measurement of the transport mean free path of diffusing photons. *Physical Review B*, 46(22):14475–14479, 1992.

[11] R. Sapienza, P. García, J. Bertolotti, M. Martín, Á. Blanco, L. Viña, C. López, and D. Wiersma. Observation of Resonant Behavior in the Energy Velocity of Diffused Light. *Physical Review Letters*, 99(23):233902, dec 2007.

[12] Matteo Burresi, Lorenzo Cortese, Lorenzo Pattelli, Mathias Kolle, Peter Vukusic, Diederik S Wiersma, Ullrich Steiner, and Silvia Vignolini. Bright-White Beetle Scales Optimise Multiple Scattering of Light. *Scientific Reports*, 4:1–7, 2014.

[13] Pete Vukusic, Benny Hallam, and Joe Noyes. Brilliant whiteness in ultrathin beetle scales, 2007.

[14] A. E Seago, P. Brady, J.-P. Vigneron, and T. D Schultz. Gold bugs and beyond: a review of iridescence and structural colour mechanisms in beetles (Coleoptera). *Journal of The Royal Society Interface*, 6(Suppl_2):S165–S184, 2009.

[15] Ad Lagendijk and Bart A. van Tiggelen. Resonant multiple scattering of light. *Physics Reports*, 270(3):143–215, 1996.

[16] P. García, R. Sapienza, J. Bertolotti, M. Martín, Á Blanco, a. Altube, L. Viña, D. Wiersma, and C. López. Resonant light transport through Mie modes in photonic glasses. *Physical Review A*, 78(2):023823, aug 2008.

[17] Bart Van Tiggelen. Introduction to Wave Scattering, Localization and Mesoscopic Phenomena. Second edition. *Waves in Random and Complex Media*, 17(2):235–237, 2007.

[18] Brian D. Lawrence, Mark Cronin-Golomb, Irene Georgakoudi, David L. Kaplan, and Fiorenzo G. Omenetto. Bioactive silk protein biomaterial systems for optical devices. *Biomacromolecules*, 9(4):1214–1220, 2008.

[19] J. X. Zhu, D. J. Pine, and D. a. Weitz. Internal-Reflection of Diffusive Light in Random-Media. *Physical Review A*, 44(6):3948–3959, 1991.

[20] D. J. Durian. Influence of boundary reflection and refraction on diffusive photon transport. *Physical Review E*, 50(2):857–866, 1994.

[21] Subrahmanyan Chandrasekhar. Radiative Transfer. *New York Dover*, page 393, 1960.

[22] William Guerin, Y. D. Chong, Quentin Baudouin, Matthias Liertzer, Stefan Rotter, and Robin Kaiser. Diffusive to quasi-ballistic random laser: incoherent and coherent models. *Journal of the Optical Society of America B*, 33(9):1888, 2016.

[23] Rachid Elaloufi, Rémi Carminati, and Jean-Jacques Greffet. Diffusive-to-ballistic transition in dynamic light transmission through thin scattering slabs: a radiative transfer approach. *Journal of the Optical Society of America. A, Optics, image science, and vision*, 21(8):1430–1437, 2004.

[24] Annamaneni Peraiah. *An introduction to radiative transfer: methods and applications in astrophysics*. 2002.

[25] George B. Rybicki and Alan P. Lightman. *Radiative Processes in Astrophysics*, volume 25. 1981.

[26] Lihong V. Wang and Hsin-I Wu. *Biomedical Optics: Principles and Imaging*. 2012.

[27] E. Akkermans and G. Montambaux. Mesoscopic physics of photons. *Journal of the Optical Society of America B*, 21(1):101–112, 2004.

[28] Pierre Etienne Wolf and Georg Maret. Weak localization and coherent backscattering of photons in disordered media. *Physical Review Letters*, 55(24):2696–2699, 1985.

[29] Yasuo Kuga and Akira Ishimaru. Retroreflectance from a dense distribution of spherical particles. *J. Opt. Soc. Am. A*, 1(8):831–835, 1984.

[30] D G Goebel. Generalized integrating-sphere theory. *Applied optics*, 6(1):125–8, 1967.

[31] Max Krook. Physical Review. 38(May):991–993, 1977.

[32] Eli Yablonovitch. Inhibited spontaneous emission in solid-state physics and electronics. *Physical Review Letters*, 58(20):2059–2062, 1987.

[33] Sajeev John. Strong localization of photons in certain disordered dielectric superlattices. *Physical Review Letters*, 58(23):2486–2489, 1987.

[34] Stuart Krauss, Thomas F., De La Rue, Richard M., Brand. Two-dimensional photonic-bandgap structures operating at near-infrared wavelengths. *Nature*, 383:699, 1996.

[35] Chaoming Song, Ping Wang, and Hernán a. Makse. A phase diagram for jammed matter. *Nature*, 453(7195):629–632, 2008.

[36] Juan F Galisteo-López, Marta Ibisate, Riccardo Sapienza, Luis S Froufe-Pérez, Alvaro Blanco, and Cefe López. Self-assembled photonic structures. *Advanced materials (Deerfield Beach, Fla.)*, 23(1):30–69, jan 2011.

[37] Van Albada and Ad Lagendijk. Observation of weak localization of light in a random medium, 1985.

[38] P. W. Anderson. Absence of diffusion in certain random lattices. *Physical Review*, 109(5):1492–1505, 1958.

[39] A. Z. Genack, N. Garcia, and W. Polkosnik. Long-range intensity correlation in random media. *Physical Review Letters*, 65(17):2129–2132, 1990.

[40] David A Weitz. PHYSICS. Packing in the spheres. *Science (New York, N.Y.)*, 303(5660):968–9, 2004.

[41] James G. Berryman. Random close packing of hard spheres and disks. *Physical Review A*, 27(2):1053–1061, 1983.

[42] Pedro David García, Riccardo Sapienza, and Cefe López. Photonic glasses: A step beyond white paint. *Advanced Materials*, 22(1):12–19, 2010.

[43] Pedro David García, Riccardo Sapienza, Álvaro Blanco, and Cefe López. Photonic glass: A novel random material for light. *Advanced Materials*, 19(18):2597–2602, 2007.

[44] J. W. Goodwin, J. Hearn, C. C. Ho, and R. H. Ottewill. Studies on the preparation and characterisation of monodisperse polystyrene laticee. *Colloid and Polymer Science*, 252(6):464–471, 1974.

[45] P. Jiang, J. F. Bertone, K. S. Hwang, and V. L. Colvin. Single-Crystal Colloidal Multilayers of Controlled Thickness. *Chemistry of Materials*, 11(8):2132–2140, 1999.

[46] David J. Norris, Erin G. Arlinghaus, Linli Meng, Ruth Heiny, and L. E. Scriven. Opaline photonic crystals: How does self-assembly work? *Advanced Materials*, 16(16):1393–1399, 2004.

[47] Geoffrey I.N. Waterhouse and Mark R. Waterland. Opal and inverse opal photonic crystals: Fabrication and characterization. *Polyhedron*, 26(2):356–368, 2007.

[48] Sunghwan Kim, Alexander N Mitropoulos, Joshua D Spitzberg, Hu Tao, David L Kaplan, and Fiorenzo G Omenetto. Silk inverse opals. *Nature Photonics*, 6(12):818–823, 2012.

[49] Anthony E. Siegman. *Lasers*. 1986.

[50] Dhruv Saxena, Sudha Mokkapati, Patrick Parkinson, Nian Jiang, Qiang Gao, Hark Hoe Tan, and Chennupati Jagadish. Optically pumped room-temperature GaAs nanowire lasers. *Nature Photonics*, 7(12):963–968, 2013.

[51] P. Eaton, S. W. ; Fu, A.; Ning, C. Z. and Yang. Semiconductor Nanowire Lasers. *Nature Materials*, 1:1 – 11, 2016.

[52] Benjamin S. Williams. Terahertz quantum-cascade lasers, 2007.

[53] David J. Bergman and Mark I. Stockman. Surface Plasmon Amplification by Stimulated Emission of Radiation: Quantum Generation of Coherent Surface Plasmons in Nanosystems. *Physical Review Letters*, 90(2):027402, 2003.

[54] M. A. Noginov, G. Zhu, A. M. Belgrave, R. Bakker, V. M. Shalaev, E. E. Narimanov, S. Stout, E. Herz, T. Suteewong, and U. Wiesner. Demonstration of a spaser-based nanolaser. *Nature*, 460(7259):1110–1112, 2009.

[55] Y.-J. Lu, J. Kim, H.-Y. Chen, C. Wu, N. Dabidian, C. E. Sanders, C.-Y. Wang, M.-Y. Lu, B.-H. Li, X. Qiu, W.-H. Chang, L.-J. Chen, G. Shvets, C.-K. Shih, and S. Gwo.

Plasmonic Nanolaser Using Epitaxially Grown Silver Film. *Science*, 337(6093):450–453, 2012.

[56] Xudong Fan and Seok-Hyun Yun. The potential of optofluidic biolasers. *Nature methods*, 11(2):141–7, feb 2014.

[57] A. Javan, W. R. Bennett, and D. R. Herriott. Population inversion and continuous optical maser oscillation in a gas discharge containing a He-Ne mixture. *Physical Review Letters*, 6(3):106–110, 1961.

[58] C. K N Patel. Continuous-Wave Laser Action on Vibrational-Rotational Transitions of CO2. *Physical Review*, 136(5A), 1964.

[59] J. E. Geusic, H. M. Marcos, and L. G. Van Uitert. Laser oscillations in nd-doped yttrium aluminum, yttrium gallium and gadolinium garnets. *Applied Physics Letters*, 4(10):182–184, 1964.

[60] Haiming Zhu, Yongping Fu, Fei Meng, Xiaoxi Wu, Zizhou Gong, Qi Ding, Martin V. Gustafsson, M. Tuan Trinh, Song Jin, and X-Y. Zhu. Lead halide perovskite nanowire lasers with low lasing thresholds and high quality factors. *Nature Materials*, 14(6):636–642, 2015.

[61] Fritz P. Schäfer, Werner Schmidt, and Jürgen Volze. Organic dye solution laser. *Applied Physics Letters*, 9(8):306–309, 1966.

[62] Fritz P. Schäfer. Principles of Dye Laser Operation. *Dye Lasers*, (1966):1–2, 1990.

[63] Jonathan Shankle. Ophthalmic photography: retinal photography, angiography, and electronic imaging. *Survey of Ophthalmology*, 49(2):264, 2004.

[64] Thomas Mathew, Simran Kundan, Mohammed Idhrees Abdulsamad, Sabarinath Menon, Baiju S. Dharan, and K. Jayakumar. Multiple muscular ventricular septal defects: Use of fluorescein dye to identify residual defects. *Annals of Thoracic Surgery*, 97(1), 2014.

[65] S. J. Strickler and R. A. Berg. Relationship between Absorption Intensity and Fluorescence Lifetime of Molecules. *The Journal of Chemical Physics*, 37(4):814, 1962.

[66] M. Y. Berezin and S. Achilefu. Fluorescence lifetime measurements and biological imaging. *Chemical Reviews*, 110(5):2641–2684, 2010.

[67] M Karl, C P Dietrich, M Schubert, I D W Samuel, G A Turnbull, and M C Gather. Single cell induced optical confinement in biological lasers. *Journal of Physics D: Applied Physics*, 50(8):084005, 2017.

[68] Matjaž Humar, Malte C. Gather, and Seok-Hyun Yun. Cellular dye lasers: lasing thresholds and sensing in a planar resonator. *Optics Express*, 23(21):27865, 2015.

[69] Malte C. Gather and Seok Hyun Yun. Single-cell biological lasers. *Nature Photonics*, 5(7):406–410, 2011.

[70] Lina He, Kaya Ozdemir, and Lan Yang. Whispering gallery microcavity lasers. *Laser and Photonics Reviews*, 7(1):60–82, 2013.

[71] Andrea M Armani, Rajan P Kulkarni, Scott E Fraser, Richard C Flagan, and Kerry J Vahala. Detection with Optical Microcavities. *Science*, 317(August):783–787, 2007.

[72] Jonathan Ward and Oliver Benson. WGM microresonators: Sensing, lasing and fundamental optics with microspheres, 2011.

[73] Matthew R. Foreman, Jon D. Swaim, and Frank Vollmer. Whispering gallery mode sensors. *Adv. Opt Photonics*, 30(7):168–240, 2015.

[74] Yan Wang, Hanyang Li, Liyuan Zhao, Bing Wu, Shuangqiang Liu, Yongjun Liu, and Jun Yang. A review of droplet resonators: Operation method and application. *Optics and Laser Technology*, 86:61–68, 2016.

[75] Sedat Nizamoglu, Malte C Gather, and Seok Hyun Yun. All-biomaterial laser using vitamin and biopolymers. *Advanced materials (Deerfield Beach, Fla.)*, 25(41):5943–7, nov 2013.

[76] Preston T. Snee, Yinthai Chan, Daniel G. Nocera, and Moungi G. Bawendi. Whispering-gallery-mode lasing from a semiconductor nanocrystal/ microsphere resonator composite. *Advanced Materials*, 17(9):1131–1136, 2005.

[77] Van Duong Ta, Rui Chen, and Han Dong Sun. Tuning whispering gallery mode lasing from self-assembled polymer droplets. *Scientific reports*, 3:1362, 2013.

[78] Marcel Schubert, Anja Steude, Philipp Liehm, Nils M Kronenberg, Markus Karl, Elaine C. Campbell, Simon J. Powis, and Malte Gather. Lasing within live cells containing intracellular optical micro-resonators for barcode-type cell tagging and tracking. *Nano Letters*, page 150717175233008, 2015.

[79] C. C. Lam, P. T. Leung, and K. Young. Explicit asymptotic formulas for the positions, widths, and strengths of resonances in Mie scattering. *Journal of the Optical Society of America B*, 9(9):1585, 1992.

[80] Sindy K. Y. Tang, Ratmir Derda, Qimin Quan, Marko Lončar, and George M. Whitesides. Continuously tunable microdroplet-laser in a microfluidic channel. *Optics Express*, 19(3):2204, 2011.

[81] S Letokhov. GENERATION OF LIGHT BY A SCATTERING MEDIUM WITH NEGATIVE RESONANCE. 26(4), 1968.

[82] R. M. Balachandran N. M. Lawandy. Laser action in strongly scattering media. *Nature*, 368:436–438, 1994.

[83] Lech Sznitko, Jaroslaw Mysliwiec, and Andrzej Miniewicz. The role of polymers in random lasing. *Journal of Polymer Science Part B: Polymer Physics*, 53(14):951–974, 2015.

[84] Ilenia Viola, Neda Ghofraniha, Antonella Zacheo, Valentina Arima, Claudio Conti, and Giuseppe Gigli. Random laser emission from a paper-based device. *Journal of Materials Chemistry C*, 1(48):8128–8133, 2013.

[85] Molíria V. Dos Santos, Christian T. Dominguez, João V. Schiavon, Hernane S. Barud, Luciana S A De Melo, Sidney J L Ribeiro, Anderson S L Gomes, and Cid B. De Araújo. Random laser action from flexible biocellulose-based device. *Journal of Applied Physics*, 115(8):1–5, 2014.

[86] Qinghai Song, Shumin Xiao, Zhengbin Xu, Jingjing Liu, Xuanhao Sun, Vladimir Drachev, Vladimir M Shalaev, Ozan Akkus, and Young L Kim. Random lasing in bone tissue. *Optics letters*, 35(9):1425–1427, 2010.

[87] Randal C. Polson and Z. Valy Vardeny. Random lasing in human tissues. *Applied Physics Letters*, 85(7):1289–1291, 2004.

[88] Michele Gaio, Dhruv Saxena, Jacopo Bertolotti, Dario Pisignano, Andrea Camposeo, and Riccardo Sapienza. Photonic network random lasing in the Anderson localized regime. pages 1–8, 2017.

[89] Dengfeng Huang, Tingshuai Li, Shenye Liu, Tao Yi, Chuanke Wang, Jin Li, Xiyun Liu, and Min Xu. Random lasing action from electrospun nanofibers doped with laser dyes. *Laser Physics*, 27(3), 2017.

[90] Sarah Krämmer, Christoph Vannahme, Cameron L C Smith, Tobias Grossmann, Michael Jenne, Stefan Schierle, Lars Jørgensen, Ioannis S. Chronakis, Anders Kristensen, and Heinz Kalt. Random-cavity lasing from electrospun polymer fiber networks. *Advanced Materials*, 26(48):8096–8100, 2014.

[91] Stefano Gottardo, Riccardo Sapienza, Pedro D. García, Alvaro Blanco, Diederik S. Wiersma, and Cefe López. Resonance-driven random lasing. *Nature Photonics*, 2(7):429–432, jun 2008.

[92] P. D. García, M. Ibisate, R. Sapienza, D. S. Wiersma, and C. López. Mie resonances to tailor random lasers. *Physical Review A - Atomic, Molecular, and Optical Physics*, 80(1):1–6, 2009.

[93] a. Tulek, R. C. Polson, and Z. V. Vardeny. Naturally occurring resonators in random lasing of π-conjugated polymer films. *Nature Physics*, 6(4):303–310, 2010.

[94] R. C. Polson, A. Chipouline, and Z. Valy Vardeny. Random Lasing in p-Conjugated Films and Infiltrated Opals. *Advanced Materials*, 13:760–764, 2001.

[95] Q. Baudouin, N. Mercadier, V. Guarrera, W. Guerin, and R. Kaiser. A cold-atom random laser. *Nature Physics*, 9(6):357–360, 2013.

[96] Sajeev John and Gendi Pang. Theory of lasing in a multiple-scattering medium. *Physical Review A*, 54(4):3642–3652, 1996.

[97] Diederik S Wiersma, Meint P. van Albada, and Ad Lagendijk. Random laser?, 1995.

[98] R. Pierrat and R. Carminati. Threshold of random lasers in the incoherent transport regime. *Physical Review A - Atomic, Molecular, and Optical Physics*, 76(2):1–6, 2007.

[99] Robert J. Rutten. Radiative Transfer in Stellar Atmospheres. *Radiative Transfer in Stellar Atmospheres*, page 255, 2003.

[100] S Johansson and V Letokhov. Astrophysical lasers and nonlinear optical effects in space. *New Astronomy Reviews*, 51(5-6):443–523, 2007.

[101] G. E. Schröder-Turk, S. Wickham, H. Averdunk, F. Brink, J. D. Fitz Gerald, L. Poladian, M. C.J. Large, and S. T. Hyde. The chiral structure of porous chitin within the wing-scales of Callophrys rubi. *Journal of Structural Biology*, 174(2):290–295, 2011.

[102] H Fabritius, C Sachs, D Raabe, S Nikolov, M Friak, and J Neugebauer. Chitin in the Exoskeletons of Arthropoda: From Ancient Design to Novel Materials Science. In *Chitin: Formation amd Diagenesis*, volume 34, pages 35–60. 2011.

[103] M. J. Frenkel and J. M. Gillespie. The proteins of the keratin component of bird?S beaks. *Australian Journal of Biological Sciences*, 29(6):467–480, 1976.

[104] C. Legnani, C. Vilani, V. L. Calil, H. S. Barud, W. G. Quirino, C. A. Achete, S. J L Ribeiro, and M. Cremona. Bacterial cellulose membrane as flexible substrate for organic light emitting devices. *Thin Solid Films*, 517(3):1016–1020, 2008.

[105] Mihai Irimia-Vladu, Niyazi Serdar Sariciftci, and Siegfried Bauer. Exotic materials for bio-organic electronics. *J. Mater. Chem.*, 21(5):1350–1361, 2011.

[106] Sarah Christoph, Julien Kwiatoszynski, Thibaud Coradin, and Francisco M. Fernandes. Cellularized Cellular Solids via Freeze-Casting. *Macromolecular Bioscience*, 16(2):182–187, 2016.

[107] Felix Kratz. Albumin as a drug carrier: Design of prodrugs, drug conjugates and nanoparticles. *Journal of Controlled Release*, 132(3):171–183, 2008.

[108] R. L. Moy, A. Lee, and A. Zalka. Commonly used suture materials in skin surgery, 1991.

[109] Gabriel S. Perrone, Gary G. Leisk, Tim J. Lo, Jodie E. Moreau, Dylan S. Haas, Bernke J. Papenburg, Ethan B. Golden, Benjamin P. Partlow, Sharon E. Fox, Ahmed M. S. Ibrahim, Samuel J. Lin, and David L. Kaplan. The use of silk-based devices for fracture fixation. *Nature Communications*, 5, 2014.

[110] Fiorenzo G. Omenetto and David L. Kaplan. A new route for silk. *Nature Photonics*, 2(11):641–643, 2008.

[111] Lorenz Meinel, Robert Fajardo, Sandra Hofmann, Robert Langer, Jake Chen, Brian Snyder, Gordana Vunjak-Novakovic, and David Kaplan. Silk implants for the healing of critical size bone defects. *Bone*, 37(5):688–698, 2005.

[112] Sara T. Parker, Peter Domachuk, Jason Amsden, Jason Bressner, Jennifer A. Lewis, David L. Kaplan, and Fiorenzo C. Omenetto. Biocompatible silk printed optical waveguides. *Advanced Materials*, 21(23):2411–2415, 2009.

[113] Yunkyoung Choi, Heonsu Jeon, and Sunghwan Kim. A fully biocompatible single-mode distributed feedback laser. *Lab Chip*, 15(3):642–645, 2015.

[114] Hu Tao, David L Kaplan, and Fiorenzo G Omenetto. Silk materials–a road to sustainable high technology. *Advanced materials (Deerfield Beach, Fla.)*, 24(21):2824–37, jun 2012.

[115] Sarute Ummartyotin and Hathaikarn Manuspiya. A critical review on cellulose: From fundamental to an approach on sensor technology, 2015.

[116] V. Favier, H. Chanzy, and J. Y. Cavaillé. Polymer Nanocomposites Reinforced by Cellulose Whiskers. *Macromolecules*, 28(18):6365–6367, 1995.

[117] Satoshi Masaoka, Tatsuhiko Ohe, and Naokazu Sakota. Production of cellulose from glucose by Acetobacter xylinum. *Journal of Fermentation and Bioengineering*, 75(1):18–22, 1993.

[118] Albert Mihranyan. Cellulose from cladophorales green algae: From environmental problem to high-tech composite materials. *Journal of Applied Polymer Science*, 119(4):2449–2460, 2011.

[119] Youssef Habibi, Lucian A. Lucia, and Orlando J. Rojas. Cellulose nanocrystals: Chemistry, self-assembly, and applications. *Chemical Reviews*, 110(6):3479–3500, 2010.

[120] Majeti N.V Ravi Kumar. A review of chitin and chitosan applications. *Reactive and Functional Polymers*, 46(1):1–27, 2000.

[121] Julian F. V. Vincent. *Structural biomaterials*. 2012.

[122] X F Liu, Y L Guan, D Z Yang, Z Li, and K D Yao. Antibacterial Action of Chitosan and Carboxymethlyated Chitosan. *Journal of Applied Polymer Science*, 79(March):1324, 2000.

[123] R. Jayakumar, M. Prabaharan, P. T. Sudheesh Kumar, S. V. Nair, and H. Tamura. Biomaterials based on chitin and chitosan in wound dressing applications, 2011.

[124] Fwu Long Mi, Shin Shing Shyu, Yu Bey Wu, Sung Tao Lee, Jen Yeu Shyong, and Rong Nan Huang. Fabrication and characterization of a sponge-like asymmetric chitosan membrane as a wound dressing. *Biomaterials*, 22(2):165–173, 2001.

[125] Abul Kalam Azad, Niwet Sermsintham, Suwalee Chandrkrachang, and Willem Frans Stevens. Chitosan membrane as a wound-healing dressing: Characterization and clinical application. *Journal of Biomedical Materials Research*, 69B(2):216–222, 2004.

[126] Zhihong Nie, Christian A Nijhuis, Jinlong Gong, Xin Chen, Alexander Kumachev, Andres W Martinez, Max Narovlyansky, and George M Whitesides. Electrochemical sensing in paper-based microfluidic devices. *Lab on a Chip*, 10(4):477–83, 2010.

[127] Chaoyi Yan, Jiangxin Wang, Wenbin Kang, Mengqi Cui, Xu Wang, Ce Yao Foo, Kenji Jianzhi Chee, and Pooi See Lee. Highly stretchable piezoresistive graphene-nanocellulose nanopaper for strain sensors. *Advanced Materials*, 26(13):2022–2027, 2014.

[128] Jacqui L. Delaney, Conor F. Hogan, Junfei Tian, and Wei Shen. Electrogenerated chemiluminescence detection in paper-based microfluidic sensors. *Analytical Chemistry*, 83(4):1300–1306, 2011.

[129] Ratmir Derda, Anna Laromaine, A. Mammoto, Sindy K Y Tang, Tadanori Mammoto, Donald E Ingber, and George M Whitesides. Paper-supported 3D cell culture for tissue-based bioassays. *Proceedings of the National Academy of Sciences*, 106(44):18457–18462, 2009.

[130] Robert J. Moon, Ashlie Martini, John Nairn, John Simonsen, and Jeff Youngblood. Cellulose nanomaterials review: structure, properties and nanocomposites. *Chemical Society Reviews*, 40(7):3941, 2011.

[131] Martin A. Hubbe, Joel J. Pawlak, and Alexander A. Koukoulas. Paper's appearance: A review, 2008.

[132] S. J. Eichhorn, A. Dufresne, M. Aranguren, N. E. Marcovich, J. R. Capadona, S. J. Rowan, C. Weder, W. Thielemans, M. Roman, S. Renneckar, W. Gindl, S. Veigel, J. Keckes, H. Yano, K. Abe, M. Nogi, A. N. Nakagaito, A. Mangalam, J. Simonsen, A. S. Benight, A. Bismarck, L. A. Berglund, and T. Peijs. Review: Current international research into cellulose nanofibres and nanocomposites, 2010.

[133] Lindy Heath and Wim Thielemans. Cellulose nanowhisker aerogels. *Green Chemistry*, 12(8):1448, 2010.

[134] James D. Beard and J. Eichorn Stephen. Highly Porous Thermoplastic Composite and Carbon Aerogel from Cellulose Nanocrystals. *Materials Letters*, 221(March):248–251, 2018.

[135] Rajalaxmi Dash, Yang Li, and Arthur J. Ragauskas. Cellulose nanowhisker foams by freeze casting. *Carbohydrate Polymers*, 88(2):789–792, 2012.

[136] Dieter Klemm, Friederike Kramer, Sebastian Moritz, Tom Lindstrom, Mikael Ankerfors, Derek Gray, and Annie Dorris. Nanocelluloses: A new family of nature-based materials. *Angewandte Chemie - International Edition*, 50(24):5438–5466, 2011.

[137] Ning Lin, Jin Huang, and Alain Dufresne. Polysaccharide Nanocrystals-Based Materials for Advanced Applications. In *Polysaccharide-Based Nanocrystals: Chemistry and Applications*, pages 219–254. 2015.

[138] Masaya Nogi, Shinichiro Iwamoto, Antonio Norio Nakagaito, and Hiroyuki Yano. Optically Transparent Nanofiber Paper. *Advanced Materials*, 21(16):1595–1598, 2009.

[139] My Ahmed Saïd Azizi Samir, Fannie Alloin, Jean Yves Sanchez, Nadia El Kissi, and Alain Dufresne. Preparation of Cellulose Whiskers Reinforced Nanocomposites from an Organic Medium Suspension. *Macromolecules*, 37(4):1386–1393, 2004.

[140] Stephanie Beck, Myriam Méthot, and Jean Bouchard. General procedure for determining cellulose nanocrystal sulfate half-ester content by conductometric titration. *Cellulose*, 22(1):101–116, 2015.

[141] Bruno Frka-Petesic, Bruno Jean, and Laurent Heux. First experimental evidence of a giant permanent electric-dipole moment in cellulose nanocrystals. *EPL (Europhysics Letters)*, 107(2):28006, 2014.

[142] L. Heux, G. Chauve, and C. Bonini. Nonflocculating and chiral-nematic self-ordering of cellulose microcrystals suspensions in nonpolar solvents. *Langmuir*, 16(21):8210–8212, 2000.

[143] J. F. Revol, H. Bradford, J. Giasson, R. H. Marchessault, and D. G. Gray. Helicoidal self-ordering of cellulose microfibrils in aqueous suspension. *International Journal of Biological Macromolecules*, 14(3):170–172, 1992.

[144] Ahu G. Dumanli, Hanne M. Van Der Kooij, Gen Kamita, Erwin Reisner, Jeremy J. Baumberg, Ullrich Steiner, and Silvia Vignolini. Digital color in cellulose nanocrystal films. *ACS Applied Materials and Interfaces*, 6(15):12302–12306, 2014.

[145] Ahu Gumrah Dumanli, Gen Kamita, Jasper Landman, Hanne van der Kooij, Beverley J. Glover, Jeremy J. Baumberg, Ullrich Steiner, and Silvia Vignolini. Controlled, bio-inspired self-assembly of cellulose-based chiral reflectors. *Advanced Optical Materials*, 2(7):646–650, 2014.

[146] Michael Giese, Lina K. Blusch, Mostofa K. Khan, Wadood Y. Hamad, and Mark J. Maclachlan. Responsive mesoporous photonic cellulose films by supramolecular cotemplating. *Angewandte Chemie - International Edition*, 53(34):8880–8884, 2014.

[147] Giulia Guidetti, Siham Atifi, Silvia Vignolini, and Wadood Y. Hamad. Flexible Photonic Cellulose Nanocrystal Films. *Advanced Materials*, 28(45):10042–10047, 2016.

[148] Galina Rodionova, Marianne Lenes, Øyvind Eriksen, and Øyvind Gregersen. Surface chemical modification of microfibrillated cellulose: improvement of barrier properties for packaging applications. *Cellulose*, 18(1):127–134, 2010.

[149] Erwan Gicquel, C??line Martin, Jos?? Garrido Yanez, and Julien Bras. Cellulose nanocrystals as new bio-based coating layer for improving fiber-based mechanical and barrier properties. *Journal of Materials Science*, pages 1–14, 2016.

[150] Stefano Toffanin, Sunghwan Kim, Susanna Cavallini, Marco Natali, Valentina Benfenati, Jason J. Amsden, David L. Kaplan, Roberto Zamboni, Michele Muccini, and

Fiorenzo G. Omenetto. Low-threshold blue lasing from silk fibroin thin films. *Applied Physics Letters*, 101(9):091110, 2012.

[151] Christoph Vannahme, Florian Maier-Flaig, Uli Lemmer, and Anders Kristensen. Single-mode biological distributed feedback laser. *Lab on a Chip*, 13(14):2675, 2013.

[152] Xiang Wu, Maung Kyaw Khaing Oo, Karthik Reddy, Qiushu Chen, Yuze Sun, and Xudong Fan. Optofluidic laser for dual-mode sensitive biomolecular detection with a large dynamic range. *Nature communications*, 5:3779, 2014.

[153] Xiang Wu, Qiushu Chen, Yuze Sun, and Xudong Fan. Bio-inspired optofluidic lasers with luciferin. *Applied Physics Letters*, 102(20):2014–2017, 2013.

[154] Yun-Lu Sun, Zhi-Shan Hou, Si-Ming Sun, Bo-Yuan Zheng, Jin-Feng Ku, Wen-Fei Dong, Qi-Dai Chen, and Hong-Bo Sun. Protein-Based Three-Dimensional Whispering-Gallery-Mode Micro-Lasers with Stimulus-Responsiveness. *Scientific Reports*, 5(August):12852, 2015.

[155] F Lahoz, I R Martín, M Urgellés, J Marrero-Alonso, R Marín, C J Saavedra, A Boto, and M Díaz. Random laser in biological tissues impregnated with a fluorescent anticancer drug. *Laser Physics Letters*, 12(4):45805, 2015.

[156] S M Spillane, T J Kippenberg, and K J Vahala. Ultralow-threshold Raman laser using a spherical dielectric microcavity. *Nature*, 415:621–623, 2002.

[157] Xue Feng Jiang, Chang Ling Zou, Li Wang, Qihuang Gong, and Yun Feng Xiao. Whispering-gallery microcavities with unidirectional laser emission, 2016.

[158] Junjie Li, Hong Sun, Da Sun, Yuli Yao, Fanglian Yao, and Kangde Yao. Biomimetic multicomponent polysaccharide/nano-hydroxyapatite composites for bone tissue engineering. *Carbohydrate Polymers*, 85(4):885–894, 2011.

[159] W J Chung, J W Oh, K Kwak, B Y Lee, and J Meyer. Biomimetic self-templating supramolecular structures. *Nature*, 478(7369):364–368, 2011.

[160] Gladstone Christopher Jayakumar, Nagarajan Usharani, Kohsaku Kawakami, Jonnalagadda Raghava Rao, and Balachandran Unni Nair. Preparation of antibacterial

collagen-pectin particles for biotherapeutics. *RSC Advances*, 4(81):42846–42854, 2014.

[161] A. Ashkin and J. M. Dziedzic. Observation of resonances in the radiation pressure on dielectric spheres. *Physical Review Letters*, 38(23):1351–1354, 1977.

[162] H.-M. Tzeng, K. F. Wall, M. B. Long, and R. K. Chang. Laser emission from individual droplets at wavelengths corresponding to morphology-dependent resonances. *Optics Letters*, 9(11):499, 1984.

[163] H-B. Lin, J. D. Eversole, and a. J. Campillo. Spectral properties of lasing microdroplets. *Journal of the Optical Society of America B*, 9(1):43, 1992.

[164] S.-X. QIAN, J. B. SNOW, H.-M. TZENG, and R. K. CHANG. Lasing Droplets: Highlighting the Liquid-Air Interface by Laser Emission. *Science*, 231(4737):486–488, 1986.

[165] Melikhan Tanyeri, Richard Perron, and Ian M. Kennedy. Lasing droplets in a microfabricated channel. *Optics Letters*, 32(17):2529, 2007.

[166] J. Schäfer, J. P. Mondia, R. Sharma, Z. H. Lu, A. S. Susha, A. L. Rogach, and L. J. Wang. Quantum dot microdrop laser. *Nano Letters*, 8(6):1709–1712, 2008.

[167] M Humar, M Ravnik, S Pajk, and I Musevic. Electrically tunable liquid crystal optical microresonators. *Nature Photonics*, 3(10):595–600, 2009.

[168] Younan Xia and George M. Whitesides. Soft Lithography. *Angewandte Chemie International Edition*, 37(5):550–575, 1998.

[169] Lee, Park, and Whitesides. Solvent compatibility of poly (dimethylsiloxane)-based microfluidic devices. *Analytical Chemistry-Washington Dc-*, 75(23):6544–6554, 2003.

[170] Ralph H. Petrucci, F. Geoffrey Herring, Jeffri D. Madura, and Carey Bissonnette. *General Chemistry: Principles and Modern Applications*. 2016.

[171] Van Duong Ta, Shancheng Yang, Yue Wang, Yuan Gao, Tingchao He, Rui Chen, Hilmi Volkan Demir, and Handong Sun. Multicolor lasing prints. *Applied Physics Letters*, 107(22), 2015.

[172] D. J. Gardiner, W.-K. Hsiao, S. M. Morris, P. J. W. Hands, T. D. Wilkinson, I. M. Hutchings, and H. J. Coles. Printed photonic arrays from self-organized chiral nematic liquid crystals. *Soft Matter*, 8(39):9977, 2012.

[173] Mitsunori Saito and Kentaro Koyama. Deformable microdroplet cavity fabricated by an inkjet method. *Japanese Journal of Applied Physics*, 49(9 PART 1), 2010.

[174] John Edgar French. Toxicology and Carcinogenesis Studies of Rhodamine 6G. *National toxicology program Technical Report Series*, (364):1–192, 1989.

[175] Robert Sjöback, Jan Nygren, Mikael Kubista, Robert Sjback, Jan Nygren, and Mikael Kubista. Absorption and fluorescence properties of fluorescein. *Spectrochimica Acta Part A*, 51:L7–L21, 1995.

[176] Judith E. Selwyn and Jeffrey I. Steinfeld. Aggregation Equilibria of Xanthene Dyes. *The Journal of Physical Chemistry*, 76(5):762–774, 1972.

[177] Alexander P. Demchenko. *Introduction to fluorescence sensing*. 2009.

[178] D. C. Valdes-Aguiler, O., & Neckers. Aggregation Phenomena in Xanthene Dyes. *Accounts Of Chemical Research.*, 22(23):171–177, 1989.

[179] Hengky Chandrahalim and Xudong Fan. Reconfigurable Solid-state Dye-doped Polymer Ring Resonator Lasers. *Scientific Reports*, 5, 2015.

[180] Yanhui Wei, Xianqing Lin, Cong Wei, Wei Zhang, Yongli Yan, and Yong Sheng Zhao. Starch-Based Biological Microlasers. 2016.

[181] H B Lin, a L Huston, B L Justus, and a J Campillo. Some characteristics of a droplet whispering-gallery-mode laser. *Optics letters*, 11(10):614–616, 1986.

[182] Malte C. Gather and Seok Hyun Yun. Bio-optimized energy transfer in densely packed fluorescent protein enables near-maximal luminescence and solid-state lasers. *Nature Communications*, 5:1–8, 2014.

[183] Malte C. Gather and Seok Hyun Yun. Lasing from Escherichia coli bacteria genetically programmed to express green fluorescent protein. *Optics Letters*, 36(16):3299, 2011.

[184] Hui Cao. Review on latest developments in random lasers with coherent feedback. *Journal of Physics A: Mathematical and General*, 38(49):10497–10535, 2005.

[185] Marco Leonetti, Riccardo Sapienza, Marta Ibisate, Claudio Conti, and Cefe López. Optical gain in DNA-DCM for lasing in photonic materials. *Optics letters*, 34(24):3764–3766, 2009.

[186] Konrad Cyprych, Lech Sznitko, and Jaroslaw Mysliwiec. Starch: Application of biopolymer in random lasing. *Organic Electronics: physics, materials, applications*, 15(10):2218–2222, 2014.

[187] R. Zhang, S. Knitter, S. F. Liew, F. G. Omenetto, B. M. Reinhard, H. Cao, and L. Dal Negro. Plasmon-enhanced random lasing in bio-compatible networks of cellulose nanofibers. *Applied Physics Letters*, 108(1), 2016.

[188] F. G. Omenetto and D. L. Kaplan. New Opportunities for an Ancient Material. *Science*, 329(5991):528–531, 2010.

[189] Robson R. da Silva, Christian T. Dominguez, Molíria V. dos Santos, Renato Barbosa-Silva, Maurício Cavicchioli, Lívia M. Christovan, Luciana S. a. de Melo, Anderson S. L. Gomes, Cid B. de Araújo, and Sidney J. L. Ribeiro. Silk fibroin biopolymer films as efficient hosts for DFB laser operation. *Journal of Materials Chemistry C*, 1(43):7181, 2013.

[190] Brian D. Lawrence, Mark Cronin-Golomb, Irene Georgakoudi, David L. Kaplan, and Fiorenzo G. Omenetto. Bioactive silk protein biomaterial systems for optical devices. *Biomacromolecules*, 9(4):1214–1220, 2008.

[191] Xiao Hu, Karen Shmelev, Lin Sun, Eun Seok Gil, Sang Hyug Park, Peggy Cebe, and David L. Kaplan. Regulation of silk material structure by temperature-controlled water vapor annealing. *Biomacromolecules*, 12(5):1686–1696, 2011.

[192] Ramy G.S. El-Dardiry and Ad Lagendijk. Tuning random lasers by engineered absorption. *Applied Physics Letters*, 98(16):1–4, 2011.

[193] Daniël Vanmaekelbergh and Lambert K. van Vugt. ZnO nanowire lasers. *Nanoscale*, 3(7):2783, 2011.

[194] Bernhard Wunderlich, David M Bodily, and Mark H Kaplan. Theory and Measurements of the Glass-Transformation Interval of Polystyrene. 95(1), 1964.

[195] Attila Imre and W. Alexander Van Hook. Liquid Liquid Demixing from Solutions of Polystyrene. *Journal of Physical and Chemical Reference Data*, 25:637, 1996.

[196] Kiyoshi Kawai, Toru Suzuki, and Masaharu Oguni. Low-temperature glass transitions of quenched and annealed bovine serum albumin aqueous solutions. *Biophysical journal*, 90(10):3732–8, 2006.

[197] N. Irving Sax and Richard J. Lewis. *Hawley's Condensed Chemical Dictionary. 11th ed.* 1987.

[198] Fangqiong Tang, Linlin Li, and Dong Chen. Mesoporous silica nanoparticles: Synthesis, biocompatibility and drug delivery. *Advanced Materials*, 24(12):1504–1534, 2012.

[199] U. G. K. Wegst, M. Schecter, A. E. Donius, and P. M. Hunger. Biomaterials by freeze casting. *Philosophical Transactions of the Royal Society A: Mathematical, Physical and Engineering Sciences*, 368(1917):2099–2121, 2010.

[200] Sylvain Deville, Eduardo Saiz, and Antoni P. Tomsia. Freeze casting of hydroxyapatite scaffolds for bone tissue engineering. *Biomaterials*, 27(32):5480–5489, 2006.

[201] Paul F. McDonagh and Stuart K. Williams. The preparation and use of fluorescent-protein conjugates for microvascular research. *Microvascular Research*, 27(1):14–27, 1984.

[202] Stephan Schreml, Robert J Meier, Otto S Wolfbeis, Michael Landthaler, Rolf-Markus Szeimies, and Philipp Babilas. 2D luminescence imaging of pH in vivo. *Proceedings of the National Academy of Sciences of the United States of America*, 108:2432–2437, 2011.

[203] Yan Geng, Mohammad A Ali, Andrew J Clulow, Shengqiang Fan, Paul L Burn, Ian R Gentle, Paul Meredith, and Paul E Shaw. Unambiguous detection of nitrated explosive vapours by fluorescence quenching of dendrimer films. *Nature communications*, 6:8240, 2015.

[204] Aimée Rose, Zhengguo Zhu, Conor F Madigan, Timothy M Swager, and Vladimir Bulović. Sensitivity gains in chemosensing by lasing action in organic polymers. *Nature*, 434(7035):876–879, 2005.

[205] Brett H Hokr, Joel N Bixler, Gary D Noojin, Robert J Thomas, Benjamin a Rockwell, Vladislav V Yakovlev, and Marlan O Scully. Single-shot stand-off chemical identification of powders using random Raman lasing. *Proceedings of the National Academy of Sciences of the United States of America*, 111(34):12320–4, 2014.

[206] Seung Ho Choi and Young L. Kim. The potential of naturally occurring lasing for biological and chemical sensors. *Biomedical Engineering Letters*, 4(3):201–212, 2014.

[207] D S Wiersma and S Cavalieri. Light emission: A temperature-tunable random laser. *Nature*, 414(December):708–709, 2001.

[208] Fernando Lopez Arbeloa, Inaki Llona Gonzalez, Pilar Ruiz Ojeda, and Inigo Lopez Arbeloa. Aggregate formation of rhodamine 6G in aqueous solution. *Journal of the Chemical Society, Faraday Transactions 2*, 78(7):989, 1982.

[209] Arig Ibrahim Hashim, Xiaomeng Zhang, Jonathan W. Wojtkowiak, Gary V. Martinez, and Robert J. Gillies. Imaging pH and metastasis. *NMR in Biomedicine*, 24(6):582–591, 2011.

[210] Georgina Gethin. The significance of surface pH in chronic wounds. *Wounds UK*, 3(3):52–56, 2007.

[211] B. Marelli, M. A. Brenckle, D. L. Kaplan, and F. G. Omenetto. Silk Fibroin as Edible Coating for Perishable Food Preservation. *Scientific Reports*, 6(1):25263, 2016.

[212] Joseph a. Curcio and Charles C. Petty. The Near Infrared Absorption Spectrum of Liquid Water. *Journal of the Optical Society of America*, 41(5):302, 1951.

[213] Dani Setiawan, Andranik Kazaryan, Muhamad Abdulkadir Martoprawiro, and Michael Filatov. A first principles study of fluorescence quenching in rhodamine B dimers: how can quenching occur in dimeric species? *Physical Chemistry Chemical Physics*, 12(37):11238, 2010.

[214] W Holzer, H Gratz, T Schmitt, A Penzkofer, A Costela, R Sastre, and F J Duarte. Photo-physical characterization of rhodamine 6G in a. *Science*, 256, 2000.

[215] Matjaž Humar, Sheldon J. J. Kwok, Myunghwan Choi, Sangyeon Cho, Ali K. Yetisen,

and Seok-Hyun Yun. Towards biomaterial-based implantable photonic devices. *Nanophotonics*, Accepted:60–80, 2016.

[216] James R Heath, Antoni Ribas, and Paul S Mischel. Single cell analytic tools for drug discovery and development. *Nature Reviews Drug Discovery*, 15:204–216, 2016.

[217] Michael Boutros, Florian Heigwer, and Christina Laufer. Microscopy-Based High-Content Screening. *Cell*, 163(6):1314–1325, 2015.

[218] William P. Janzen. Screening technologies for small molecule discovery: The state of the art, 2014.